

WIND FARM MODELING: FROM THE MESO-SCALE TO THE MICRO-SCALE

by

Christian Santoni-Ortiz



APPROVED BY SUPERVISORY COMMITTEE:

Stefano Leonardi, Chair

Giacomo Valerio Iungo

William Anderson

Yaoyu Li

Copyright © 2018
Christian Santoni-Ortiz
All rights reserved

*To my lovely wife,
it is my joy to spend
this space and this time
with you.*

WIND FARM MODELING: FROM THE MESO-SCALE TO THE MICRO-SCALE

by

CHRISTIAN SANTONI-ORTIZ, BSc, MSc

DISSERTATION

Presented to the Faculty of
The University of Texas at Dallas
in Partial Fulfillment
of the Requirements
for the Degree of

DOCTOR OF PHILOSOPHY IN
MECHANICAL ENGINEERING

THE UNIVERSITY OF TEXAS AT DALLAS

August 2018

ACKNOWLEDGMENTS

I would like to express deep appreciation to my committee chair and supervisor, Professor Leonardi, who has taught me how an excellent scientist should be. His highly energetic guidance was always a motivation to keep working and studying hard. Without his help and encouragement none of this research would have been possible. Thank you for this opportunity.

I would like to thank each committee member for their insightful comments, suggestions and for sharing their knowledge, which has been essential for this and future works.

Thanks to my friends and colleagues, Edgardo Garcia, Isnardo Arenas, Kenneth Carrasquillo and Umberto Ciri, for all the stimulating discussions, sleepless nights working together and all the fun we had. Fridays at Fillmore's would not have been fun without you guys. Our energetic discussions about science, politics and philosophy could not have been better.

Last but not least, I would like to thank my wife. This journey would have been unbearable without you. Thank you for your support and encouragement. Thank you for believing in me.

This work would not have been possible without the financial support of the Wind Integration Simulations PIRE (WINDINSPIRE) and the WindStar Industry/University Cooperative Research Center.

July 2018

WIND FARM MODELING: FROM THE MESO-SCALE TO THE MICRO-SCALE

Christian Santoni-Ortiz, PhD
The University of Texas at Dallas, 2018

Supervising Professor: Stefano Leonardi, Chair

This dissertation is focused on numerical modeling of wind turbines. An initial set of simulations is performed to assess the effect of the tower and nacelle on the wake of a wind turbine. The wind turbine is modeled using the Actuator Line Model for the rotor and the Immersed Boundary Method for the tower and nacelle. Results are compared with the experimental measurements made at NTNU (Norwegian University of Science and Technology), and numerical simulations available in the literature. For the first time, we show that the tower and nacelle not only produce a velocity deficit in the wake but also affect the entrainment of mean kinetic energy. The wake of the tower interacts with that generated by the turbine blades, promoting the breakdown of the tip vortex and increasing the mean kinetic energy flux into the wake.

Additionally, we studied the effect of topography on the performance and wake of a wind turbine. The topography consists of wavy ridges that are perpendicular to the flow direction. The effect of the relative position of the rotor and terrain geometry is assessed by placing the turbine either at the crest or trough of the undulating wall.

To study wind turbines under realistic conditions, one-way nested mesoscale to microscale simulations of an on-shore wind farm have been performed using the Weather Research and Forecasting (WRF) model. Each simulation contains five nested domains modeling the mesoscale wind field using the planetary boundary layer scheme on the entire north Texas

Panhandle region to microscale wind fluctuations and turbine wakes of a wind farm with Large-Eddy simulation (LES). Moreover, an additional nesting with our in-house LES code is performed. Numerical results agree well with meteorological, LiDAR and SCADA data. Power production and momentum deficit obtained with our in-house LES code and actuator disk model presented a better agreement than WRF because the simulation captures the wind shear on the rotor.

TABLE OF CONTENTS

ACKNOWLEDGMENTS	v
ABSTRACT	vi
LIST OF FIGURES	x
LIST OF TABLES	xiv
CHAPTER 1 INTRODUCTION	1
1.1 Intellectual Merit	5
1.2 Broader Impact	5
CHAPTER 2 METHODOLOGY AND MODELING	6
2.1 Governing Equations	6
2.2 Discretization of the Navier-Stokes Equations	6
2.2.1 Time Discretization	7
2.2.2 Stability of the Numerical Scheme	12
2.3 Sub-grid Stress Modeling	12
2.4 Immersed Boundary Method	14
2.5 Turbine Modeling	16
CHAPTER 3 THE WAKE OF THE TOWER AND NACELLE	19
3.1 Introduction	19
3.1.1 Literature Review	19
3.2 Geometrical Configuration	21
3.3 Result and Analysis	23
3.3.1 Mean Flow	23
3.3.2 Mean Kinetic Energy Entrainment	28
3.3.3 Coherent Structures	30
3.3.4 Turbulent Kinetic Energy	33
3.4 Conclusion	37
CHAPTER 4 PERFORMANCE OF A WIND TURBINE ON A RIDGED TERRAIN	39
4.1 Introduction	39
4.1.1 Literature Review	39

4.2	Numerical Setup	41
4.3	Results and Discussion	42
4.3.1	Wind Turbine Wake and Recovery	42
4.3.2	Power Fluctuations	47
4.4	Conclusion	48
CHAPTER 5 NUMERICAL SIMULATION OF AN ONSHORE WIND FARM . .		50
5.1	Introduction	50
5.1.1	Literature Review	50
5.2	Methodology	52
5.2.1	Wind Farm layout	52
5.2.2	Numerical Scheme and Flow Configuration	53
5.3	Validation against Met-Tower data	57
5.3.1	Velocity Spectra	60
5.4	Validation Against LiDAR	62
5.5	Power Production	67
5.6	Conclusion	74
CHAPTER 6 FINAL REMARKS		75
REFERENCES		77
BIOGRAPHICAL SKETCH		84
CURRICULUM VITAE		

LIST OF FIGURES

1.1	Cumulative wind power production. Department of Energy Wind Vision study scenario [1].	2
1.2	Average turbine rotor diameter and hub height installed during period. 2015 Wind technologies market report [2].	3
2.1	Computational cell with pressure pressure computed in the cell center and staggered velocity in the cell faces	7
2.2	Geometrical sketch of the grid around a section of the tower. The arrows indicate the position in the grid where the velocities are defined (staggered). The velocities inside the body (x in red) are set to zero. The derivatives of the velocities at the closest points around the boundary are computed using the real distance to the body (Δx and Δy) and not the grid spacing. The latter would result in a stepwise body.	15
2.3	Blade cross-section in the plane $T - \theta$, where T is the direct ion of the thrust force and θ is the azimuthal direction.	16
2.4	Sketch of the distribution of the aerodynamic load among the plane of the blade section.	17
3.1	Computational box.	22
3.2	Contours of \bar{U}_1 in a vertical section; (a, b) $\lambda = 3$, (c,d) $\lambda = 6$, with (b,d), and without tower and nacelle (a,c); (e,f,g,h) vertical profiles of the mean streamwise velocity 1D (----) and 3D (----) downwind the rotor disk: LES results (—) and experiments (\circ).	24
3.3	Time averaged streamwise velocity profiles: (a) $\lambda = 3$, 1D downwind, (b) $\lambda = 3$, 3D downwind, (c) $\lambda = 6$, 1D downwind, (d) $\lambda = 6$, 3D downwind: present simulations with (—) and without (----) the tower and nacelle, (—) numerical results from [3], and (\bullet) experimental measurements [4].	25
3.4	Streamwise velocity averaged in time and over the rotor disk, $\langle U_{\text{rot}} \rangle$: $\lambda = 3$ with (—) and without tower and nacelle (----); $\lambda = 6$ with (—) and without (----) tower and nacelle. The vertical dashed lines denote the position of the rotor.	27
3.5	Iso-surface of λ_2 super-imposed to color contours of $-\bar{U}\overline{uw}$ on a horizontal plane at hub height: $\lambda = 3$ (a,b), $\lambda = 6$ (c,d), with (b,d) and without (a,c) tower and nacelle (note that color ranges vary with tip speed ratio).	29
3.6	Iso-contours of $\lambda_2 = -3$ for a turbine with tower and nacelle (not shown in the figure for clarity) and tip speed ratio $\lambda = 6$; front (a), side (b) and back (c) views. The region closer to the turbine axis is colored darker.	30

3.7	Color contours of instantaneous streamwise velocity in horizontal planes at $0.75D$ (a,d), $0.4D$ (b,e) and $0.01D$ (c,f) from the bottom wall. Top $\lambda = 3$, bottom $\lambda = 6$.	31
3.8	Color contours of the time averaged wall-normal vorticity, $\bar{\omega}_y$, in a horizontal plane located at $0.75D$ from the bottom wall: (a) $\lambda = 3$ and (b) $\lambda = 6$.	32
3.9	Profiles of turbulent kinetic energy production at $3D$ (left) and $6D$ (right) for $\lambda = 6$: with (—) and without (---) tower and nacelle. Horizontal dashed lines denote the highest and lowest points reached by the blade tip during its revolution.	33
3.10	Color contours of Turbulent kinetic energy (TKE) in a x-y plane (left column) and x-z plane (right column): (a-b, e-f) $\lambda = 3$, (c-d, g-h) $\lambda = 6$ with (b,d,f,h) and without (a,c,e,g) tower and nacelle.	34
3.11	Turbulent kinetic energy profiles: present results with (—) and without (---) tower and nacelle compared to experimental measurements (\bullet). Top $\lambda = 3$, bottom $\lambda = 6$; (a,c) $1D$, (b,d) $3D$ downwind the rotor disk.	36
4.1	Computational box geometrical configuration.	41
4.2	Vertical profiles of the time averaged streamwise velocity (top) and turbulent intensity (bottom) at: a) $x/D = -1.5$, b) $x/D = 1.5$, c) $x/D = 3.0$ d) $x/D = 4.5$ and e) $x/D = 6.0$ from the turbine rotor located in the flat terrain (.....), flat with wavy inlet (—), cavity (----) and crest (—) of the wavy wall.	43
4.3	Streamwise profile of the rotor area averaged velocity U_{Rot} non-dimensionalized with the rotor averaged velocity at the entrance of the computational box for a turbine placed in a flat terrain (.....), flat with wavy inlet (—), cavity (----) and crest (—) of the wavy wall.	44
4.4	Color contours of time averaged streamwise velocity with superimposed mean kinetic energy tubes for a turbine placed in: a) a flat terrain, b) flat terrain with wavy inlet and in the c) crest and d) cavity of the wavy terrain. The black (\blacksquare) and gray (\square) delimits the energy tube due to mean kinetic energy convection only and the superposition of convection and flux due to turbulence, respectively.	45
4.5	Tangential aerodynamic load at 75% of the blade span (left) and power spectra of the fluctuations of the load (right) for the turbine located flat terrain (—), flat terrain with wavy inlet (—), cavity (—) and crest (—) of the wavy wall	47
4.6	Time series of the normalized power for the turbine located flat terrain (—), flat terrain with wavy inlet (—), cavity (—) and crest (—) of the wavy wall with slope $a/\lambda_W = 0.0167$ (left) and $a/\lambda_W = 0.0333$ (right).	48
5.1	Wind farm layout superimposed over the color contours of the topographic elevation. The location of the met-tower is marked by the red circle (\bullet) and the LiDAR by the red square (\blacksquare). The position of each turbine is marked by a solid circle (\bullet).	52

5.2	Color contours of the topographic elevation of the Texas Panhandle region. The state boundaries are delimited by the dotted lines (.....) and the domains by the solid lines (——). The position of each turbine is marked by a solid circle (●).	53
5.3	High fidelity Large Eddy simulation domain, delimited by the solid lines (——). The turbines location are indicated by the black circles (●). The location of the meteorological tower is denoted by the red circle (●) and the LiDAR by the red square (■).	55
5.4	Time variation of the wind speed (a), wind direction (b) and turbulence intensity (c) at 80 m height for 2015/09/05 through 2015/09/10; (— —) WRF simulation <i>D2</i> , (----) WRF simulation <i>D5</i> and (——) met tower measurements. Shaded gray region delimits the nigh-time period.	58
5.5	Time variation of the bulk Richardson number (a) and shear exponent (b) at 80 m height for 2015/09/05 through 2015/09/10; (— —) WRF simulation <i>D2</i> , (----) WRF simulation <i>D5</i> and (——) met tower measurements. Shaded gray region delimits the nigh-time period.	59
5.6	Spectra of the wind speed at 80 <i>m</i> high of domain; (----) <i>D1</i> , (— —) <i>D2</i> , (.....) <i>D3</i> , (— —) <i>D4</i> , (----) <i>D5</i> , (——) met-tower measurements and (——) SCADA from a turbine located in the southernmost row. The solid lines represent an energy decay with slope -1 and $-5/3$	61
5.7	Numerical simulation velocity profile comparison against (——) LiDAR wind speed measurements; (a) mean wind speed profile, (b) mean absolute gross error, (c) root mean square error and (d) index of agreement of the (——) numerical results at <i>D2</i> , (——) numerical results at <i>D5</i> and (----) numerical VAD at <i>D5</i> . Horizontal dashed lines (----) delimits the turbines rotor area.	62
5.8	Color contours of the absolute value of the radial velocity field obtain from the LiDAR measurements (a, c) and virtual LiDAR from the MDTKE numerical simulations (b, d) during stable (a, b) and unstable (c, d) atmospheric boundary conditions at an elevation angle of 3° , synchronized in time. The turbine position are denoted by a solid circle (●).	65
5.9	Color contours of the absolute value of the radial velocity field obtained from the LiDAR measurements (a,f), WRF (b,g) and UTD-WF LES (c,h) during stable (a-e) and unstable (f-j) atmospheric conditions at an elevation angle of 3° . The velocity magnitude obtained from WRF MDTKE (d,i) and UTD-WF (e,j) on a plane at hub-height is alsow shown as reference. The turbine positions are denoted by a black circle (●).	66
5.10	Polar and color histogram of the wind direction and power (P/P_T), respectively, during (a) stable and (b)unstable conditions. The colorbar correspond to the histogram bins with increments of 5% of the nominal power production.	68

5.11	Mean absolute gross error (a) and index of agreement (b) of each turbine within the wind farm; (\circ) MDTKE turbines and (\circ) MO turbines. Size of each circle is relative to the value shown for each turbine.	69
5.12	Wind farm normalized net power production for the 2015/09/05 through 2015/09/10; (—) SCADA data, (----) MDTKE turbines and (----) MO turbines. Shaded gray region delimits the night-time period.	70
5.13	Power production of the northern-most row (a,b), middle row (c,d) and southern-most row (e,f); (—) SCADA measurements, (—) WRF simulation and (—) high-fidelity LES. The night-time is delimited by the shaded region.	71
5.14	Velocity profile at 10:30 UTC averaged along $1D$ in the spanwise direction; a) $2D$ upwind, b) at the rotor and c) $0.5D$ downwind of turbine $T1$ of the WRF simulation (—) and high-fidelity LES (—) The rotor region is delimited by (.....) and the hub-height is indicated with (—).	73

LIST OF TABLES

2.1	Low-Storage Runge-Kutta scheme	8
4.1	Power coefficient and rms for each case.	48
5.1	WRF domains size and resolution	54
5.2	Turbine power production mean absolute gross error and index of agreement . .	73

CHAPTER 1

INTRODUCTION

Since the onset of the industrial revolution, human activities have reached scales that are potentially changing the global environment [5]. One of the many human-driven processes that had captured the global attention is the increase in the average global temperature due to the increase in the concentration of greenhouse gases in the atmosphere, especially CO₂. The increment in the levels of carbon dioxide, reaching over 400 parts per million, have been linked to the massive expansion in the use of fossil fuels. As a consequence and due to the increasing environmental consciousness, a great interest on renewable energy sources has been raised. One of the most promising resources of renewable energy is wind.

The energy of the wind has been harnessed since ancient times for propelling sailing ships and boats. Although, nowadays sailing boats are mainly used for recreational purpose, once it was one of the most important means of transportation vital for the market across seas. Another wind-powered tool with a similar importance for the development of the agriculture is the windmill. This machine, of Persian origin, was used for the processing of grains and pumping water for crops. Originally, the machines consisted of a vertical shaft with a light wooden sails attached by horizontal struts. After it reached Europe, with the help of gears, the rotor was turned horizontally having a larger efficiency than its counterpart with vertical axis rotor.

Eolic electric power generation began with the first modern wind turbine constructed in 1890 in Denmark [6]. During the 1970's the wind power gained visibility as a commercial power generation in the United States due to the 1973 oil crisis. To date, wind energy is the fastest growing source of electricity in the U.S. with an increase rate of 30% per year. Due to the competitive, long-term stable pricing, economic development potential and its environmental attributes, the Department of Energy of the United States has decided to increase the wind

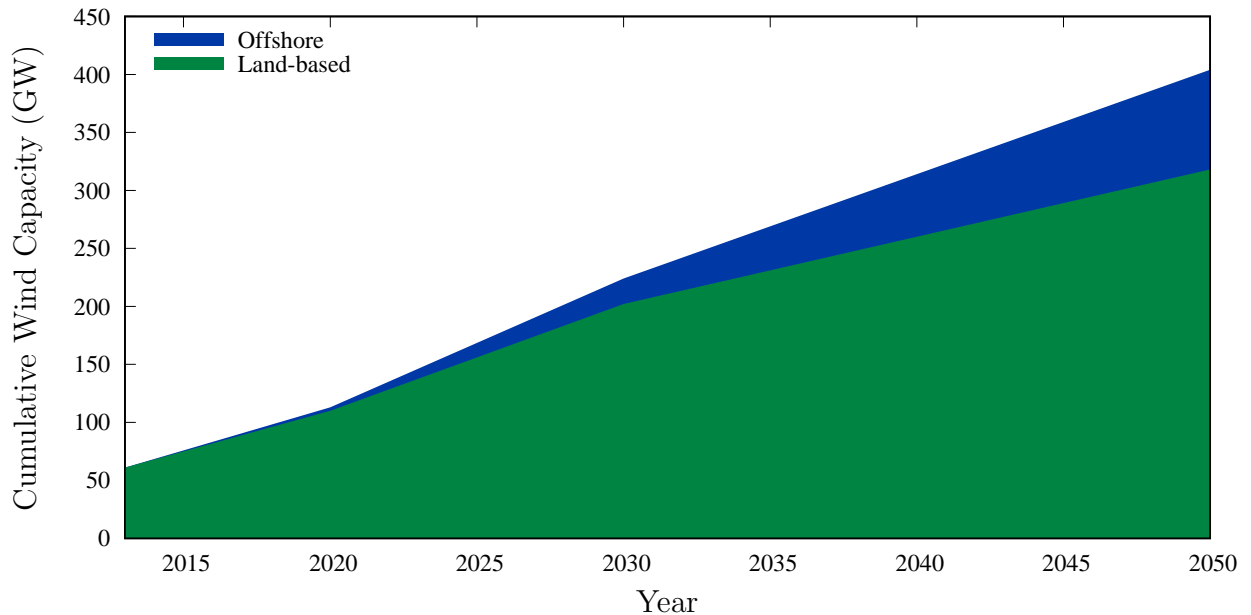


Figure 1.1. Cumulative wind power production. Department of Energy Wind Vision study scenario [1].

energy penetration [1]. The proposed target of wind penetration is of 20% for the year 2030, which corresponds to around 113 GW, with a long-term goal of 35% by 2050.

To meet up with the demand and reach the targeted goals, wind turbines are clustered in larger arrays known as wind farms. From an economical standpoint, ideally, the distance between the turbines should be as close as possible to reduce the required land area. Due to the wake interaction, the turbines operating in the lee side of another turbine produce 40% to 60% less power than in isolated conditions, therefore reducing the overall efficiency of the power plant [7]. This is a major concern as the hub height and the rotor diameter are increasing significantly (see Figure 1.2 [2]) and mitigating the wake interaction requires vast amount of land.

Due to the size of the rotor, the turbines cannot be studied as isolated. The landscape may induce velocity fluctuations that can be detrimental for the power production and increase fatigue loads thus reducing the operational life of the blades. At the same time, the

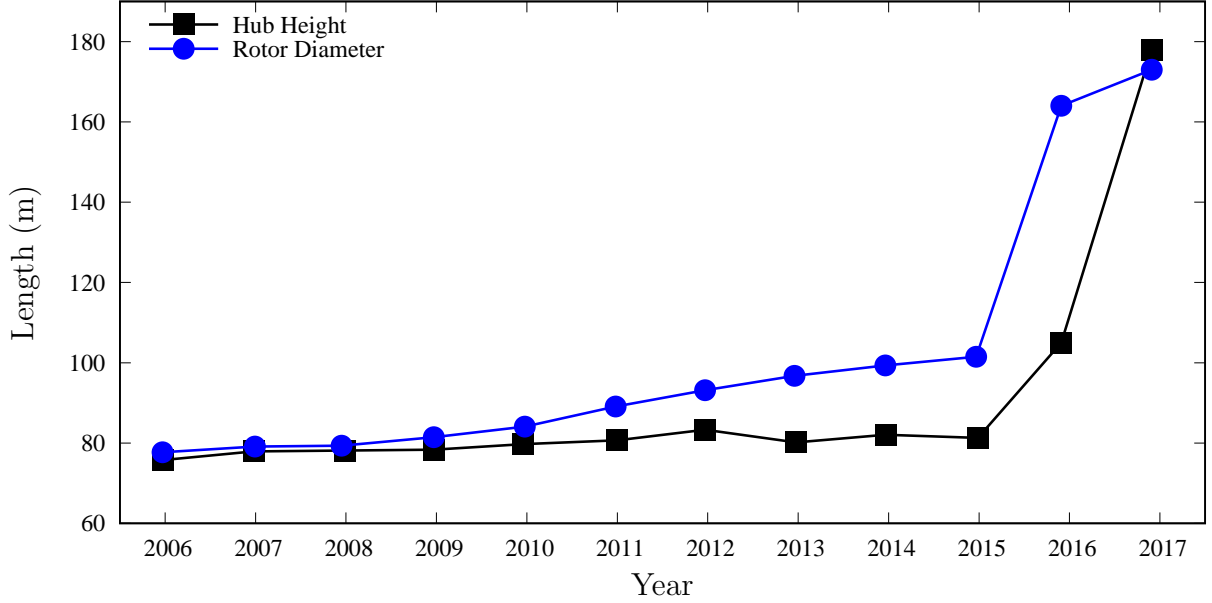


Figure 1.2. Average turbine rotor diameter and hub height installed during period. 2015 Wind technologies market report [2].

turbulence induced by the terrain or in the atmosphere can change the transport of kinetic energy in the wakes affecting the overall efficiency of the power plant. The power production is also affected by the atmospheric stability. The atmospheric conditions change significantly through a diurnal cycle. Stable conditions are encountered during the night while having buoyancy driven structures during the day.

To address the problems mentioned above, wind farm designers rely on simple engineering wake models for determining the wind turbine layout in a plant and control strategies [8, 9, 10]. These tools are based on simplified assumption to reduce the computational cost and produce good results faster than high fidelity simulations. Improvements over these models have been made with the help of high fidelity simulations and experimental measurements by fine-tuning parameters such as the mixing length or through reduced order models [11, 12, 13]. Nevertheless, the accuracy of these methods still depends on the quality of the experimental and numerical data used to tune the model.

More accurate results are obtained using large eddy simulation (LES) solvers coupled with the actuator disk model (ADM) [14] or the actuator line model (ALM) [15]. These models mimic the turbine by computing the forces exerted by each individual blade, similar to the blade element momentum (BEM) theory, using the measured local velocity obtained from the LES. The forces are applied to the Navier-Stokes equation by resembling the rotor disk (ADM) or each individual blade (ALM).

The coordination between conventional and wind power plants is essential for the stability and reliability of the electrical grid system. Therefore, it is imperative to determine the performance, power production and variability of wind energy plants under different weather conditions. To provide more realistic atmospheric conditions, wind farm parameterizations have been integrated into numerical weather prediction (NWP) models [16, 17]. This allows to study the performance of the wind farm through a diurnal cycle [18] encompassing stable and unstable atmospheric conditions or through the evening transition [19]. As a limiting factor of the parameterization is that the mesoscale modeling is limited to grid size larger than 1 km , therefore impeding the modeling of the wind turbine interaction of turbines located in the same mesh point.

In this dissertation Large Eddy Simulations of flow past wind turbines are performed with the objective of improving high fidelity models of turbines, providing an accurate description of their wakes and of their power production. In chapter 2, details of the numerical discretization of the governing equations are given. To improve the wind turbine modeling, a high-resolution LES was performed where the effect of the tower and nacelle was studied (Chapter 3). In chapter 4 it is studied the effect of the topography, on the performance of a wind turbine. Chapter 5 an assessment of nested mesoscale to microscale simulations using the Weather and Research Forecast model (WRF) against LiDAR and SCADA data is discussed. A modification to the parameterization is proposed in order to model the wind

turbines in grids smaller than 1 km, allowing to study wake interactions between turbines. Coupling between the WRF simulations with high fidelity wind turbine simulations using the actuator disk model is discussed in Chapter 5. Closing remarks are given in Chapter 6.

1.1 Intellectual Merit

For the design and development of wind farm control systems is of great importance to accurately simulate the wind turbine wake and energy entrainment, specifically for those operating in the wake of a windward turbine [20]. In this work we studied for the first time the interference between the wake of the tower and nacelle and that of the rotor. For the first time, we considered the effect of a wavy topography on the power production and its fluctuations and on the loads on the blade. Finally, we were able to couple our high fidelity wind turbine code with numerical weather prediction models. This novel numerical tool allowed us to reproduce the wind field over a real wind farm, accounting for wind speed and wind direction variability.

1.2 Broader Impact

Mitigating wake interaction losses can potentially improve the power production of a wind farm and reduce the total cost of wind energy production. More importantly, wind is a clean renewable energy source that contributes in reducing the dependence from fossil fuels. Consequently, it will reduce the production of air pollutants and greenhouse gases, such as sulfur dioxide, nitrogen dioxide carbon dioxide and nitric oxide and other particulate matter. Wind energy can also reduce the use of clean water that is required for the transport of energy on conventional power plants. For example, the Department of Energy has set the goal of producing 20% of the total energy by wind energy by 2030. This would save up to 260 billion gallons of water by 2050 [1].

CHAPTER 2

METHODOLOGY AND MODELING

2.1 Governing Equations

The governing equations that describe the motion of a fluid past wind turbines are the incompressible Navier-Stokes and conservation of mass equations,

$$\frac{\partial U_i}{\partial t} + \frac{\partial U_i U_j}{\partial x_j} = -\frac{\partial P}{\partial x_i} + \frac{1}{Re} \frac{\partial^2 U_i}{\partial x_j \partial x_j} + F_i, \quad (2.1a)$$

$$\frac{\partial U_i}{\partial x_i} = 0, \quad (2.1b)$$

$$U_i = \frac{U_i^*}{U_\infty}, \quad (2.1c)$$

$$t = \frac{t^* D}{U_\infty}, \quad (2.1d)$$

$$P = \frac{P^*}{\rho U_\infty^2}, \quad (2.1e)$$

where U_i is the velocity along the i direction, P is the pressure, U_∞ is the reference velocity and D is the rotor diameter. Since the resolution needed to describe the turbine blades, especially at their tip is beyond our reach with the computer power available nowadays, the turbines are modeled with a virtual force F_i . The Reynolds number is given by $Re = U_\infty D / \nu$, where ν the kinematic viscosity.

2.2 Discretization of the Navier-Stokes Equations

The Navier-Stokes equations are a system of non-linear second order partial differential equations. Due to their complexity, an analytical solution exists for a small number of cases and for cases as those of interest in this dissertation, equations need to be discretized. In this work the Navier-Stokes equations are discretized using a central second-order finite-difference. The scheme is based on a fractional step and factorization method, second order

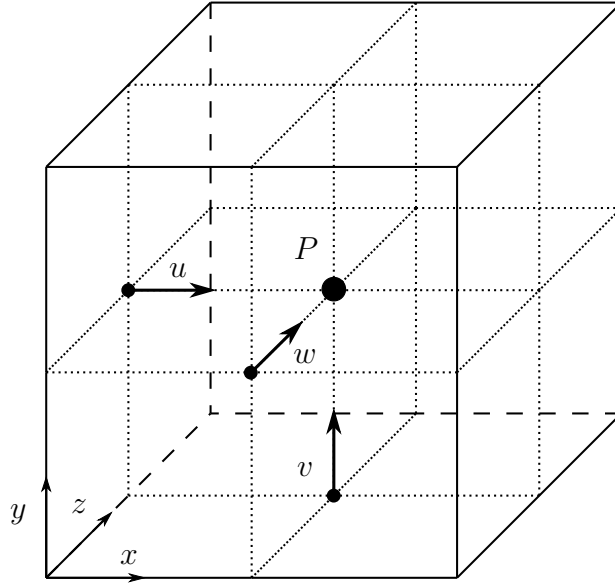


Figure 2.1. Computational cell with pressure computed in the cell center and staggered velocity in the cell faces

accurate in space and time. To keep the differential operators as compact as possible, a staggered grid was employed. The velocities are defined in the faces of the cell and the pressure in the center (Figure 2.1).

2.2.1 Time Discretization

For the integration in time we use a low-storage Runge-Kutta method originally developed by Wray [21]. This method provides a 3rd order of accuracy in time with good stability properties. It requires 3 sub-steps and only 2 memory spaces, therefore being low-storage. Let us consider a general differential equation:

$$\frac{\partial U}{\partial t} = f(U, t). \quad (2.2)$$

The method must satisfy the following requirements:

- New time is approximated by the Taylor series for successive times;

Table 2.1. Low-Storage Runge-Kutta scheme

First Memory Location	Second Memory Location
$U^0 = U^n$	$f^0 = f^n$
$U^1 = U^0 + a\Delta t f^0$	$U^A = f^0 + A\Delta t f_0$
$U^2 = U^1 + b\Delta t f(t^l + A\Delta t, U^A)$	$U^B = U^1 + B\Delta t f(t^l + A\Delta t, U^A)$
$U^3 = U^2 + c\Delta t f(t^l + (a + B)\Delta t, U^B)$	-

- Only two memory locations are available per dependent variable U , and consequently $f(U, t)$;
- the operation must be cyclic, therefore containing the necessary quantities on the end of a time-step for the next iteration.

Given the conditions above, the initial memory locations are

$$U^n | f(U^n, t^n). \quad (2.3)$$

The only dimensionless group for a given U^l is $f(U^l, t^l)\Delta t^l/U^l$, therefore the only possible approximation is $F(f(U^l, t^l)\Delta t^l/U^l)U^l$. The Taylor series requirement implies that F must be linear, therefore it can be written as

$$U^l + a\Delta t f(U^l, t^l), \quad (2.4)$$

and similarly, for the second memory location,

$$U^l + A\Delta t f(U^l, t^l). \quad (2.5)$$

This procedure is repeated l -times until the desired accuracy is obtained. Table 2.1 summarize the third-order low storage Runge-Kutta scheme.

Substituting the expression for U^1 and U^2 into U^3 , the third-order scheme is given by

$$U^{n+1} = U^n + a\Delta t f(U^n, t^n) + b\Delta t f(U^A, t^n + A\Delta t) + c\Delta t f(U^B, t^n + (a + B)\Delta t). \quad (2.6)$$

To determine the unknown coefficients, the new time is approximated by the Taylor series, which is

$$U^{n+1} = U^n + \Delta t \frac{\partial U}{\partial t} + \frac{\Delta t^2}{2} \frac{\partial^2 U}{\partial t^2} + \frac{\Delta t^3}{6} \frac{\partial^3 U}{\partial t^3} + O(\Delta t^4). \quad (2.7)$$

By matching the coefficients of the two relations, a system of equation allows to determine the unknowns, given by

$$a + b + c = 1, \quad (2.8a)$$

$$(a + B)c + Ab = 1/2, \quad (2.8b)$$

$$(a + B)^2 c + A^2 b = 1/3, \quad (2.8c)$$

$$ABc = 1/6. \quad (2.8d)$$

Having five unknowns and four equations a common solution is obtained by setting $b = 0$, which gives

$$a = 1/4,$$

$$A = 8/15,$$

$$B = 5/12,$$

$$c = 3/4.$$

The momentum equation is simplified to a single function for the development of the time integration above. Nevertheless, this function can be further divided into the convective non-linear terms and the viscous linear terms as such

$$\frac{\partial U}{\partial t} = N(U) + L(U), \quad (2.10)$$

where $N(U)$ is the non-linear terms and $L(U)$ is the linear terms. To eliminate the numerical viscous stability restriction, particularly at very low Reynolds number and highly stretched

meshes near boundaries, the viscous terms will be advanced implicitly using the Crank-Nicolson scheme in each Runge-Kutta step. On the other hand, the non-linear terms are advanced explicitly, obtaining

$$U^1 = U^0 + \gamma^1 \Delta t N^0 + \rho^1 \Delta t N^{-1} + \alpha^1 \Delta t \frac{L^1 + L^0}{2}, \quad (2.11a)$$

$$U^2 = U^1 + \gamma^2 \Delta t N^1 + \rho^2 \Delta t N^0 + \alpha^2 \Delta t \frac{L^2 + L^1}{2}, \quad (2.11b)$$

$$U^{n+1} = U^3 = U^1 + \gamma^2 \Delta t N^1 + \rho^2 \Delta t N^0 + \alpha^2 \Delta t \frac{L^2 + L^1}{2}. \quad (2.11c)$$

From the initial conditions the values of a previous step are not known, therefore, we can conclude that $\rho^1 = 0$, and because the linear and non-linear terms must be at the same time-step, $\alpha^l = \gamma^l + \rho^l$.

Substituting into the final step all the previous Runge-Kutta steps we get

$$U^{n+1} = U^0 + \Delta t [(\gamma^1 + \rho^2) N^0 + (\gamma^2 + \rho^3) N^1 + \gamma^3 N^2]. \quad (2.12)$$

Comparing the equation above with equation 2.6 we can deduce that

$$a = \gamma^1 + \rho^2, \quad (2.13a)$$

$$b = \gamma^2 + \rho^3, \quad (2.13b)$$

$$c = \gamma^3. \quad (2.13c)$$

Considering that U^A was evaluated at time $t^n + A\Delta t$, U^B at $t^n + (a + B)\Delta t$ in function we get

$$A = \gamma^1 + \rho^1, \quad (2.14a)$$

$$a + B = \gamma^2 + \rho^2 + \gamma^1 + \rho^1. \quad (2.14b)$$

Solving this system of equations with five equations and five unknowns we get

$$\gamma^1 = 8/15, \quad \rho^1 = 0, \quad \alpha^1 = 8/15,$$

$$\gamma^2 = 5/12, \quad \rho^2 = -17/60, \quad \alpha^2 = 2/15,$$

$$\gamma^3 = 3/4, \quad \rho^3 = -5/12, \quad \alpha^3 = 1/3.$$

Then applying the discretization scheme to the momentum equation, it is obtained

$$\frac{\hat{U}_i^{l+1} - U_i^l}{\Delta t} = -\gamma^l N_i^l - \rho^l N_i^{l-1} + \frac{\alpha^l}{Re} L_{jj} \left(\frac{\hat{U}_{i+1}^l + U_i^l}{2} \right) - \alpha^l G_i P^l \quad (2.16)$$

where in this case L_{jj} represents the Laplacian operator that is calculated using central scheme difference and G_i the gradient operator.

Equation 2.16 is discretized around time $l + 1/2$ for the solution at time $l + 1$. The fact that the pressure term is only known at time l and is computed explicitly from this time, yields to the solution \hat{U}_i that is a non-solenoidal velocity field. As a consequence the field \hat{U}_i has to be corrected to obtain a divergence free velocity field. Introducing $\Delta U_i = \hat{U}_i - U_i^l$ into equation 2.16 we obtain

$$\left(1 - \frac{\alpha^l}{2Re} L_{jj}\right) \Delta U_i = -\gamma^l N_i^l - \rho^l N_i^{l-1} + \frac{\alpha^l}{Re} L_{jj} U_i^l - \frac{\delta P^l}{\delta x_i}. \quad (2.17)$$

This results in a sparse matrix of $N \times N$ with seven diagonals, where N is the amount of grid points. Inverting this matrix by standards methods, such as Gaussian elimination, requires a large amount of operations that may limit the amount of grid points. However, it is essential for dealing with turbulent flows and vortex dynamics to have fine grid resolutions. Therefore, the seven diagonal matrix is approximated by a three tri-diagonal matrices that are easily inverted. The three step factorization of equation 2.17,

$$\left(I - \frac{\alpha^l}{2Re} L_{11}\right) \Delta U_i^{**} = RHS, \quad (2.18a)$$

$$\left(I - \frac{\alpha^l}{2Re} L_{22}\right) \Delta U_i^* = \Delta U_i^{**}, \quad (2.18b)$$

$$\left(I - \frac{\alpha^l}{2Re} L_{33}\right) \Delta U_i = \Delta U_i^*. \quad (2.18c)$$

Equation 2.18 approximate equation 2.17 with an order of Δt^2 . The solenoidal field at the new step $l + 1$ is obtained by introducing a scalar quantity ϕ that projects the non-solenoidal field into a solenoidal space given by the following equation:

$$U^{l+1} = \hat{U} - \Delta t \frac{\delta \phi}{\delta x_i}, \quad (2.19)$$

$$\nabla \cdot \nabla \phi = \nabla^2 \phi = \nabla \cdot \hat{\mathbf{U}} = \frac{\partial \hat{U}_i}{\partial x_i}. \quad (2.20)$$

By solving Poisson equation (Equation 2.20), then the pressure field can be computed using the following equation

$$P^{l+1} = P^l + \phi - \frac{\Delta t \alpha^l}{2Re} L_{jj} \phi. \quad (2.21)$$

2.2.2 Stability of the Numerical Scheme

The numerical scheme shown in section 2.2.1 is known as the Hybrid third-order Runge-Kutta/Crank-Nicolson scheme. However, because the linear term is advanced using a second order of accuracy integration in time in each Runge-Kutta step the overall accuracy is reduced to second order. Despite decreasing the accuracy, the time integration stability is increased. The Courant-Friedrich-Lewis (CFL) condition is typically given by:

$$\left| \frac{U_i \Delta t}{\Delta x_i} \right| \leq 1, \quad (2.22)$$

which limits the distance a fluid *particle* travel in each time integration to be less or equal to the mesh width. The three-step Runge-Kutta method, increasing the stability, relax the constraint imposed by the CFL condition to $CFL = \sqrt{3}$. A further advantage of this method is that $\rho_1 = 0$, which allows for a perfect restart without previous times needed for the integration.

2.3 Sub-grid Stress Modeling

Resolving all the scales of turbulent motions, via Direct Numerical Simulations (DNS), provides the most accurate representation of turbulent flows. In order to do so, it is required to solve the largest energetic scales and, at the same time, the smallest scales where all the turbulent kinetic energy dissipation occurs. Therefore, to resolve the smallest scales

the computational grid size must be no larger than the smallest scales also known as the Kolomogorov scale, η .

For homogeneous isotropic turbulence the number of grid points in each direction must be greater than L/η , where L is the distance over which the velocity fluctuations remains correlated. It can be shown that [22]:

$$\frac{L}{\eta} = \mathcal{O}(Re^{3/4}). \quad (2.23)$$

Although the majority of flow of interest cannot be considered homogeneous isotropic this equation gives a good estimate for the amount of required grid points. Considering that modern utility wind turbines have a rotor diameter of around 100 *m* and designed for wind speeds of around 10 *m/s* the Reynolds number is $Re_D = \mathcal{O}(10^8)$. Thus, it can be estimated that the minimum of grid points required for solving the smallest scales is of $\mathcal{O}(10^{18})$ for a three-dimensional field, that with nowadays technologies is a prohibitive.

To overcome these difficulties only the large scales of the flow are solved while the finer scales are filtered. This reduces the number of grid points and then the computational cost. This methodology is known as Large Eddy Simulation (LES). The filter operation is defined by

$$\tilde{U}_i(x_i, t) = \int G(r_i, x_i) U(x_i - r_i, t) dr_i, \quad (2.24)$$

where \tilde{U}_i is the filtered, resolved, velocity vector and G is the filter function. The residual field is defined by

$$u'_i(x_i, t) \equiv U(x_i, t) - \tilde{U}_i(x_i, t). \quad (2.25)$$

By introducing equation 2.25 into the Navier-Stokes equation 2.1 it is obtained the filtered Navier-Stokes and continuity equations

$$\frac{\partial \tilde{U}_i}{\partial t} + \frac{\partial \tilde{U}_i \tilde{U}_j}{\partial x_j} = -\frac{\partial \tilde{P}}{\partial x_i} + \frac{1}{Re} \frac{\partial^2 \tilde{U}_i}{\partial x_j \partial x_j} - \frac{\partial \tau_{ij}}{\partial x_j}, \quad (2.26a)$$

$$\frac{\partial \tilde{U}_i}{\partial x_i} = 0, \quad (2.26b)$$

where τ_{ij} is the sub-grid scale (SGS) stress tensor that represents the interaction between the large resolved scales with the unresolved ones.

The sub-grid scale stresses are parameterized using the eddy-viscosity model as

$$\tau_{ij} - \frac{1}{3}\delta_{ij}\tau_{kk} = -2\nu_T\tilde{S}_{ij}, \quad (2.27)$$

where \tilde{S}_{ij} is the filtered strain rate tensor ($\tilde{S}_{ij} = 1/2 \left(\partial\tilde{U}_i/\partial x_j + \partial\tilde{U}_j/\partial x_i \right)$) and δ_{ij} is Kronecker delta that represents the identity matrix. The Smagorinsky model is used for the eddy viscosity ν_T , and is given by

$$\nu_T = (C_s\Delta)^2 \sqrt{2\tilde{S}_{ij}\tilde{S}_{ij}}, \quad (2.28)$$

where Δ is the filter width and C_s is a non-dimensional parameter known as the Smagorinsky constant.

2.4 Immersed Boundary Method

The solid interfaces such as the tower, nacelle and topography are modeled with the Immersed Boundary Method. The technique consists of imposing a zero velocity, $U_i = 0$, in the grid points inside the solid boundary (\times in Figure 2.2). The derivatives in the Navier-Stokes equations are discretized using the distance between the “immersed” body and points where the velocities are defined on the Cartesian grid (\times , Figure 2.2). This prevents the body to be modeled as a stepwise geometry. More details are given in [23]. The present Immersed Boundary Method has been extensively validated in studies over rough walls [23, 24, 25].

Immersed Boundary Method may be interpreted as body forces added to the Navier-Stokes equation (as shown by Fadlun et al. [26]), similarly to the Actuator Line Model:

$$\frac{u_i^{n+1} - u_i^n}{\Delta t} = RHS^{n+1/2} + F_{IB,i}^{n+1/2}, \quad (2.29)$$

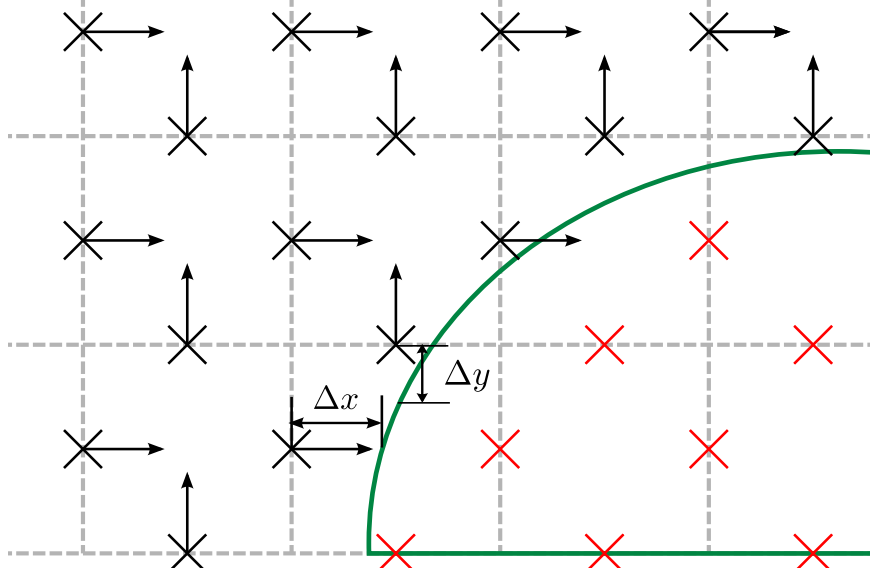


Figure 2.2. Geometrical sketch of the grid around a section of the tower. The arrows indicate the position in the grid where the velocities are defined (staggered). The velocities inside the body (x in red) are set to zero. The derivatives of the velocities at the closest points around the boundary are computed using the real distance to the body (Δx and Δy) and not the grid spacing. The latter would result in a stepwise body.

where RHS is the sum of the viscous terms, non-linear terms and pressure gradient and $F_{IB,i}$ is the Immersed Boundary force. Since the tower and nacelle do not move and then $u_i^n = 0$, the force $F_{IB,i}$ is calculated as

$$F_{IB,i}^{n+1/2} = -RHS^{n+1/2}, \quad (2.30)$$

to obtain zero velocity in the grid points inside the body. It would be ideal to use Immersed Boundaries for the entire blade given to the accuracy of the method. However, this would require a very fine grid to describe the tip of the blade and its camber. While this may not be critical for the drag, it is for the circulations and then for the lift. A grid that would resolve accurately the blade with Immersed Boundary is beyond our reach. Therefore, it is preferred to use the Actuator Line or Actuator Disk Model for the blades and the Immersed Boundary Method for the tower and nacelle (which are bluff bodies).

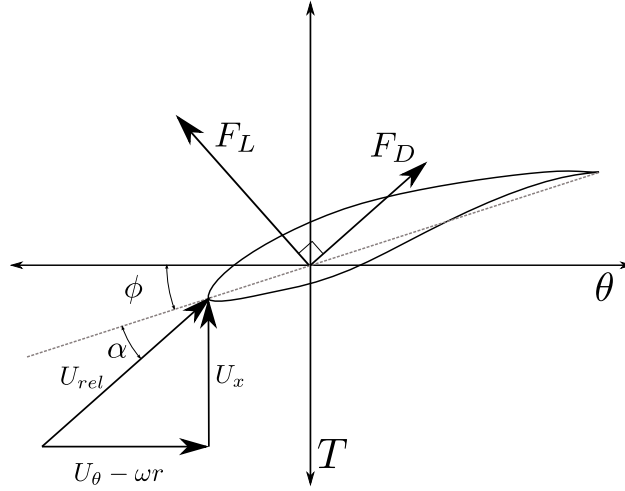


Figure 2.3. Blade cross-section in the plane $T - \theta$, where T is the direct ion of the thrust force and θ is the azimuthal direction.

2.5 Turbine Modeling

The wind turbine blades are modeled using the Actuator Line Model (ALM) developed by Sørensen et al. [27]. The lift F_L and drag F_D of the blades are computed using blade element theory for a two dimensional airfoil and are given by

$$F_L = \frac{1}{2} C_L(\alpha) \rho U_{rel}^2 c F, \quad (2.31)$$

$$F_D = \frac{1}{2} C_D(\alpha) \rho U_{rel}^2 c F, \quad (2.32)$$

where ρ is the flow density, C_L and C_D are the lift and drag coefficient which are function of the angle of attack, α , of the airfoil, c is the chord length of the airfoil, F is the Prandtl correction factor. The relative velocity, U_{rel} , is given by:

$$U_{rel} = \sqrt{U_x^2 + (U_\theta - \omega r)^2}, \quad (2.33)$$

U_x and U_θ denotes the streamwise and azimuthal flow velocity respectively, ω is the angular velocity of the rotor and r the radial distance from the center of the rotor (Figure 2.3). The

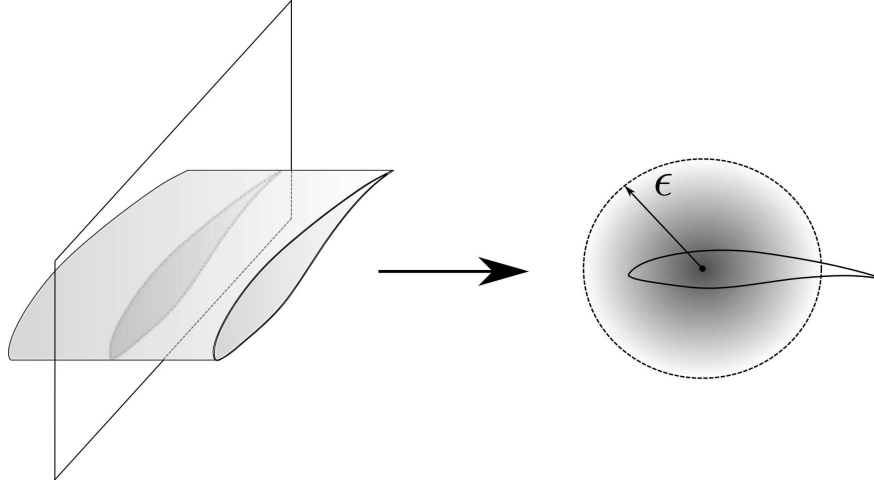


Figure 2.4. Sketch of the distribution of the aerodynamic load along the plane of the blade section.

lift and drag coefficient are obtained from a look-up table by computing the local angle of attack of each airfoil section

$$\alpha = \tan^{-1} \left(\frac{U_x}{U_\theta - \omega r} \right) - \phi_t, \quad (2.34)$$

where ϕ_t is the local twist of the blade. Since using look up tables of 2D airfoils neglects three dimensional effects of the blade, a modified Prandtl correction factor [28] is used to account for the tip and root vortex:

$$F = \left(\frac{2}{\pi} \right)^2 \cos^{-1} (e^{-f_t}) \cos^{-1} (e^{-f_r}), \quad (2.35)$$

where

$$f_t = \frac{B}{2} \frac{D/2 - r}{r \sin(\alpha + \phi_t)}, \quad (2.36)$$

and

$$f_r = \frac{B}{2} \frac{r - D_h/2}{r \sin(\alpha + \phi_t)}, \quad (2.37)$$

where D_h is the hub diameter and B is the number of blades of the wind turbine. The calculated aerodynamic forces are distributed in the perpendicular direction to each actuator

line with a Gaussian distribution kernel shown below

$$\eta_L = \frac{1}{\epsilon^2 \pi} \exp \left[- \left(\frac{r_\eta}{\epsilon} \right)^2 \right], \quad (2.38)$$

where r_η is the radial distance from the center of the blade and ϵ determines the spreading of the forces (Figure 2.4). It must be remarked from the previous equation that the actuator line consists of a *continuous* line instead of discrete actuator points as it has been done in the past by Martínez-Tossas et al. [3].

Instead of distributing the aerodynamic forces in a line, the forces can also be distributed over the rotor disk. The method is referred to as the rotating Actuator Disk Model (ADM) [29] and the forces are distributed as

$$\eta = \exp \left[- \left(\frac{x - x_c}{\epsilon} \right)^2 \right] \exp \left[- \left(\frac{\theta - \theta_B}{\pi/3} \right)^2 \right], \quad (2.39)$$

$$\eta_D = \frac{\eta}{\int \int_A \eta dA}, \quad (2.40)$$

where $x - x_c$ is the relative distance from the position of the rotor x_c , $\theta - \theta_B$ is the relative angular distance from the angular position of the blade θ_B . The ADM model requires less grid points and allows a larger integration time steps than the ALM reducing the computational cost. However the space resolution is coarser and the effect of the blade is spread over a large area thus preventing the formation of tip vortices.

CHAPTER 3

THE WAKE OF THE TOWER AND NACELLE¹

3.1 Introduction

In this chapter we quantify the effect of tower and nacelle on the wake of a wind turbine. Results have been published in Santoni et al. [30] and visualizations of the wake were featured in the cover of the journal *Wind Energy* [31]. The numerical code combines an ALM, for the rotating blades, with an immersed boundary method [23] used to model the tower and nacelle. Two sets of simulations, with and without tower and nacelle have been performed at two tip speed ratios: $\lambda = 3$ and 6. Results are compared with the experimental measurements (Krogstad et al. [4]) and with the numerical results obtained by Martínez-Tossas et al. [3] using OpenFOAM and the ALM.

3.1.1 Literature Review

To date the most accurate model to resolve the flow around a rotating blade is the Actuator Line Model, which mimics each individual blade with a body force along a line [15]. The lift and drag forces at each section of the blade are computed using look-up tables of the airfoil aerodynamic coefficients and spread over a few grid-points generally with a Gaussian function of width ϵ . The velocity obtained solving the Navier-Stokes equation is used to determine the velocity and angle of attack at each element of the blade.

Numerical results using the Actuator Line Model depend on the smearing factor, grid resolution, correction of the azimuthal and thrust force due to the tip and root losses and on the

¹©2018 WILEY. Portions Adapted, with permission, from Santoni, C., K. Carrasquillo, I. Arenas-Navarro, and S. Leonardi. (2017) “Effect of tower and nacelle on the flow past a wind turbine.” *Wind Energy* 20 (12), 19271939.

point with respect to the blade section where the relative velocity and angle of attack are calculated. Efforts have been made to quantify the effect of these parameters on the power production. For example, Martínez-Tossas et al. [3] found an optimal value of the smearing factor, ϵ , with respect to grid resolution $\epsilon/\Delta x \approx 2.5$. Jha et al. [32] proposed a smearing factor dependent on the geometry of the turbine blade. This is further corroborated by Martínez-Tossas *et al.* [33], who found that the optimal smoothing width is correlated to the chord of the blade, c , and it should be in a range $\epsilon/c \simeq 0.14 - 0.25$, while the center of the force distribution should be about $0.14 - 0.25c$ downwind the leading edge of the airfoil.

Much less attention had been paid to the effect of tower and nacelle. In general, wind turbines are modeled as rotating blades only. More recently, attempts have been made to model the tower and nacelle with body forces [34, 35]. For example Sarlak et al. [35] used a drag coefficient $C_D = 1.2$ and a lift coefficient which oscillates in time with a Strouhal number $St = 0.2$ and an amplitude $A = 0.3$ to model the tower of the turbine. Krogstad et al. [4] and Pierella et al. [36] compared numerical results obtained with different codes and turbine models with experimental measurements. The disk and line actuator models agreed better with the experimental data although the lack of the tower and nacelle resulted in a symmetric wake with a high velocity jet in the center of the rotor not observed in the measurements. In a recent paper, Mittal et al. [37] performed numerical simulations to reproduce the experiment done at NTNU (Norwegian University of Science and Technology), using an unstructured in-house code to model tower and nacelle. The numerical results agreed well with the experiment even in the near wake. Therefore, the comparison between numerical results and experiments carried out at NTNU seems to indicate that tower and nacelle are not negligible especially in the near wake of the turbines.

A similar conclusion was also reached by Kang et al. [38] who modeled a hydrokinetic turbine using three different approaches: curvilinear immersed boundary method where all

the details of the turbine, including tower and nacelle were solved, ADM and ALM. Results compared well with those of Chamorro et al. [39]. The presence of tower and nacelle, through the curvilinear immersed boundary method, allowed to reproduce with good accuracy the wake meandering and the interaction between the unstable hub vortex and the tip vortices as observed in the experiment. On the other hand, without modeling tower and nacelle, numerical results showed lower turbulent intensities, a stable hub vortex, which does not interact with the external shear layer, and a wake rotation extending much longer downwind.

3.2 Geometrical Configuration

The numerical simulations aim at reproducing the wind tunnel experiment of a single turbine performed at the Norwegian University of Science and Technology [40]. The turbine model has a three bladed rotor disk with diameter $D = 894mm$, the center being located at $817mm$ above the tunnel floor level. The tower consists of four cylinders of different diameters and lengths. From top to bottom, the cylinders diameters are $D_1 = 0.057D$, $D_2 = 0.068D$, $D_3 = 0.092D$ and $D_4 = 0.114D$ and the lengths of the cylinders are $L_1 = 0.208D$, $L_2 = 0.180D$, $L_3 = 0.267D$ and $L_4 = 0.197D$, respectively. The nacelle geometry is very similar to a capsule with radius of $0.05D$ and a total length of $0.64D$. The two-dimensional lift and drag coefficients of the NREL S826 airfoil, as well as the chord and twist angle along the span of the blade were obtained from [41].

The Reynolds number is $Re = 6.3 \times 10^5$, as in the experiment. The computational domain is $12.5D$ (length) \times $3D$ (width) \times $2.1D$ (height) where D is the rotor diameter. The hub is located at a height of $0.9D$, centered in spanwise direction and $4.1D$ from the inlet (Figure 3.1). No slip condition ($U_i = 0$) is prescribed at the tunnel walls (top, bottom and lateral boundaries of the computational box). A uniform velocity profile is given at the inlet

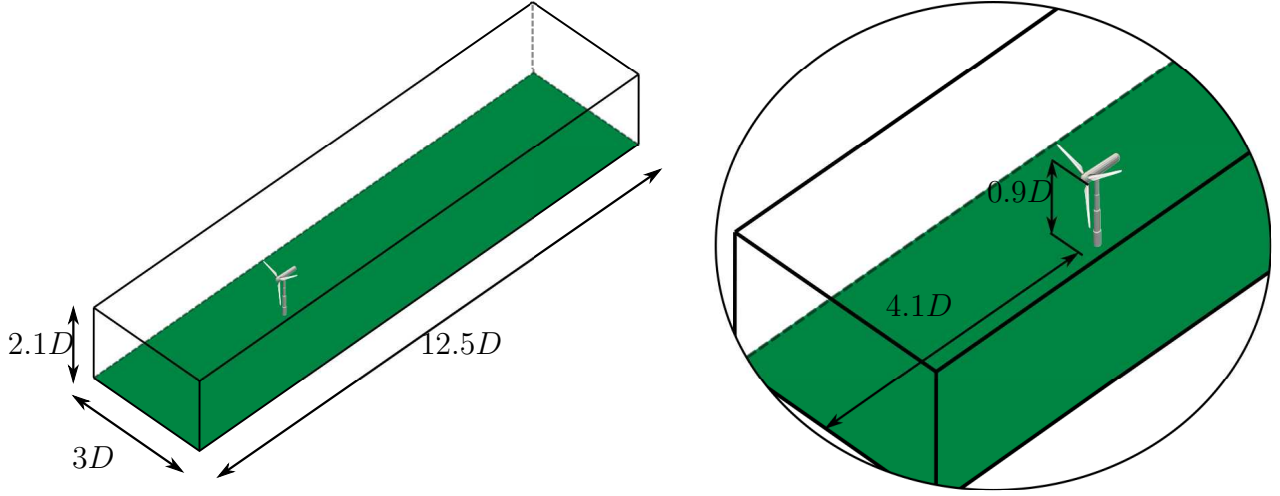


Figure 3.1. Computational box.

($U_\infty = 10\text{m/s}$) while radiative boundary conditions are imposed at the outlet:

$$\frac{\partial \tilde{U}_i}{\partial t} + C \frac{\partial \tilde{U}_i}{\partial n} = 0, \quad (3.1)$$

where C denotes the convection velocity. The Smagorinsky model with a constant $C_S = 0.09$ is used for the subgrid stresses.

Two different tip speed ratios are considered, $\lambda = \omega R/U_\infty = 3$ and 6. The tip speed ratios are chosen among those available from the experiment so as to have one off-design condition, $\lambda = 3$, with the blades in stall, and one as the optimum design condition, $\lambda = 6$. For each tip speed ratio, two sets of simulations, with and without tower and nacelle, were performed. The computational grid is $2048 \times 512 \times 512$ in the streamwise, spanwise and wall-normal direction, respectively. The rotor disk is discretized in 170 points in the spanwise direction and 243 in the wall normal direction. The smoothing width is $\epsilon = 0.03D$ corresponding to $\epsilon/c_R = 0.33$ at the root and $\epsilon/c_t = 1.03$ at tip, where c_R and c_T are the chord at the root and at the tip, respectively. This is slightly larger than the values recommended by Martínez-Tossas et al. [33] but decreasing it even further would have resulted in a grid unfeasible for our computational resources. The spreading $\epsilon/\Delta = 3.2$, where $\Delta = \sqrt{\Delta x^2 + \Delta y^2 + \Delta z^2}$,

is used to minimize the numerical oscillations on the blade, that were also observed by Martínez-Tossas et al. [3] and Troldborg [42].

3.3 Result and Analysis

Simulations were run for about 50 rotor revolutions (T) for $\lambda = 3$ and 100 for $\lambda = 6$. Each rotor revolution was discretized in 600 time steps for $\lambda = 3$ and 800 for $\lambda = 6$. In fact, because of the increased tip velocity for $\lambda = 6$, a smaller Δt is necessary to keep the CFL in the stability limit. The first $20T$ were discarded to eliminate the effect of the initial conditions. The data was recorded nearly every $T/5$ and $T/10$ times per revolutions for $\lambda = 3$ and 6, respectively. A convergence analysis showed that 200 snapshots were sufficient for the statistical convergence. However, all the snapshots obtained for each case were used for the analysis shown below.

3.3.1 Mean Flow

Color contours of the time averaged streamwise velocity (\overline{U}_1) in a vertical plane (x, y) at the center of the rotor disk are shown in Figure 3.2 for $\lambda = 3$ and 6. A velocity deficit can be observed behind the rotor disk due to the thrust force of the turbine, which increases by increasing the tip speed ratio. Similarly, the induction zone upwind the rotor becomes larger when the tip speed ratio increases. Because of the blockage caused by the turbine, the velocity near the upper smooth wall increases up to $\overline{U}_1 = 1.15U_\infty$ for $\lambda = 6$. When tower and nacelle are not modeled, an unphysical jet is generated at the center of the rotor disk, as stronger as larger is the tip speed ratio. This streak of high velocity flow persists for more than 3 diameters behind the rotor although as we move further downwind, the velocity gradient is smoothed out by the viscosity and the breakdown of the root vortex. The nacelle,

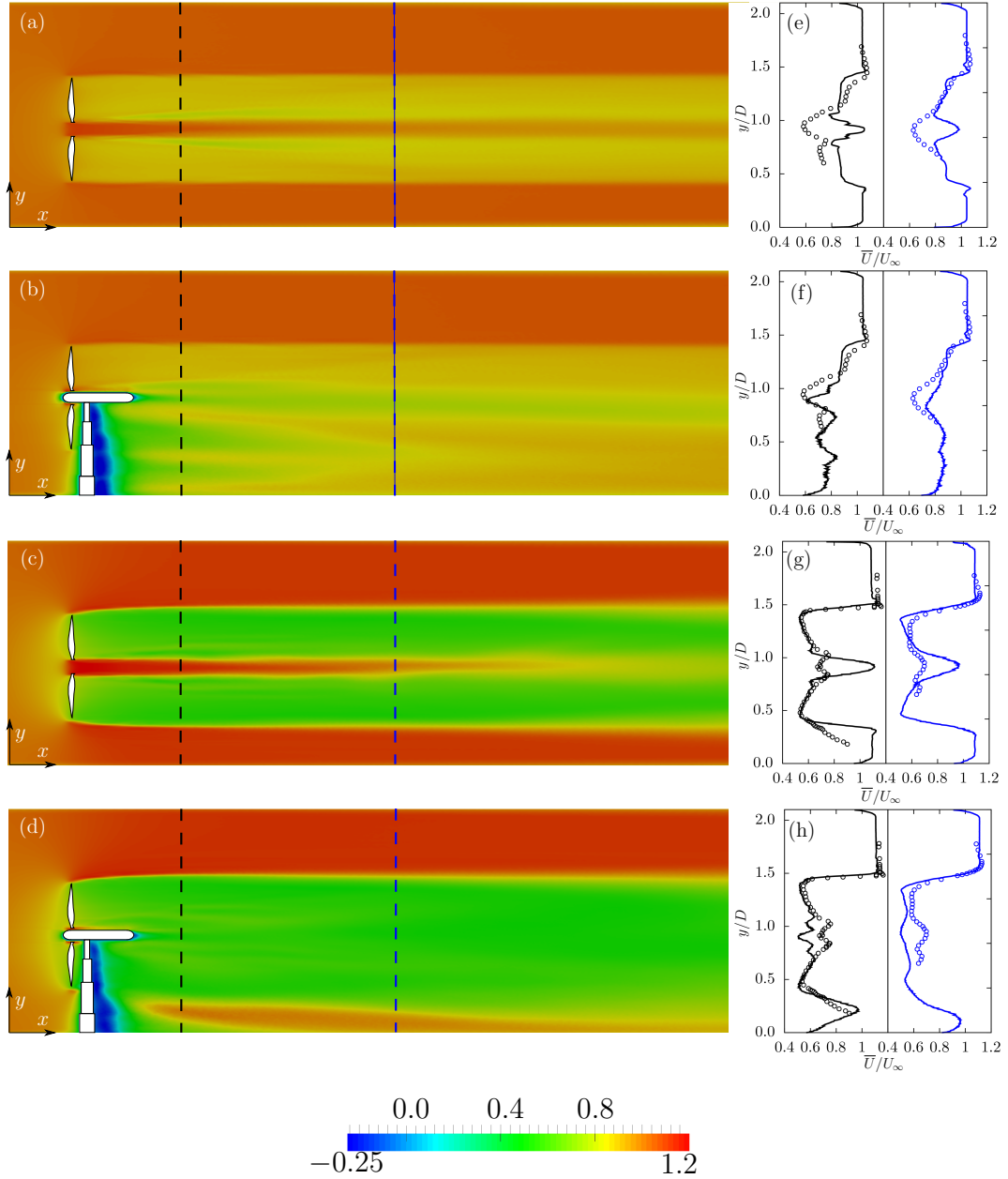


Figure 3.2. Contours of \bar{U}_1 in a vertical section; (a, b) $\lambda = 3$, (c,d) $\lambda = 6$, with (b,d), and without tower and nacelle (a,c); (e,f,g,h) vertical profiles of the mean streamwise velocity $1D$ (----) and $3D$ (----) downwind the rotor disk: LES results (—) and experiments (\circ).

instead, causes a momentum deficit, which is not aligned with the flow direction but tilted slightly downward. The wake behind the turbine without tower and nacelle is symmetric in the vertical direction with respect to the hub. The increase of streamwise velocity due to

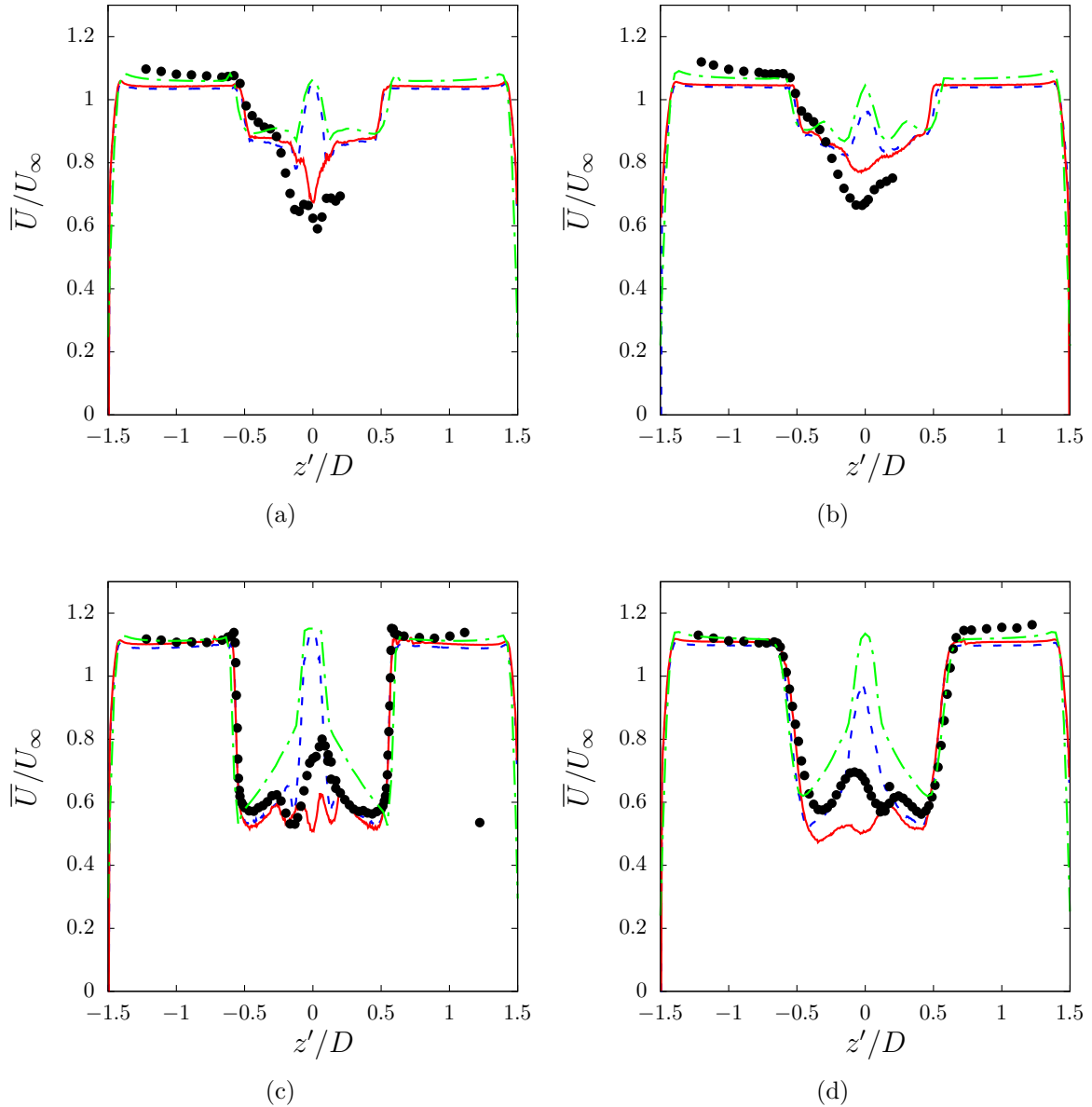


Figure 3.3. Time averaged streamwise velocity profiles: (a) $\lambda = 3$, $1D$ downwind, (b) $\lambda = 3$, $3D$ downwind, (c) $\lambda = 6$, $1D$ downwind, (d) $\lambda = 6$, $3D$ downwind: present simulations with (—) and without (---) the tower and nacelle, (— · —) numerical results from [3], and (•) experimental measurements [4].

the blockage is observed not only on the upper wall, as expected, but even on the lower wall. On the other hand, when tower and nacelle are modeled, the momentum in the lower part of the disk is much smaller. A reverse flow is observed behind the tower (Figure 3.2 b,d).

The size of the recirculation appears to be correlated with the diameter of the tower, which is larger closer to the ground and it decreases moving upward towards the nacelle.

Streamwise velocity profiles along the wall normal direction at $1D$ and $3D$ (as indicated by the dashed vertical lines) are compared with experimental measurements (Figure 3.2 e,f,g,h). On the upper part of the disk, $y/D \gtrsim 1$, numerical results agree well with experimental measurements for both sets of simulations (with/without tower and nacelle). When tower and nacelle are included in the simulation, the agreement with measurements is improved especially in the lower part of the disk ($y/D < 1$). The presence of the tower and the nacelle causes a lower momentum near the ground and prevents the formation of the jet in the center of the rotor. The velocity at the center of the rotor, $y/D = 0.91$, is slightly larger than that measured experimentally. This is believed to be due to the excessive dissipation caused by the sub-grid scale model behind the nacelle.

Time averaged streamwise velocity profiles along the spanwise direction (z' , with origin at the center of the hub) at hub height are shown in Figure 3.3. Results are compared with experiments [4] and with the numerical results of Martínez-Tossas et al. [3], at $x = 1D$ and $x = 3D$ behind the turbine rotor. Present results for the case without tower and nacelle are consistent with those of Martínez-Tossas et al. [3] for both $\lambda = 3$ and 6. The intensity of the jet at the hub is very similar while small differences are observed along the blade ($0.05 < |z'/D| < 0.5$) close to the rotor. However, the velocity in the present simulations without tower and nacelle at the hub height decreases faster than that in Martínez-Tossas et al. [3] farther away from the rotor, due to the correction for the root loss we applied to the Actuator Line Model. This creates a weaker vortex caused by the root of the blades which breaks down earlier allowing for mixing between the high and low momentum flow of the wake. The interaction between the tower and nacelle and the wake of the blades results in an asymmetric velocity profile similar to that measured experimentally. By increasing the

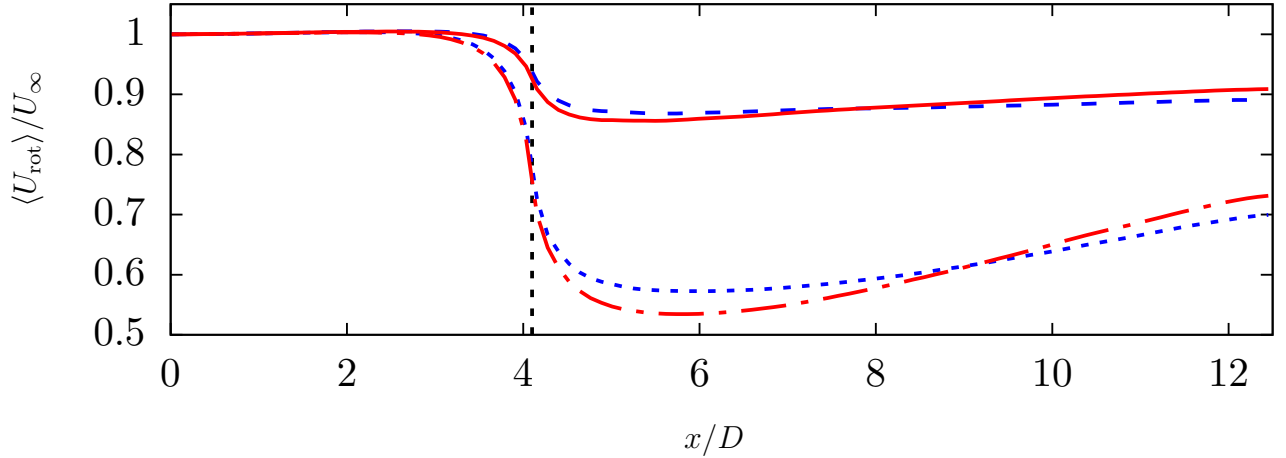


Figure 3.4. Streamwise velocity averaged in time and over the rotor disk, $\langle U_{\text{rot}} \rangle$: $\lambda = 3$ with (—) and without tower and nacelle (---); $\lambda = 6$ with (-·-) and without (····) tower and nacelle. The vertical dashed lines denote the position of the rotor.

tip speed ratio (i.e. the angular speed of the turbine) the asymmetry in the wake appears more evident and lasts longer in the wake.

The velocity profile over the blade is not significantly affected by the tower and nacelle with the exception of a small portion in the lowest part of its revolution. Therefore, the relative velocity and angle of attack (U_{rel} and α respectively) and as a consequence torque, thrust and power coefficients are quite accurately predicted even when only the rotating blades are modeled. However, in case of an array of turbines, the wake may impinge on downwind turbines. Since the wake characteristics may differ significantly, modeling the tower and nacelle can improve the prediction of the performance of wind turbine arrays. This is quantified in Figure 3.4 by showing how the velocity in the rotor swept area, $\langle U_{\text{RA}} \rangle$, varies with the streamwise distance, ($\langle U_{\text{RA}} \rangle = \frac{1}{A_{\text{rot}}} \int_{A_{\text{rot}}} \bar{U}_1 dA$, where A_{rot} is the rotor swept area and \bar{U}_1 is the time averaged streamwise velocity). The velocity in the rotor swept area decreases in correspondence of the location of the blades, $x/D = 4.1$, due to the drag force (thrust) caused by the turbine. To a larger drag, relative to a higher tip speed ratio,

corresponds a larger velocity deficit. Downwind the turbine, the rotor velocity increases (wake recovery) with a slope that depends primarily on the tip speed ratio. In fact, the swirl imparted by the rotating blades promotes the mixing and increases with increasing the tip speed ratio. The tower and nacelle increase further the velocity deficit in correspondence of the turbine (since there is no jet) and enhance the wake recovery by increasing entrainment of mean kinetic energy (as it is discussed in the next sections). The velocity, in the near wake of the turbine, is larger for the case without tower and nacelle because of the (unphysical) jet at the hub. However, due to the increased entrainment, about 4 – 5 diameters downwind the turbine, $\langle U_{RA} \rangle$ relative to the case with tower and nacelle overcomes that obtained with the rotating blades only.

3.3.2 Mean Kinetic Energy Entrainment

The increased recovery observed in Figure 3.4 is further corroborated by the budget of mean kinetic energy. The mean kinetic energy transport equation is:

$$\frac{\partial \bar{E}}{\partial t} = -\bar{U}_i \frac{\partial \bar{E}}{\partial x_i} - \frac{\partial}{\partial x_j} [\bar{U}_i \overline{u_i u_j} + \bar{U}_i \bar{\tau}_{ij}] + (\overline{u_i u_j} + \bar{\tau}_{ij}) \frac{\partial \bar{U}_i}{\partial x_j} + \bar{U}_i \bar{F}_i - \frac{\partial \bar{U}_i \bar{P} / \rho}{\partial x_i}, \quad (3.2)$$

where $\bar{E} = 1/2 \bar{U}_i \bar{U}_i$, τ_{ij} is the sum of the viscous and sub-grid stresses, P the pressure and \bar{U}_i and u_i are the mean velocity and fluctuation along the i direction, respectively. As shown in [43, 44], the dominating terms of equation (3.2) in the turbine region are the power extraction given by $\bar{U}_i \bar{F}_i$, where F_i is the forces exerted by the turbine, and the turbulent kinetic energy flux induced by the Reynolds stresses. The recovery of mean kinetic energy in the wake is mainly due to the turbulent kinetic energy flux which is given by the gradient of $-\bar{U}_i \overline{u_i u_j}$ where index j is along the radial direction [45].

Figure 3.5 shows the color contours of $-\bar{U} \overline{uw}$, which accounts for the entrainment of mean kinetic energy along the spanwise direction. Positive values (red) indicate a turbulent kinetic

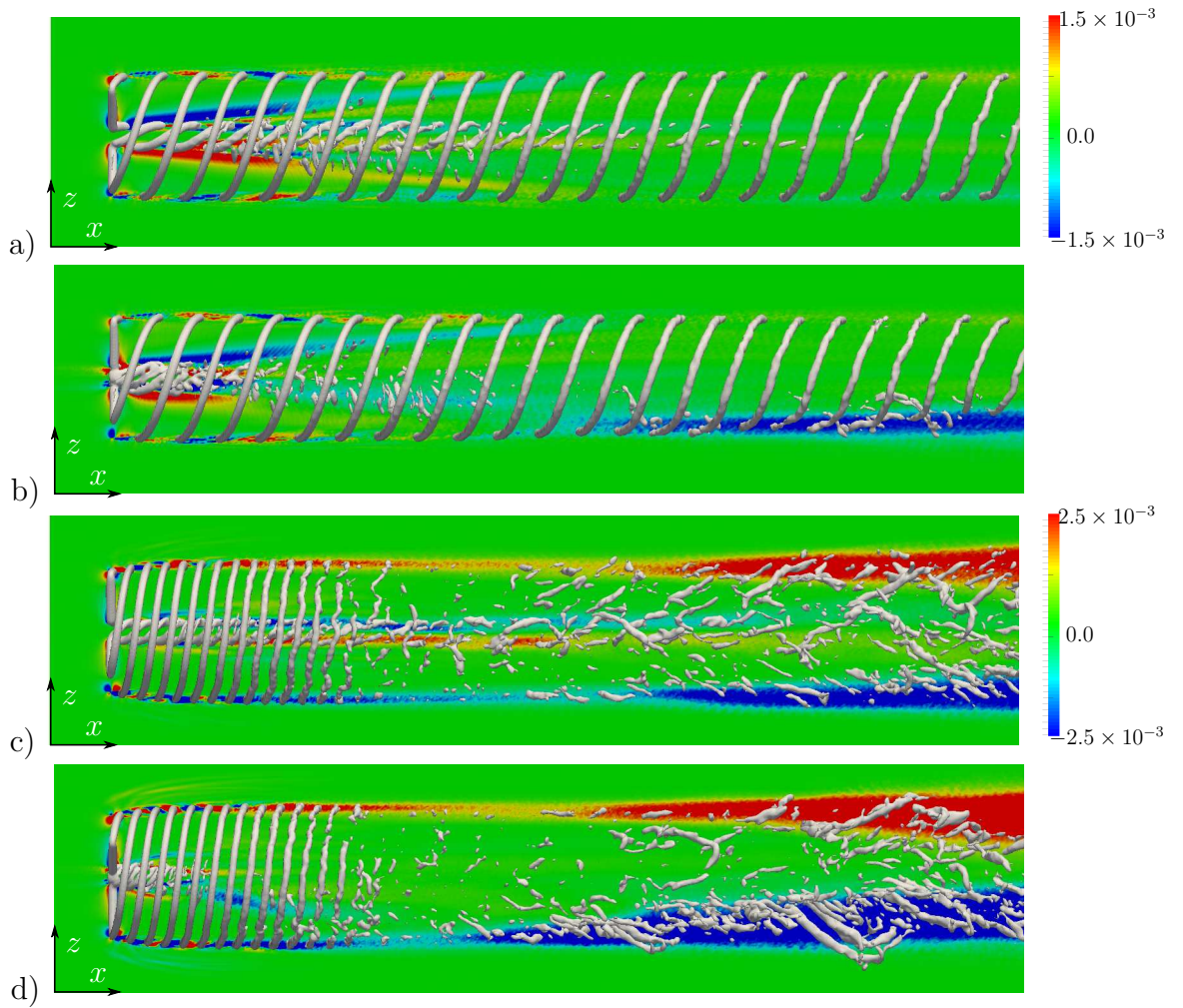


Figure 3.5. Iso-surface of λ_2 super-imposed to color contours of $-\overline{Uuuw}$ on a horizontal plane at hub height: $\lambda = 3$ (a,b), $\lambda = 6$ (c,d), with (b,d) and without (a,c) tower and nacelle (note that color ranges vary with tip speed ratio).

energy flux in the negative spanwise direction, while negative (blue) values denote a flux in the positive spanwise direction. For both set of simulations, by increasing the tip speed ratio, the entrainment of mean kinetic energy increases for a given streamwise distance from the rotor disk. At the tip of the blades, in the near wake, a weak flux of mean kinetic energy towards the center of the wake is caused by the tip vortex. A similar effect occurs at the center of the wake, due to the root vortex. By increasing the angular velocity, a stronger vortex and as a consequence a larger entrainment in the tip and root regions are obtained

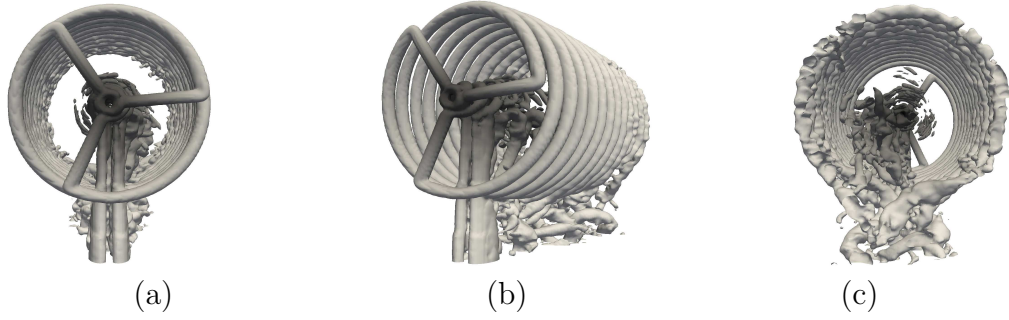


Figure 3.6. Iso-contours of $\lambda_2 = -3$ for a turbine with tower and nacelle (not shown in the figure for clarity) and tip speed ratio $\lambda = 6$; front (a), side (b) and back (c) views. The region closer to the turbine axis is colored darker.

(Figure 3.5c). Further downwind, in correspondence of the vortex breakdown, increased fluxes are observed on both sides of the wake. This is consistent with the observations of Lignarolo et al. [45], who showed that the increase in flux of mean kinetic energy corresponds to the breakdown of the tip vortex. For both tip speed ratios ($\lambda = 3, 6$), tower and nacelle enhance the entrainment of mean kinetic energy and break the symmetry of the wake and that of \overline{Uuw} with more energy being entrained from the side $z < z_{hub}$. This is more evident at $\lambda = 6$ because the swirl is larger.

3.3.3 Coherent Structures

Visualizations of iso-surfaces of λ_2 (Figure 3.5, 3.6), (second largest eigenvalue of $S_{ik}S_{kj} + \Omega_{ik}\Omega_{kj}$ [46], where $S_{ij} = 1/2(\partial U_i/\partial x_j + \partial U_j/\partial x_i)$ and $\Omega_{ij} = 1/2(\partial U_i/\partial x_j - \partial U_j/\partial x_i)$), show that the root vortex as well as the vortex shedding behind the tower are tilted towards one side of the wake for both tip speed ratios. A couple of diameters downwind the rotor disk, the vortices generated at the nacelle and tower get very close to the tip vortex and promote the vortex breakdown. On the other hand, when only the rotating blades are simulated (no tower and nacelle), the root vortex is aligned to the flow direction and does not interact significantly with the coherent structure at the tip (Figure 3.5a,c). When the vortical structure generated

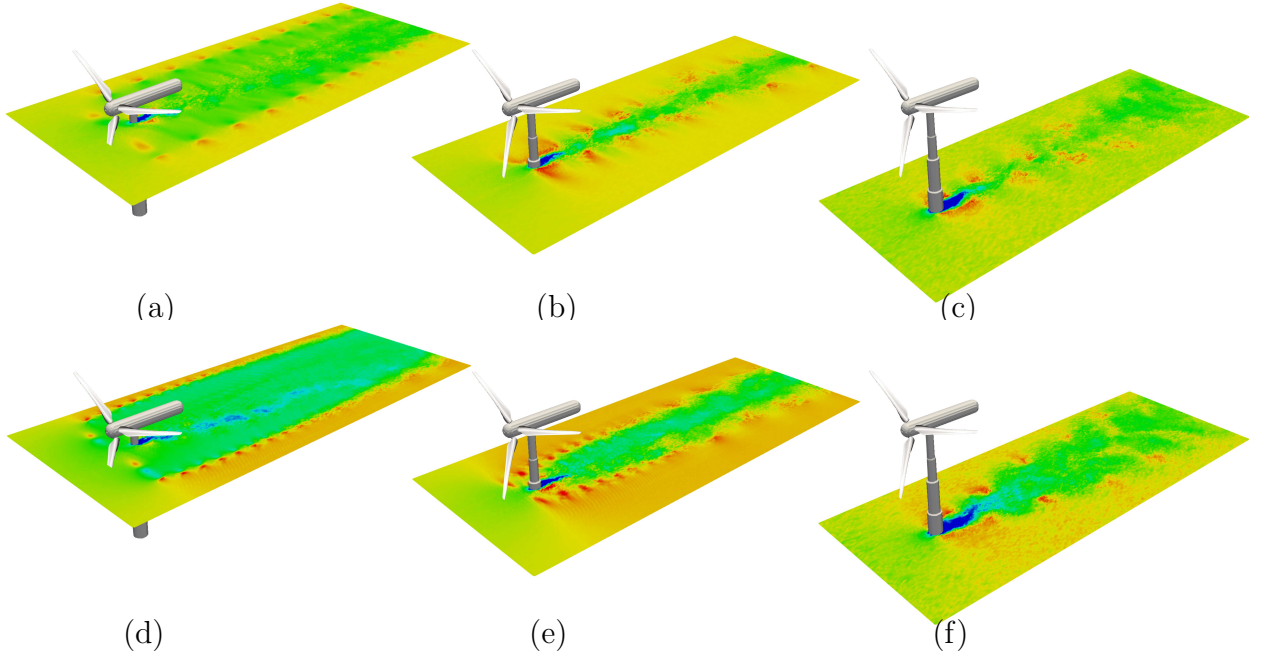


Figure 3.7. Color contours of instantaneous streamwise velocity in horizontal planes at $0.75D$ (a,d), $0.4D$ (b,e) and $0.01D$ (c,f) from the bottom wall. Top $\lambda = 3$, bottom $\lambda = 6$.

from tower and nacelle is close enough to the tip vortex, entrainment is largely increased and explains the asymmetry in the fluxes.

To further describe the interaction between the wake of the tower and nacelle and that of the turbine blades, contours of instantaneous streamwise velocity are shown in Figure 3.7 on horizontal planes at different heights ($0.01D$, $0.4D$ and $0.75D$). Below the rotor, a vortex shedding from the tower similar to that of a circular cylinder ([47]) is observed. In the section closer to the wall, which corresponds to the tower segment with the largest diameter, the Strouhal number ($St = fd/U_\infty$, where f is the vortex shedding frequency and d is the diameter of the section of the tower and U_∞ is the inlet velocity) is $St = 0.18$ for both $\lambda = 3$ and $\lambda = 6$. An additional simulation with only tower and nacelle (not shown here) had been performed as reference. The Strouhal number is very similar, denoting that the wake at the base of the mast is weakly affected by the rotating blades. Despite having a negligible effect on the Strouhal number, the blockage effect, caused by the rotor, increases

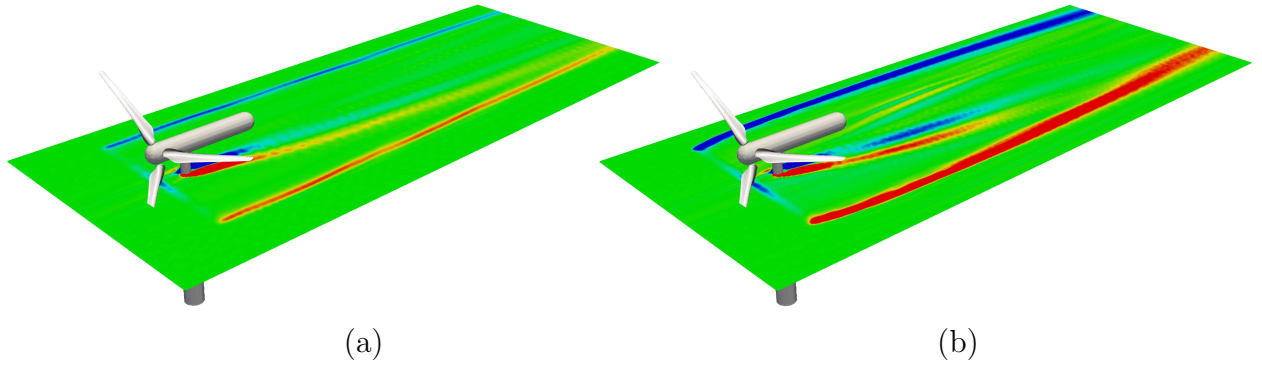


Figure 3.8. Color contours of the time averaged wall-normal vorticity, $\bar{\omega}_y$, in a horizontal plane located at $0.75D$ from the bottom wall: (a) $\lambda = 3$ and (b) $\lambda = 6$.

the (spanwise) separation of the vortices due to $\epsilon_{312}\tilde{U}_1\tilde{\omega}_2$ (Magnus effect) on the momentum equation ($\partial_j\tilde{U}_i\tilde{U}_j = -\epsilon_{ijk}\tilde{U}_j\tilde{\omega}_k + \partial_i 1/2\tilde{U}_j\tilde{U}_j$). Indeed, when $\lambda = 6$, because of the larger thrust coefficient and therefore the larger blockage, the vortices present a larger separation.

By moving upward, crossing the rotor disk, the Strouhal number (the reference velocity in the definition of the Strouhal number is the undisturbed inlet velocity for all the sections) for $\lambda = 6$ is reduced to $St = 0.16$ and $St = 0.1$ at $0.4D$ and $0.75D$, respectively, and to $St = 0.17$ and $St = 0.13$ for $\lambda = 3$. This is primarily due to the reduced momentum of the flow impinging the tower caused by the turbine. The decrease of the shedding frequency is correlated to the tip speed ratio. In fact, the larger is λ , the larger is the thrust force and induction zone, and therefore the smaller is the wind velocity. At $y/D = 0.4$ (Figure 3.7 b,e), for $\lambda = 3$ the vortex shedding of the tower prevails over the helicoidal tip vortex. For $\lambda = 6$, the tower splits the helicoidal vortex which is shed downwind similarly to a Kármán street. In the plane closer to the nacelle, at $y/D = 0.75$ (Figure 3.7 (a)), the imprint of the two tip vortices is observed on both sides of the turbine. The recirculation behind the tower is not aligned with the flow direction but rather tilted in the direction of the swirling flow as shown in the previous section. This is further corroborated by color contours of time averaged wall-normal vorticity $\bar{\omega}_y$ (Figure 3.8), where even though the tip vortex is farther away from the tower, the vortex is evidently stretched and twisted toward the tip vortex.

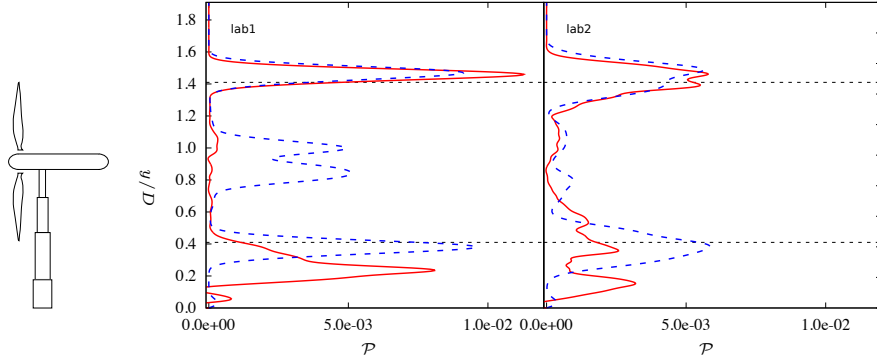


Figure 3.9. Profiles of turbulent kinetic energy production at $3D$ (left) and $6D$ (right) for $\lambda = 6$: with (—) and without (---) tower and nacelle. Horizontal dashed lines denote the highest and lowest points reached by the blade tip during its revolution.

3.3.4 Turbulent Kinetic Energy

Profiles of turbulent kinetic energy production, $\mathcal{P} = -\overline{u_i u_j} \partial \overline{U_i} / \partial x_j$, $3D$ and $6D$ behind the turbine along the wall-normal direction (y/D) are shown in Figure 3.9. When tower and nacelle are not modeled, regions of high production of turbulent kinetic energy are observed, as expected, at the tip of the blades but also at the hub height ($0.7 \leq y/D \leq 1.3$). The high turbulent kinetic energy production at hub height is due to the shear induced by the jet (see Figure 4 e.g). Moving downwind, at $6D$ from the turbine, velocity gradients decrease thus reducing the production at the tip of the blades. The shear due to the jet is weaker (as shown also in Figure 3.2) and production at the hub vanishes. Tower and nacelle do not affect much the production in the higher part of the rotor disk. On the other hand, at $3D$ downwind the rotor disk, there is no significant production of turbulent kinetic energy at hub height. In fact, the velocity profiles shown in Figure 3.2 reveal a very low shear at the nacelle despite its blockage. The peak of production generated by the tip of the blade in the lower part of the rotor is displaced downward closer to the wall. The production occurs over a larger area because the velocity field is smoother than that obtained without tower and nacelle. At $6D$ behind the turbine, in the lower part of the rotor, due to the enhanced mixing promoted by tower and nacelle, the production is reduced without a dominant localized region.

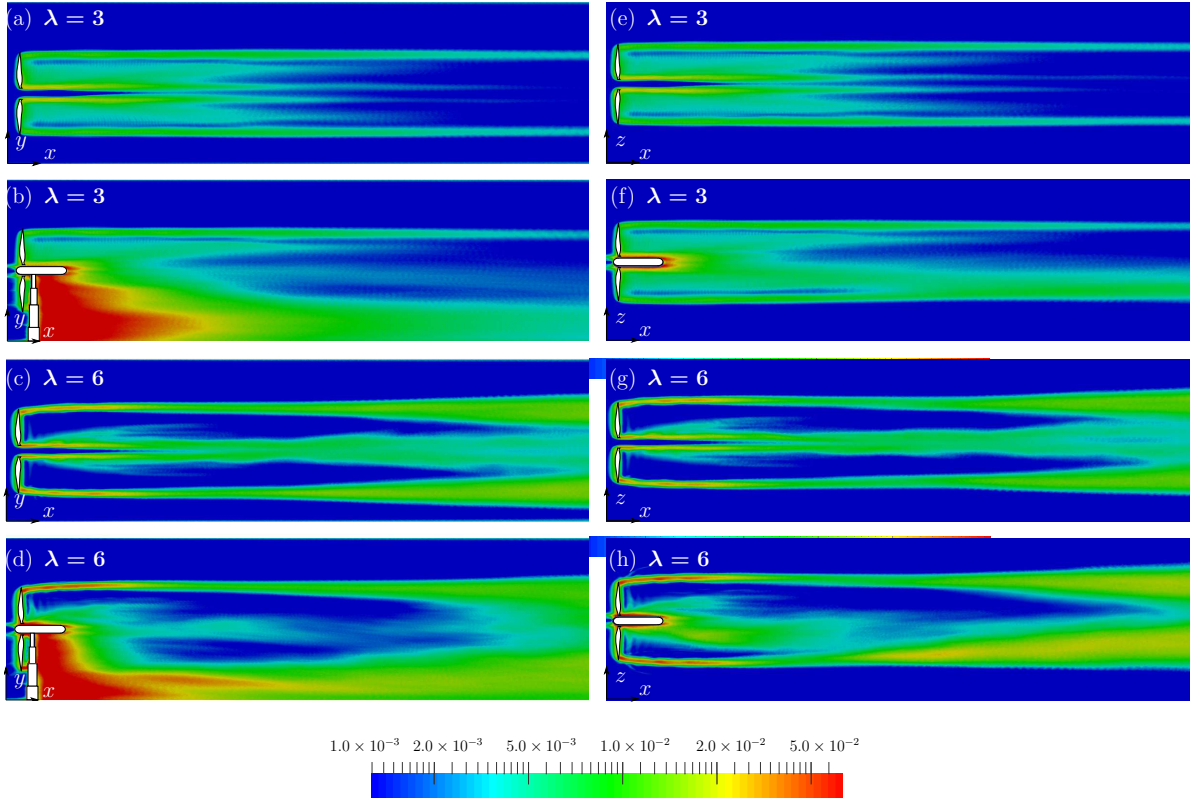


Figure 3.10. Color contours of Turbulent kinetic energy (TKE) in a x-y plane (left column) and x-z plane (right column): (a-b, e-f) $\lambda = 3$, (c-d, g-h) $\lambda = 6$ with (b,d,f,h) and without (a,c,e,g) tower and nacelle.

Figure 3.10 shows the turbulent kinetic energy (TKE) ($k' = 1/2\overline{u_i u_i}$) in a vertical and horizontal plane at the center of the rotor disk. The inlet velocity is uniform and fluctuations upwind the turbine are negligible. The turbine operating at $\lambda = 3$ presents weaker tip and root vortices but a larger turbulence kinetic energy over the entire blade because the blade is operating under stalled condition as it was also observed by Krogstad et al. [4]. The turbulent kinetic energy is axially symmetric when tower and nacelle are not included as it is observed in the two cross-sections (vertical and horizontal) in Figure 3.10 a, e, c and g.

In the near wake, the tower and nacelle produce a larger amount of turbulent kinetic energy. The vortex shed behind the tower interacts with the wake of the turbine blades enhancing turbulent kinetic energy in the lower part of the wake (Figure 3.10 b,d). The region of large

velocity fluctuations, behind the tower, appears to extend further downwind for $\lambda = 3$ than that of $\lambda = 6$. This is because the rotation of the wake, due to the azimuthal force, is higher at $\lambda = 6$, advecting the wake of the tower out of the vertical plane as it is observed in the horizontal plane, Figure 3.10 (h). Indeed, the TKE is advected toward the tip region as it was discussed in Section 3.3.2. Farther downwind within the wake, the TKE at the nacelle height decreases. In fact, the turbulent kinetic energy production ceases as shown in Figure 3.9.

In Figure 3.11 the turbulent kinetic energy is shown along the spanwise direction at hub height at the downwind distances $x = 1D$ and $3D$ behind the rotor. The turbulent kinetic energy is normalized with the undisturbed inlet velocity and a log scale is used to present the results as in Krogstad et al. [4]. As observed from the contours of turbulent kinetic energy, the simulations without tower and nacelle present four peaks, at $z'/D = \pm 0.05$ and ± 0.5 , which correspond to the tip and root vortices. The TKE at the tip is smaller than that measured in the experiments for $\lambda = 6$. In fact, in the ALM, the force (and circulation) is spread over a number of grid points. On the other hand, in the real experiment, the tip is of a smaller scale than those resolved in the simulation given the value of ϵ we used. As discussed in Section 3, a smaller ϵ should be used at the tip, but this would increase significantly the computational cost. When the tower and nacelle are not modeled, a favorable pressure gradient is induced at the center of the rotor, which weakens the turbulent kinetic energy.

Numerical results compare better with experimental measurements when tower and nacelle are modeled. The improvement is observed not only in the central part of the wake, but over the entire rotor disk. Not surprisingly, the TKE does not present a drop at $z'/D = 0$. While at $1D$ downwind the rotor, the two sets of simulations (with and without tower and nacelle) almost overlaps, larger differences are observed at $3D$ where the TKE becomes more skewed, especially at higher tip speed ratio. We speculate that this is due to the interaction of the vorticity field generated by the nacelle with the helicoidal wake of the turbine.

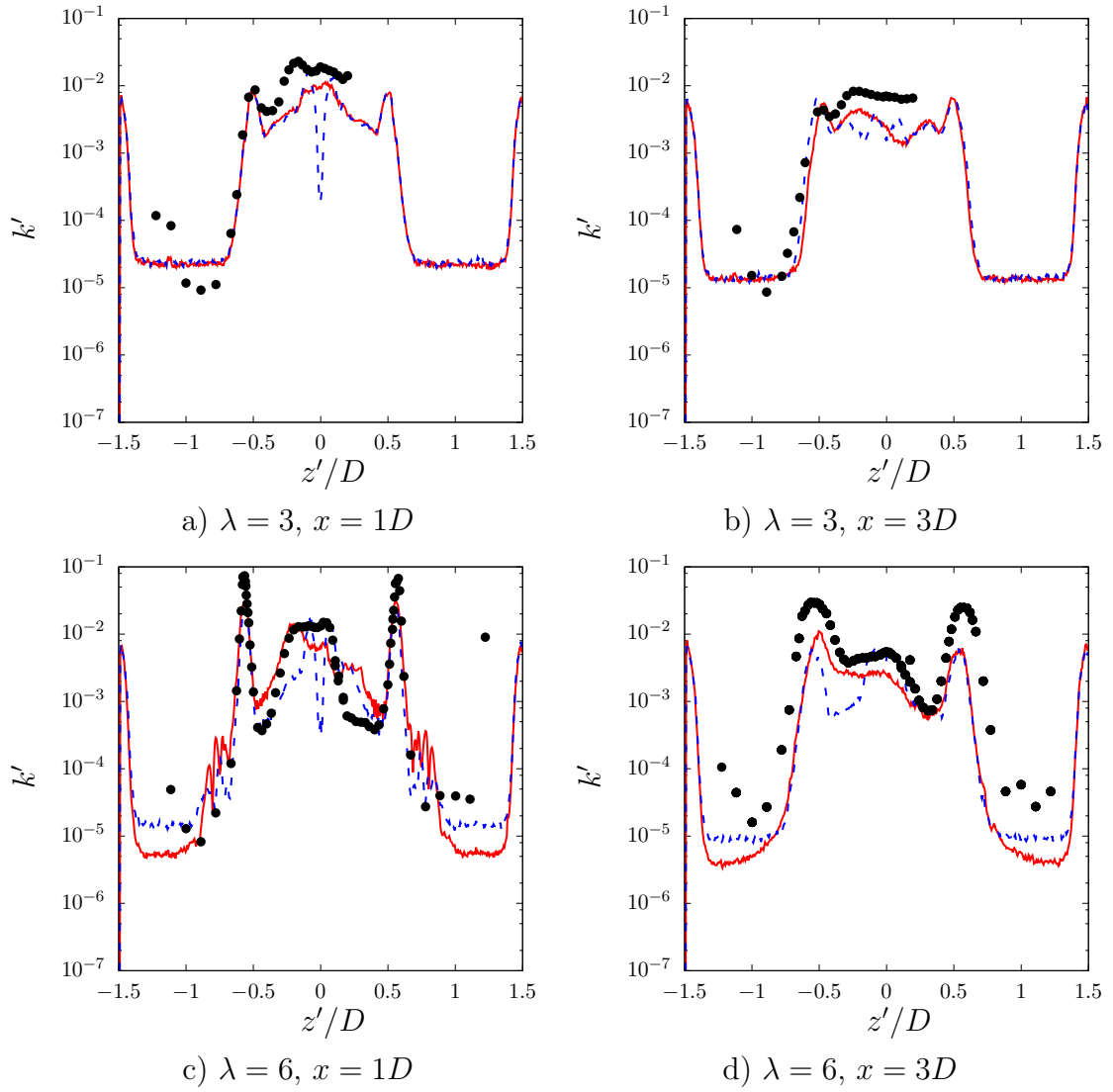


Figure 3.11. Turbulent kinetic energy profiles: present results with (—) and without (---) tower and nacelle compared to experimental measurements (\bullet). Top $\lambda = 3$, bottom $\lambda = 6$; (a,c) $1D$, (b,d) $3D$ downwind the rotor disk.

The agreement with the experiments is encouraging. The lower intensity of TKE at the center of the turbine seems to be due to the damping of the subgrid model. The Smagorinsky constant of 0.09 appears to be too large in the region of the tower and nacelle. In fact, no-model simulations (not shown here) present a better agreement in this region with the experiment.

Another approach to mimic tower and nacelle is to use a virtual force similarly to the Actuator Line. Porté-Agel et al. [34] imposed a steady drag force to mimic the tower and nacelle, while Sarlak et al. [35] an oscillating force with a frequency similar to the Strouhal frequency behind the cylinder. Both approaches prevent the formation of the jet at the hub, consistently with the present results. The oscillating force used by Sarlak et al. [35] mimics, to a good approximation, the Kármán vortex observed in Figure 9. However, it seems that the turbulent kinetic energy differs from that obtained with the immersed boundaries, in particular, because it does not reproduce the asymmetric distribution and the interaction with the tip vortices which increases entrainment. Nevertheless, the resolution required by the actuator tower and nacelle models is much lower than that needed by the Immersed Boundary Method and then it can be a good compromise between quality of results and computational cost.

3.4 Conclusion

Large Eddy simulations of a wind turbine, placed in a wind tunnel, were performed for two tip speed ratios, $\lambda = 3$ and 6, the former being an off-design condition, the latter configuration leading to the highest power coefficient. The geometrical configuration reproduces the experiment carried out at NTNU. The wind turbine was modeled using the Actuator Line Model for the rotor blades and the immersed boundary method for the tower and nacelle. A second set of simulations without tower and nacelle was performed as a reference to assess how tower and nacelle affect the wake.

The mean velocity profiles calculated numerically, with and without tower and nacelle, agree well with experimental measurements in the upper part of the rotor. However, in the lower part, a larger momentum deficit and a better agreement with the experiment is observed when the tower and nacelle are modeled. By neglecting the nacelle, a jet at the hub height

is generated. Although this has no effect on the torque or power production, it stabilizes the wake and delays the vortex breakdown. Instantaneous visualizations, as well as mean kinetic energy budget showed that the wake of tower and nacelle interacts with the tip vortices promoting the vortex breakdown and a higher turbulent kinetic energy especially in the lower part of the wake. The fluxes are not symmetric, the entrainment from the side of the swirl being larger.

In conclusion, despite tower and nacelle do not contribute much to the power production of a single isolated turbine, present results show that they influence the wake dynamics significantly. Therefore, when an array of turbines is considered, modeling tower and nacelle provides a more realistic inflow for waked turbines due to the more accurate calculation of the wake recovery and entrainment. This is very important when the performances of the entire array are considered. The asymmetry in the velocity and turbulent kinetic energy may induce fatigue loads on waked turbines that drastically differ from those which would be computed neglecting the presence of tower and nacelle.

CHAPTER 4

PERFORMANCE OF A WIND TURBINE ON A RIDGED TERRAIN

4.1 Introduction

In this chapter we consider, for the first time through high fidelity simulations, the effect of waviness on the ground on the flow past a wind turbine. Topography and roughness very often have a strong impact on the atmospheric boundary layer flow [48]. The local terrain has a direct influence on the speed and direction of the wind. Additionally, hills, ridges, mounds and other orographic features may induce velocity fluctuations that can severely affect the power production of wind turbines and increase fatigue loads. Moreover, the turbulence caused by the terrain changes the transport of kinetic energy in the wake of the turbines that is crucial on the overall efficiency of wind farms. Therefore, determining the effect of terrain induced wind fluctuations on turbines is essential for maximizing the energy production and extending their life span.

Our objective is to assess the effect of the topography on the performance of a wind turbine through Large Eddy simulations. The turbine is modeled using the actuator line model for the rotor blades, and immersed boundary method for the tower and nacelle. The topography is simplified and described as a harmonic function and modeled using the Immersed Boundary Method. A precursor simulation with periodic boundary conditions along the streamwise direction of the terrain has been performed to obtain the inflow conditions for the simulation with the turbine.

4.1.1 Literature Review

One of the earliest turbine wake model that incorporated the surface roughness is the Ainslie model [8], which is based on an eddy viscosity model. Through the turbulent viscosity

concept, the model considers the effect of the roughness as part of the ambient turbulence contribution. Incorporating the eddy viscosity model into the conservation of momentum, represents an improvement for the description of the shear stresses in the wake of the turbine for flat or moderately complex terrains. Newer top-down model approaches for describing the atmospheric boundary layer (ABL) flow through a turbine array, integrate the surface roughness of the terrain and the wind farm as shear stresses at different heights [49, 50, 51]. The simplicity of the model provides a seamless integration of the wind farm into the ABL and insightful understanding about the vertical transport of kinetic energy. Through a parametric study, Meneveau [51] demonstrated that increasing the roughness has a negative effect on the power production of a single wind turbine. Additionally, the power production of an array of turbines is almost independent of the surface roughness due to the fact that the entire wind farm acts as an augmented roughness in the ABL.

Although the wake and the top-down models help understanding the basic trends and effects of the surface roughness on the power production and vertical transport of energy, they do not provide information of the flow on highly complex terrains that are not easily parametrized as a roughness length. For example, Howard et al. [52] demonstrated experimentally that a turbine operating behind a three-dimensional hill has strong variations of the angular velocity and, consequently, of the power production due to coherent structures generated by the hill. Two-point correlation of PIV measurements of the streamwise velocity showed that large-scale structures in the ABL, were diverted by the hill and limiting their impingement into the rotor [53]. Yang et al. [54], performed a Large Eddy simulation of the flow past a wind turbine with a three-dimensional hill upwind. They demonstrated that the power production of the turbine when it is located sufficiently far from the hill is larger than that located over the flat terrain because of the speed up caused by the topography. In addition, the hill induces turbulent kinetic energy in the wake of the turbine thus promoting the wake recovery. In contrast, Reynolds-Averaged Navier-Stokes simulations (RANS) of a turbine

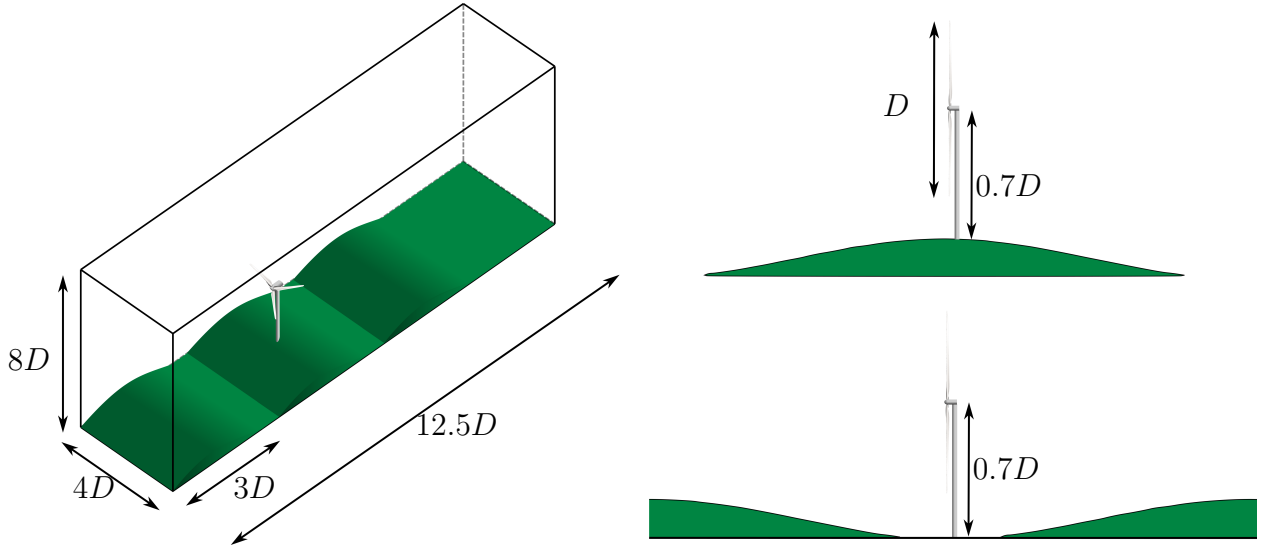


Figure 4.1. Computational box geometrical configuration.

located on the top of a large hill (0.7 the height of the hub) suggests that the wake of the turbine have a lower recovery than that on even topography [55]. An experimental study of a wind farm where the turbines are located on the leeward and downward side of the hill showed that the turbine at the top of the hill, despite working under waked condition, had less velocity fluctuations at the rotor than those experienced by the same turbine on a flat terrain located [56].

4.2 Numerical Setup

A sketch of the geometrical configuration is shown in figure 4.1. The topography is mimicked as a harmonic function:

$$y_w = a \sin 2\pi x / \lambda_W + a \quad (4.1)$$

where $2a$ is the height of the hills, λ_W is the wavelength or distance between the top of the hills and x is the streamwise coordinate. The wavelength is kept constant to $3D$, where D is the rotor diameter ($126m$). Two different amplitudes, $a/D = 0.1$ and 0.05 , are considered. To understand the effect of the relative position of the rotor within the terrain, the turbine

is placed either at the crest or at the cavity of the undulated wall. The dimension of the computational box are $12.5D \times 4.0D \times 8D$ along the streamwise, spanwise and wall-normal direction, respectively. The computational grid has $1024 \times 512 \times 512$ grid points, in streamwise, spanwise and wall-normal, respectively. The inlet velocity profiles are given by a precursor simulation with periodic boundary conditions to obtain a developed flow with the same topography as in the inflow-outflow simulation. An extra set of simulations with flat terrain and same inlet has been performed to quantify the effect of local topography.

The turbine modeled is the NREL 5-MW [57]. The tower in these simulations has been model as a cylinder with a diameter of $0.048D$. The nacelle was also modeled as a cylinder with the same diameter as the tower with a semi-circular hub in the front-end. Details of the blades can be found on the technical report [57]. The rotor angular velocity is given by

$$I\dot{\omega} = T_{aero} - M_{gen} \quad (4.2)$$

where I is the rotor angular moment of inertia ($11\,776\,047\,kg \cdot m^2$ per blade), M_{gen} and T_{aero} is the generator and aerodynamic torque, respectively. The generator torque is given by $\kappa\omega^2$, where ω is the angular velocity and κ is the generator gain.

4.3 Results and Discussion

4.3.1 Wind Turbine Wake and Recovery

The time averaged streamwise velocity and turbulent intensity profiles at various locations are shown in figure 4.2. Three different cases have been considered, with the turbine placed either on the crest, at the center of the cavity or on the flat terrain. Because the turbines rotor is in 3 different positions within the boundary layer, to compare the results, the origin in vertical direction is taken for all cases at the hub ($y/D = 0$).

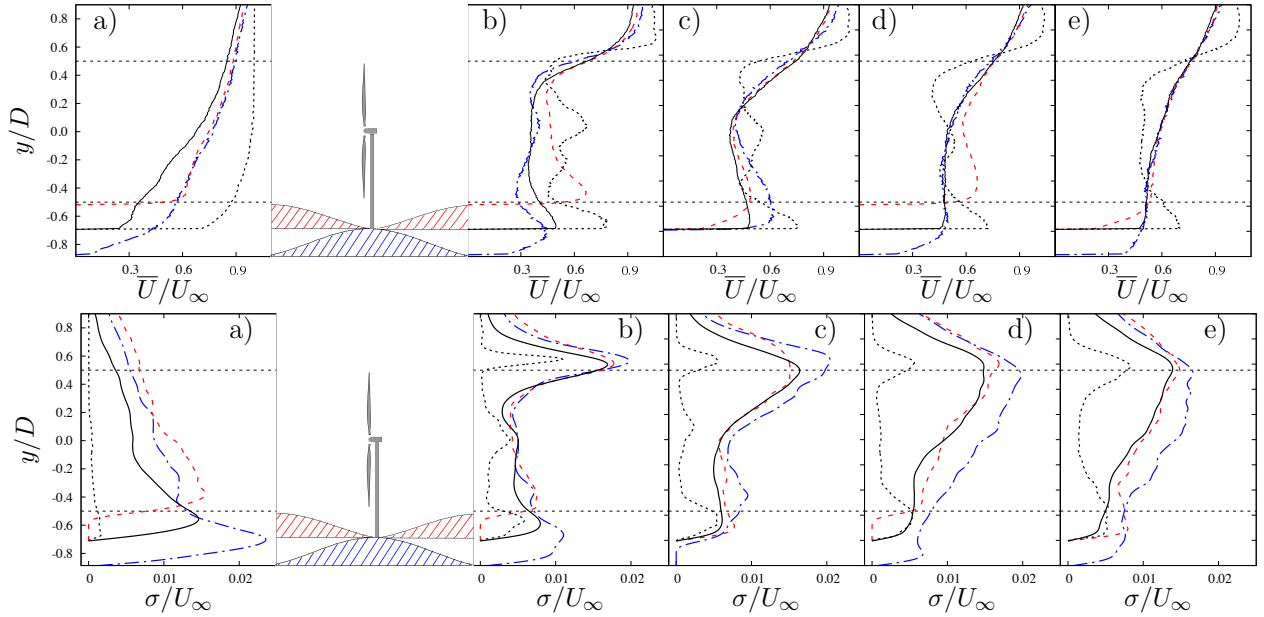


Figure 4.2. Vertical profiles of the time averaged streamwise velocity (top) and turbulent intensity (bottom) at: a) $x/D = -1.5$, b) $x/D = 1.5$, c) $x/D = 3.0$ d) $x/D = 4.5$ and e) $x/D = 6.0$ from the turbine rotor located in the flat terrain (·····), flat with wavy inlet (—), cavity (---) and crest (— · —) of the wavy wall.

The presence of the ridges upwind the wind turbine causes larger shear and turbulence intensity across the lower part of the rotor (Figure 4.2a). The incoming turbulence causes an increment of the velocity fluctuations across the wake of the wind turbine further downwind (Figure 4.2b-e). The turbines placed on the ridged terrain have a larger turbulence intensity than that located on the flat terrain. Consequently, the increased mixing leads to a faster wake recovery. Moreover, the turbine located on a flat terrain with inlet velocity from the wavy terrain precursor simulation, has a similar wake recovery to those placed on the cavity and the crest of the hills. This suggests that the structures and intensity of the incoming turbulence dominate the wake recovery and the effect of the local topography is weak.

To provide a quantitative measure of wake recovery, the time and rotor averaged streamwise velocity ($\langle U_{\text{rot}} \rangle = 1/(U_\infty A_{\text{rot}}) \int_{A_{\text{rot}}} \bar{U}_1 dA$) is shown in figure 4.3. The rotor swept area is given by A_{rot} , the vertical dashed line denotes the position of the turbine rotor and \bar{U}_1 is the time averaged streamwise velocity normalized by the rotor averaged velocity at the inlet,

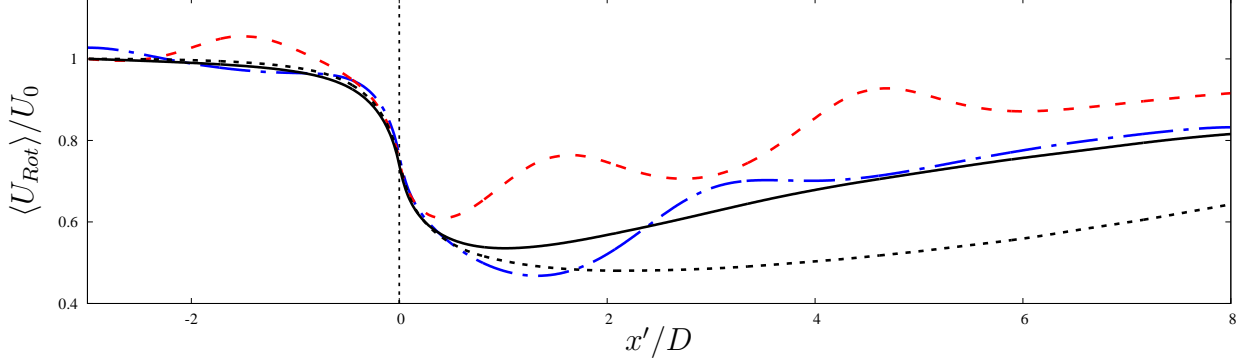


Figure 4.3. Streamwise profile of the rotor area averaged velocity U_{Rot} non-dimensionalized with the rotor averaged velocity at the entrance of the computational box for a turbine placed in a flat terrain (·····), flat with wavy inlet (——), cavity (---) and crest (—·—) of the wavy wall.

U_0 . Across the rotor, at $x/D = 0$, the adverse pressure gradient causes a momentum deficit proportional to the thrust force applied by the turbine. A slow recovery rate is observed for the turbine located over the flat terrain. At $x = 8D$ behind the turbine U_{Rot} is nearly 65% of the inlet velocity. The turbine located at the center of the cavity is affected by an adverse pressure gradient that greatly reduces the performance of the turbine. The effect of the pressure gradient is evident in the modulation of the rotor averaged velocity, especially in the wake. This is due to the alternating adverse and favorable pressure gradient on the windward and leeward sides of the hills, respectively. The wake behind the turbine located on the flat terrain and the turbine placed on the crest of the wavy wall shows similar wake recovery. This indicates that the turbulent structures at the inlet are responsible for the wake recovery more than the local topography.

To examine the mechanism that promotes the entrainment of mean kinetic energy into the wake, the mean-flow energy-transport tubes are constructed. The energy tubes are based on the transport equation of mean-flow mechanical energy,

$$E = \frac{1}{2} \overline{U_i U_i} + \frac{P}{\rho}, \quad (4.3)$$

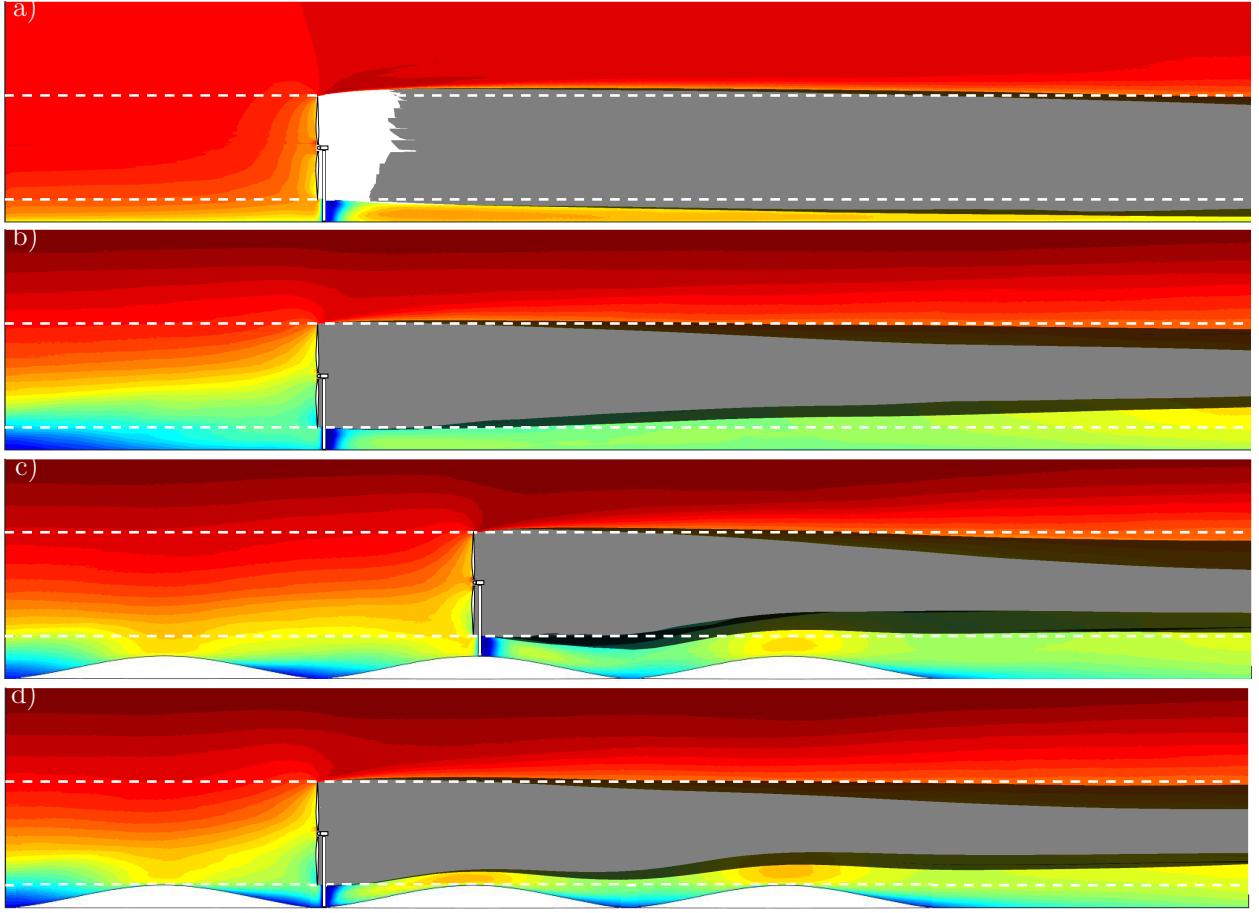


Figure 4.4. Color contours of time averaged streamwise velocity with superimposed mean kinetic energy tubes for a turbine placed in: a) a flat terrain, b) flat terrain with wavy inlet and in the c) crest and d) cavity of the wavy terrain. The black (■) and gray (■) delimits the energy tube due to mean kinetic energy convection only and the superposition of convection and flux due to turbulence, respectively.

as in Meyers and Meneveau (2012) [58]. The tubes are formed such that there is no exchange of energy through the mantle. Therefore, the mantle is formulated using the total mechanical energy transport vector field (Φ) given by

$$\bar{\Phi}_i = E\bar{U}_i + \overline{u_i u_j} \bar{U}_j - 2\nu \bar{S}_{ij} \bar{U}_j, \quad (4.4)$$

where \bar{S}_{ij} is the strain rate tensor ($S_{ij} = 1/2(\partial U_j / \partial x_i + \partial U_i / \partial x_j)$). The color contours of the time averaged streamwise velocity with superimposed the energy tube are shown in Figure 4.4. The energy tube constructed considering the convection term only ($E\bar{U}_i$) is

shown in black, and in gray the superposition of the flux due to turbulence ($\overline{u_i u_j} \overline{U_j}$) and the convection term. The contribution of the viscous diffusion term was considered but due to the nature of the flow (high Reynolds number) it has a negligible effect and therefore is not included in this analysis. Because the mantle is constructed from the rotor, the only sinks of energy would be the mean-flow viscous dissipation (although negligible) and production of turbulent kinetic energy.

The turbine located on the flat topography shows a white region near the rotor. This is caused by the strong tip vortex inducing a turbulence flux out of the wake region. Although this flux is considerably small, it causes an expansion of the convection-turbulence flux tube over the convection only tube. The convection-turbulence tube behind the turbine does not show a significant reduction in size in comparison to the convection tube. This is due to the low turbulence intensity behind the turbine as it was shown in Figure 4.2b-e. Nevertheless, the small recovery of the rotor averaged velocity observed (Figure 4.3) is due to a small flux of energy from the sides of the wake due to the interaction between the wake of the tower and that of the rotating wake of the rotor as it was observed in Santoni et al. (2017) [30].

The mean kinetic energy entrainment into the turbine wake is mostly driven by the flux due to turbulence. This causes a larger contraction of the convection-turbulence flux tube (gray) (Figure 4.4) over that of mean kinetic energy convection (black). The topography in the leeward side of the turbine modulates the convection of mean kinetic energy, producing an expansion and contraction of the energy tube, following the surface of the topography. Despite this modulation, the ridges do not contribute significantly to the total energy entrainment. The turbine in the flat terrain with the same inlet velocity as those placed in the ridges shows a similar reduction of the convection-turbulence flux tube. This suggests that the turbulence structures generated farther upwind are responsible of most of the mean kinetic energy entrainment, rather than the ridges on the wake. Recall that we are looking

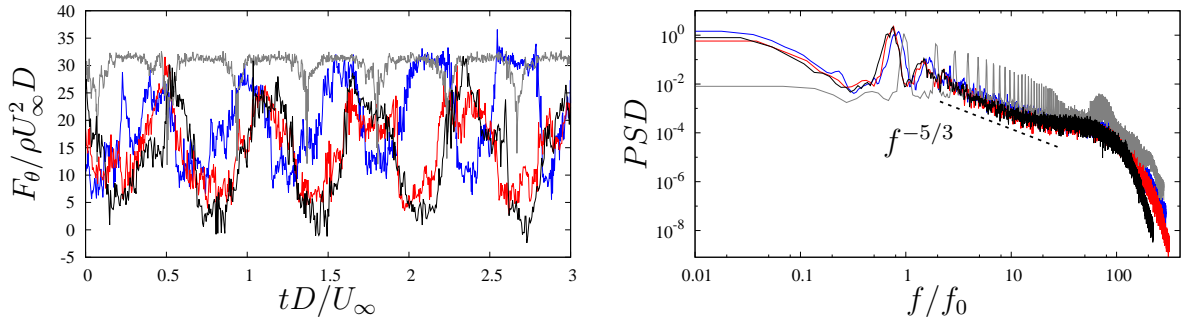


Figure 4.5. Tangential aerodynamic load at 75% of the blade span (left) and power spectra of the fluctuations of the load (right) for the turbine located flat terrain (—), flat terrain with wavy inlet (—), cavity (—) and crest (—) of the wavy wall

at the **mean** kinetic energy transport, for which the production of turbulent kinetic energy is a sink (while it is a source in the **turbulent** kinetic energy balance).

4.3.2 Power Fluctuations

The tangential aerodynamic force at 3/4 of the span of the blade as a function of time and the corresponding power spectral density are shown in Figure 4.5. A periodic fluctuation on the tangential force which corresponds to the angular rotation frequency $f/f_0 = 1$ is observed for each case. The turbine located over the flat terrain shows a constant force through its revolution with a small fluctuation due to the tower shadowing effect. This effect is not observed as clearly for the turbines in the ridged terrain due to the shear in the upwind velocity, but it produces a smoother reduction in the tangential force at the same frequency. Large coherent structures, impinging the rotor of the turbines on the ridged terrain, are observed, especially, on the low frequency region showing a larger power spectral density than that on the flat topography.

The power production as function of time is shown in Figure 4.6 for the 3 cases with inlet velocity obtained with the precursor simulation with a wavy terrain. The case with a turbine on a flat terrain and laminar inflow is also shown as reference. The time history of the power

Table 4.1. Power coefficient and rms for each case.

	a/λ_W	P_n	\overline{C}_P	C_{Prms}/\overline{C}_P
crest	0.016	0.303	0.481	0.158
cavity	0.016	0.264	0.468	0.164
crest	0.033	0.283	0.507	0.217
cavity	0.033	0.204	0.460	0.244
Flat	-	0.455	0.495	0.036
Flat	0.033*	0.177	0.504	0.241
Flat	0.016*	0.257	0.507	0.169

* Simulations on a flat terrain with same inlet of the ridged terrain.

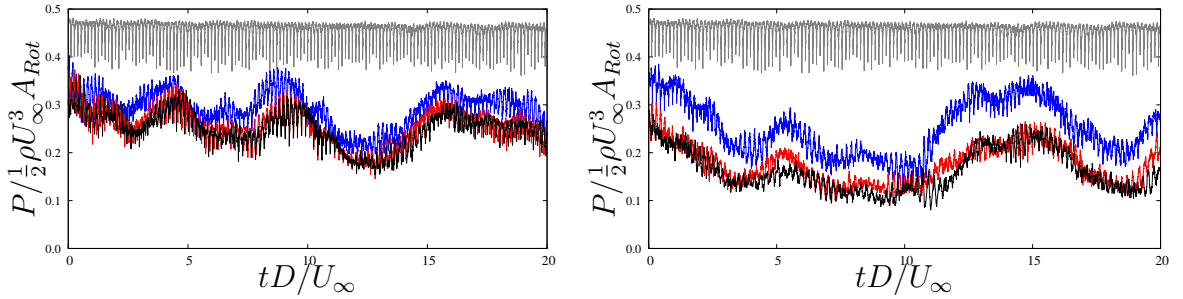


Figure 4.6. Time series of the normalized power for the turbine located flat terrain (—), flat terrain with wavy inlet (—), cavity (—) and crest (—) of the wavy wall with slope $a/\lambda_W = 0.0167$ (left) and $a/\lambda_W = 0.0333$ (right).

production is very similar for the turbines on the crest, center of the cavity and flat terrain when the inlet is the same (precursor simulation with wavy walls). In fact, the power fluctuations, shown in Table 4.1, are mostly dependent on the amplitude of the wavy terrain rather than on the location of the turbine. The location of the turbine influences mainly the average power production. The turbine located at the crest of the hill is in an advantageous location over the turbine located at the cavity, therefore having a larger power output.

4.4 Conclusion

Large Eddy simulations of a turbine on a ridged terrain were performed. The wind turbine was modeled using the actuator line model and the tower, nacelle and topography were resolved with the Immersed Boundary method. The ridges were modeled as a harmonic

function with a constant distance between the hills ($\lambda = 3D$) for two different amplitudes $a/D = 0.05$ and $a/D = 0.10$ to evaluate the effect of the hills height. The turbine was placed in the cavity or in the crest of the hill to assess the performance of the wind turbine relative to its position.

Results show that the wake recovery and power production of the turbine is largely determined by the upwind topography. The wavy wall showed to be unfavorable to the average power production of the turbine compared to the turbine in the flat terrain, as it increases the shear reducing the available energy at the turbine rotor. Fluctuations on the power production were shown to be correlated to the amplitude of the upwind topography, rather than if the turbine was placed on the crest, cavity or in the flat terrain. In addition, the wake recovery of the turbine was caused by the mean kinetic energy flux due to the velocity fluctuations induced by the coherent structures impinging into the rotor. The local topography showed to have a smaller effect on the recovery as the turbine located in the flat terrain with high turbulent intensity at the inlet showed to have a similar recovery to those placed on the ridges.

CHAPTER 5

NUMERICAL SIMULATION OF AN ONSHORE WIND FARM ¹

5.1 Introduction

In the present chapter we discuss an alternative approach for wind farm modeling. The computational box is made of 5 nested domains resolving the mesoscale wind variations over the entire north Texas Panhandle region and the wind fluctuations and turbine wakes at the farm level. We propose an alternative method to model an array of turbines by implementing the parameterization of Fitch et al. [16] into a coarse LES. To evaluate the performance of the wind turbine parameterization against a high fidelity turbine model, an additional offline nesting is performed with our in-house LES code (UTD-WF) [20] (6th nested domain). The turbines in UTD-WF are modeled using the rotating actuator disk [29]. The comparison with meteorological, SCADA and LiDAR measurements has been discussed in Santoni et al. [59].

5.1.1 Literature Review

Wind farms have been modeled into the planetary boundary layer (PBL) as a momentum deficit into numerical weather prediction (NWP) models [16, 17]. The sink of momentum depends on the power curve of the turbine, which is a function of the incoming wind. Additionally, the fraction of kinetic energy extracted from the flow that is not converted into electrical power is added as a source of turbulent kinetic energy production to the PBL model. The PBL model accounts for the exchange of momentum, heat and moisture between the earth surface and the troposphere that is filtered by the grid and is restricted to

¹ Portions Adapted from Santoni, C., E. García-Cartagena, U. Ciri, G. Iungo, and S. Leonardi (2018). Coupling of mesoscale weather research and forecasting model to a high fidelity large eddy simulation. Journal of Physics: Conference Series 1037 (6), 062010.

resolutions of the order of 1 – 100 km [60]. This approach allows examining the interaction between the atmospheric boundary layer and a wind farm in a diurnal cycle. For example, numerical results obtained by Fitch et al.[18] indicated that the wake is nearly 4 times larger during the night, under stable atmospheric conditions, than during the day for a wind farm in central Iowa. Using a similar wind farm parameterization, Lee et al.[19] studied the wind farm wake during the evening transition from unstable to stable atmospheric boundary layer (ABL). During the transition, the wakes of the upwind turbines intensify reducing the power production of the downwind turbines in the evening. These results have been recently corroborated by LiDAR measurements on the wake of the wind turbines, [61, 62]. A drawback of this numerical approach is that multiple turbines may be located on the same computational cell precluding the study of wake interactions.

In fact, finer resolution is necessary to resolve and understand entrainment of mean kinetic energy [20, 63], wake interaction, and its effect on the atmospheric boundary layer. Abkar et al. [64] studied the performance of a wind farm in a diurnal cycle using large eddy simulations (LES) and the actuator disk with rotation. A precursor simulation of a flat topography with radiative heat flux was performed to change the atmospheric conditions from stable to unstable in the diurnal cycle. They concluded that the turbulence intensities in all three directions have to be considered to obtain an accurate prediction of the impact of the atmospheric stability on the wind turbine wakes. To represent more accurately the turbine wake interaction with the atmospheric boundary layer, Mirocha et al. [65, 66] incorporated the generalized actuator disk into the Weather Research and Forecasting (WRF) model. They found good agreement on the near wake of a single turbine when the resolution on the rotor is adequate. Alternatively, Vollmer et al. [67] performed simulations of a region in central Iowa with WRF to provide a mesoscale forcing to a large eddy simulation of a single turbine with an actuator disk model (ADM). In order to properly represent the actuator disk, the required resolution was between 5-10 m for the smaller nested domain solved with

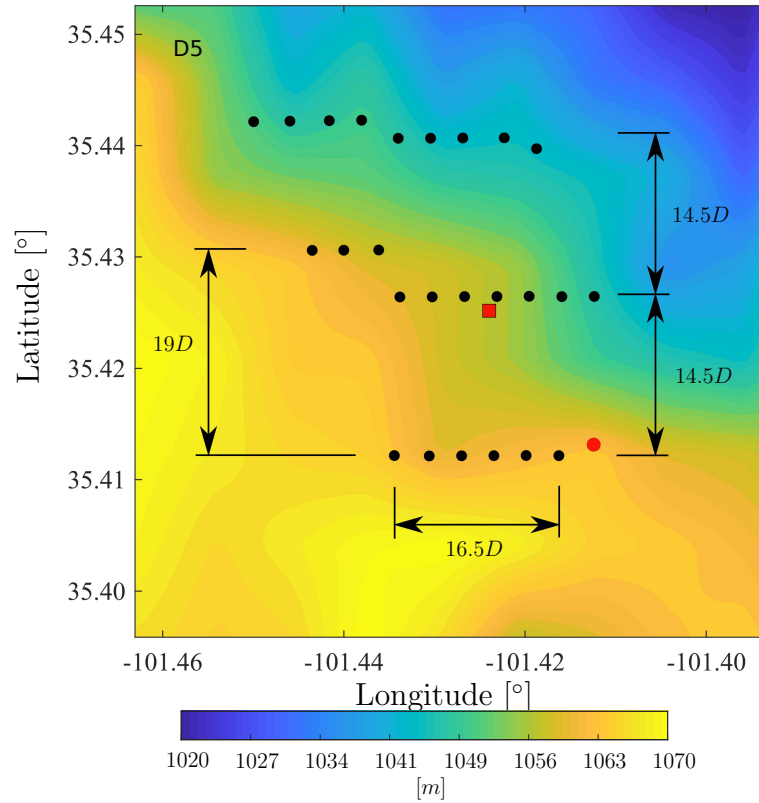


Figure 5.1. Wind farm layout superimposed over the color contours of the topographic elevation. The location of the met-tower is marked by the red circle (●) and the LiDAR by the red square (■). The position of each turbine is marked by a solid circle (●).

LES. The computational requirements for such resolutions might limit the size of the region studied and, consequently, the amount of turbines.

5.2 Methodology

5.2.1 Wind Farm layout

We simulated the flow past a wind farm located in the Panhandle region in north Texas, which consists of 80 turbines. The computational domain of the innermost domain resolved with WRF includes only the 25 turbines shown in Figure 5.1 to reproduce the experimental campaign of El-Asha et al. [62]. The turbines are of the same manufacturer and model with

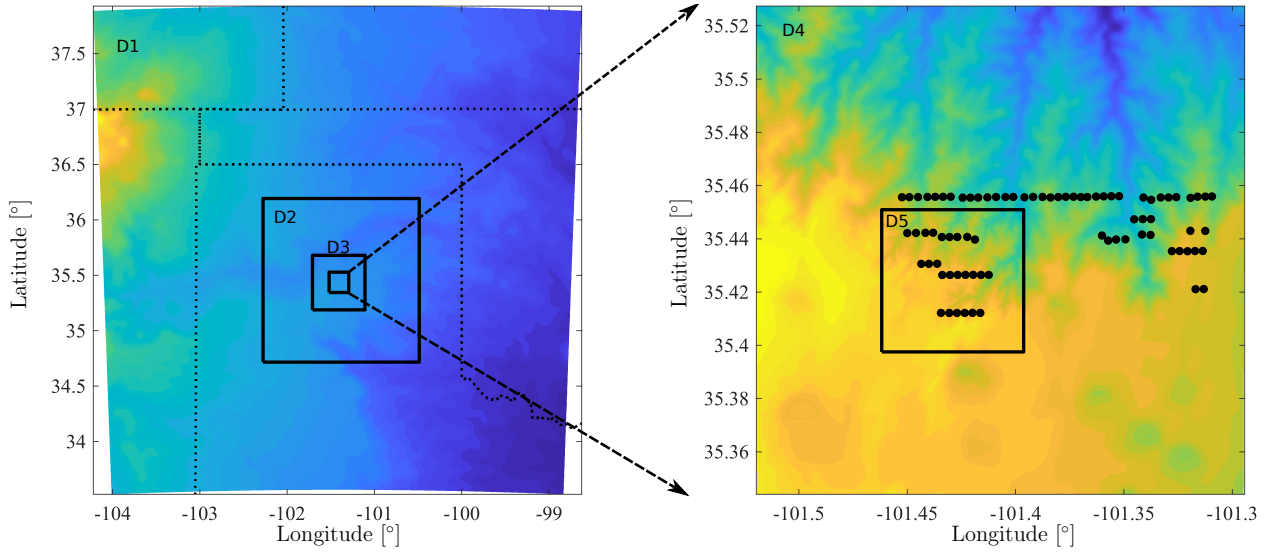


Figure 5.2. Color contours of the topographic elevation of the Texas Panhandle region. The state boundaries are delimited by the dotted lines (·····) and the domains by the solid lines (——). The position of each turbine is marked by a solid circle (●).

a nominal power production of 2.3 MW, each, at 11 ms^{-1} , a rotor diameter, D , of 108 m and a hub height of 80 m. The spacing between the rows, along the meridional direction, is approximately of $14.5D$ and $3.3D$ along the zonal direction.

5.2.2 Numerical Scheme and Flow Configuration

Numerical simulation of 5 nested domains progressively smaller and more resolved have been performed with the Weather Research and Forecasting (WRF) model, developed by the National Center of Atmospheric Research (NCAR). The numerical integration in time is performed using a third-order Runge-Kutta scheme. The spatial discretization consists of a staggered fifth and third-order central difference upwind biased advection scheme for the horizontal and vertical direction, respectively. The larger domain has a size of $512 \text{ km} \times 512 \text{ km}$ with a resolution of 4 km of the Texas Panhandle region, Figure 5.2. The initial and boundary conditions of the first domain are obtained from the North America Mesoscale

Forecast system (NAM) model that is run by the National Centers for Environmental Prediction (NCEP) with a space resolution of 12 km and a time resolution of 3 hours. The grid resolution is increased by a factor of 3 for the subsequent domains up to a resolution of 49 m for the smaller domain. Details of the size and horizontal resolution of the domains can be found in table 5.1. The wall-normal direction is discretized with 100 grid cells on all the domains. The grid points are stretched to cluster more points near the surface and in the rotor region where the resolution is between 7 and 12 m. A resolution of 12 m near the surface produces better agreement with the observed wind speed, wind direction and power production according to Lee et al. [68].

The mesoscale atmospheric modeling is used for a computational grid cell larger than 1 km. Therefore, for domains $D1$ and $D2$, the vertical mixing is modelled using the Mellor-Yamada, Nakanishi and Niino (MYNN) planetary boundary layer scheme [69, 70]. For subsequent domains ($D3 - D5$), the turbulence mixing model is replaced by fully three-dimensional local sub-grid turbulence (LES) scheme. The sub-grid stresses are computed using an eddy viscosity model that is dependent on the turbulent kinetic energy. Therefore, turbulent kinetic energy 1.5 order of closure is used, where a prognostic equation is solved to obtain the TKE for the computation of the turbulent viscosity.

In addition, an off-line coupling to our LES in-house code, described in detail in Chapter 2, is performed for a subset of 6 turbines of the wind farm for the first diurnal cycle (Figure

Table 5.1. WRF domains size and resolution

Domain	Size	Resolution
$D1$	512 km \times 512 km	4 km
$D2$	173 km \times 173 km	1.3 km
$D3$	58 km \times 58 km	444 m
$D4$	21 km \times 21 km	148 m
$D5$	6 km \times 6 km	49 m
UTD-WF	4 km \times 756 m	4 \times 6 m

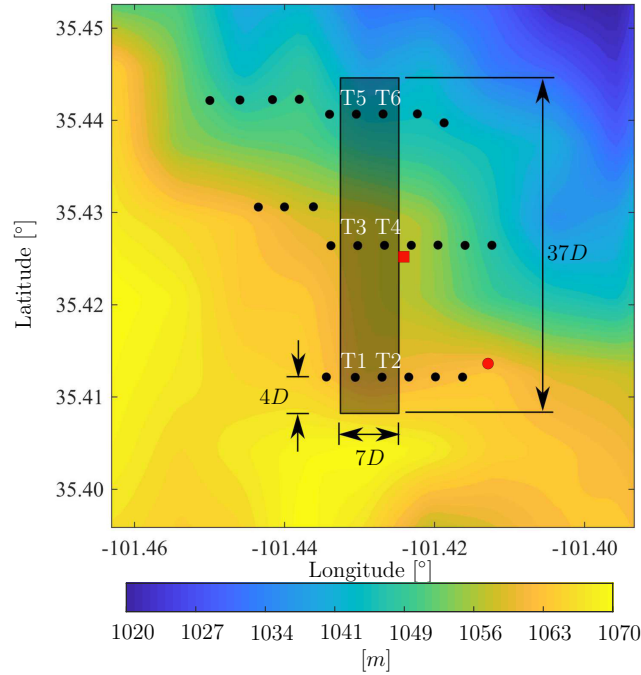


Figure 5.3. High fidelity Large Eddy simulation domain, delimited by the solid lines (—). The turbines location are indicated by the black circles (●). The location of the meteorological tower is denoted by the red circle (●) and the LiDAR by the red square (■).

5.3). With regards to the turbine model, instead of the ALM, which requires a very fine resolution, for this case we used a rotating ADM. The generator torque, blade pitch angle and yaw orientation are computed from an adapted version of the baseline controller in Laks et al.[71]. The angular velocity of the turbine is determined by the rotor dynamics by balancing the aerodynamic and generator torque. The tower and nacelle of the turbines are modelled using the immersed boundary method that has been widely validated [23, 30].

The WRF and UTD-WF simulations were performed in our in-house cluster using a total of 128 and 64 Intel Xeon (Sandy Bridge) cores, respectively. Best performance was found from hybrid distributed and shared memory parallel capabilities of the WRF code. In addition to the 6 days of simulation discussed in this chapter (2015/09/05 through 2015/09/10), a spin-up of 7 days is carried out allowing sufficient time for the development of the flow in the interior of the domain. The largest domain $D1$ has a time step of 10 s and subsequent

domains ($D2 - D5$) have a reduction ratio of 3. The ratio of the wall-clock time to simulation integration time is approximately 3 for WRF and 6.6 for our in-house code (the grid has about twice the grid points and finer time integration than WRF). We recall that the simulations are not in sync, the coupling is one-way and therefore, the computational time of one domain is not affected by the other domains.

Turbine Modeling in WRF

The turbines in WRF are modeled as a momentum sink (drag) and turbulent kinetic energy source as in Fitch et al. [16]. Therefore, the drag generated by the turbine in a grid cell is given by

$$F_{T,i} = \frac{1}{2} N_t \frac{C_T (U_j U_j)^{1/2} U_i A}{\delta z}, \quad (5.1)$$

where C_T is the turbine thrust coefficient, A is the rotor swept area, U_i is the velocity at the grid cell along the i -direction, δz is the vertical distance between grid points and N_T is the number of turbine per horizontal area of the grid cell.

The turbulent kinetic energy (TKE) produced by the turbines is given by

$$\Pi = \frac{1}{2} N_t \frac{(C_T - C_P) (U_j U_j)^{3/2} A}{\delta z}, \quad (5.2)$$

where C_P is the turbine power coefficient. Therefore, the kinetic energy that is extracted from the flow that is not converted into electrical power is transformed into TKE. This model was initially developed to be applied in a mesoscale model, where the production of turbulent kinetic energy of the turbines was added by Fitch et al.[16] in the MYNN planetary boundary layer scheme. Because the PBL is not parameterized through the MYNN scheme, in the domains $D3$ through $D5$, the turbulence production is considered in the computation of the eddy viscosity given by,

$$\nu_{h,v} = C_k l_{h,v} \sqrt{e}, \quad (5.3)$$

where subscripts h and v stand for horizontal and vertical direction, respectively, C_k is constant ($C_k = 0.18$), l is the mixing length and e is the TKE. A prognostic equation is solved for the evolution in time of the TKE given by

$$\frac{\partial e}{\partial t} + \frac{\partial U_i e}{\partial x_i} = (P_s + \Pi + B - D), \quad (5.4)$$

where P_s and Π are the TKE production due to shear and the wind turbines, respectively, B due to buoyancy and D is the dissipation. Details of the computation of the shear, buoyancy and dissipation terms can be found in the WRF description manual [72].

To understand the effect of the turbulence production on the turbine parameterization, two sets of simulations are performed. The first set of simulations accounts only for the momentum deficit given by equation 5.1, hereafter this model will be referred to as MO. The second set of simulations considers the momentum deficit and the turbulence production, Eq. 5.1 and 5.2, hereafter MDTKE.

5.3 Validation against Met-Tower data

The numerical results are compared against meteorological data, temperature, wind speed and direction at a height of 80 m from a met-tower located in the east side of the southernmost turbine row were collected as 10 minutes average and standard deviation. Met tower wind speed, direction and turbulence intensity acquired during the 6 days period are shown in Figure 5.4. The night-time period, indicated in the figure by the shaded region, is characterized by high wind speed and low turbulence intensities, distinctive of stable atmospheric conditions. In the transition between night and day, the turbulence production increases due to the buoyancy, thus enhancing the turbulence intensity. Consequently, the wind speed is reduced. The opposite effect is observed during the evening transition. The wind direction is very stable. During night-time the wind is mostly from the south and south-west

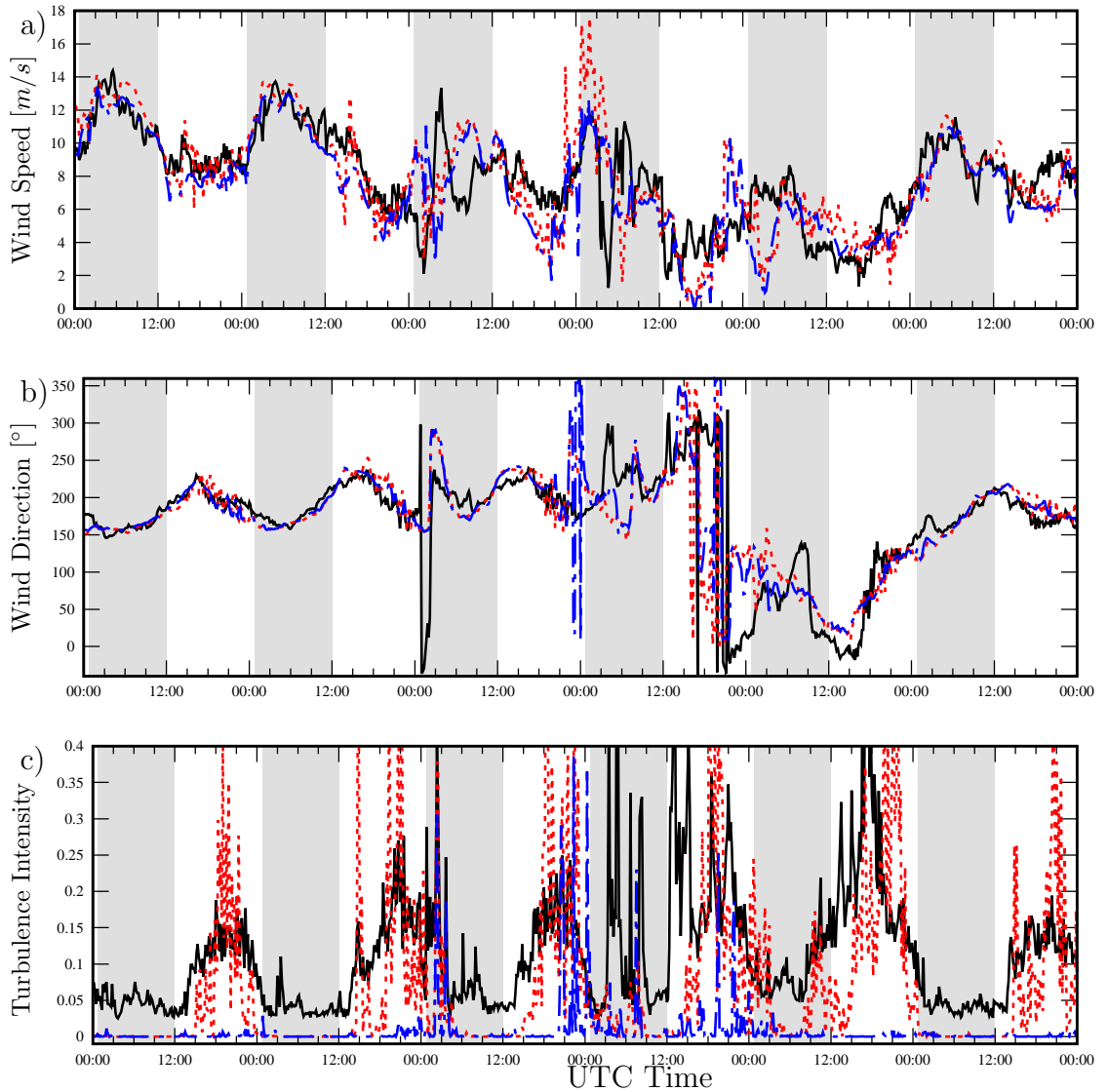


Figure 5.4. Time variation of the wind speed (a), wind direction (b) and turbulence intensity (c) at 80 m height for 2015/09/05 through 2015/09/10; (---) WRF simulation $D2$, (---) WRF simulation $D5$ and (—) met tower measurements. Shaded gray region delimits the night-time period.

and during the day-time from south-east and north-west. The wind speed and direction, obtained in the domains $D2$ and $D5$, agree well with the anemometer measurements. The high frequency variations in the wind speed and wind direction are not well captured by domain $D2$ due to the space filtering caused by the coarse grid resolution. The turbulence

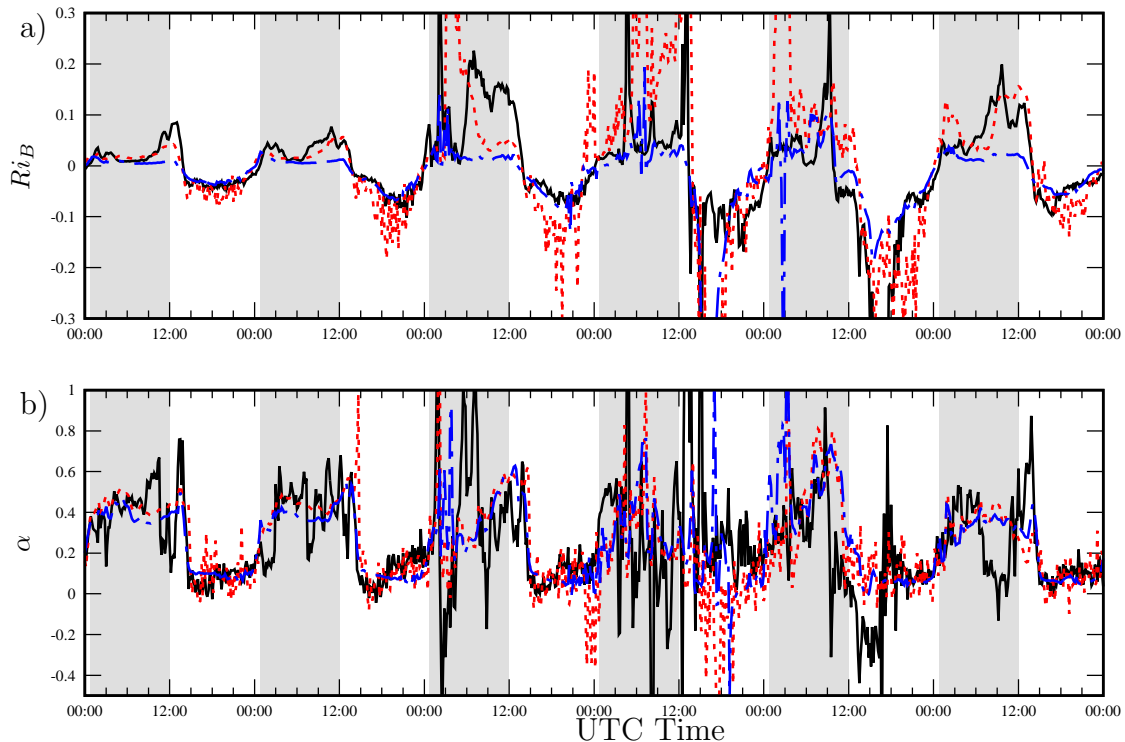


Figure 5.5. Time variation of the bulk Richardson number (a) and shear exponent (b) at 80 m height for 2015/09/05 through 2015/09/10; (— —) WRF simulation $D2$, (· · · ·) WRF simulation $D5$ and (—) met tower measurements. Shaded gray region delimits the night-time period.

intensity is almost constantly zero, even during convective atmospheric condition. Domain $D5$ approximate better than $D2$ the wind speed fluctuations, although during night-time the turbulence intensity is underestimated.

The atmospheric boundary layer stability has been quantified using the bulk Richardson number (Figure 5.5a), that is given by

$$Ri_B = \frac{g\Delta\bar{\theta}_v\Delta z}{\bar{\theta}_v(\Delta\bar{U}^2 + \Delta\bar{V}^2)}, \quad (5.5)$$

where g is the gravity acceleration, θ_v is the virtual potential temperature, z is the height of the measurement, U and V are the horizontal velocity components and Δ stands for the difference between the measurements taken at two different heights, 36 m and 80 m. During

the day-time, $Ri_B < 0$, the incident solar radiation increases the temperature of the air near the ground, producing buoyancy that is characteristic of convective atmospheric condition. During the night-time the opposite effect is observed, $Ri_B > 0$, with a smaller turbulence intensity as observed in Figure 5.4. The vertical wind shear exponent, α , computed as

$$U_H(z) = U_R \left(\frac{z}{z_R} \right)^\alpha, \quad (5.6)$$

(where U_H is the mean horizontal wind speed, U_R is the mean horizontal wind speed at a reference height z_R) can also be used to quantify the stability of the atmosphere [73]. Values of $\alpha > 0.3$ characterize stable atmospheric conditions. During convective conditions, the buoyancy driven turbulence increases the mixing lowering the shear exponent to $\alpha < 0.2$. The numerical simulations, of both domains $D2$ and $D5$, capture with good agreement the measured atmospheric stability and the wind velocity profile (Figure 5.5b).

5.3.1 Velocity Spectra

To verify that each nested domain properly resolves the turbulent scales, we evaluate the turbulent kinetic energy spectra (Figure 5.6). The energy spectra, $E(f)$, is defined as

$$E(f) = \int \frac{1}{\pi} R(s) e^{-ifs} ds, \quad (5.7)$$

where f is the frequency. The autocovariance, $R(s)$, of the velocity is given by

$$R(s) = \overline{u(t)u(t+s)}, \quad (5.8)$$

where the over-bar stand for the time averaged of the product of the wind speed, u , at time t and $t + s$. The frequency is non-dimensionalized with respect to the diurnal frequency, f_o . The low-frequency spectra, exhibit an inverse power law behavior, $E(f) \sim f^{-1}$. This observation agrees with the experimental observations of Perry et al. [74] and Katul et al. [75]. In this region, a small peak at $f/f_o = 1$ is observed, which correspond to the diurnal

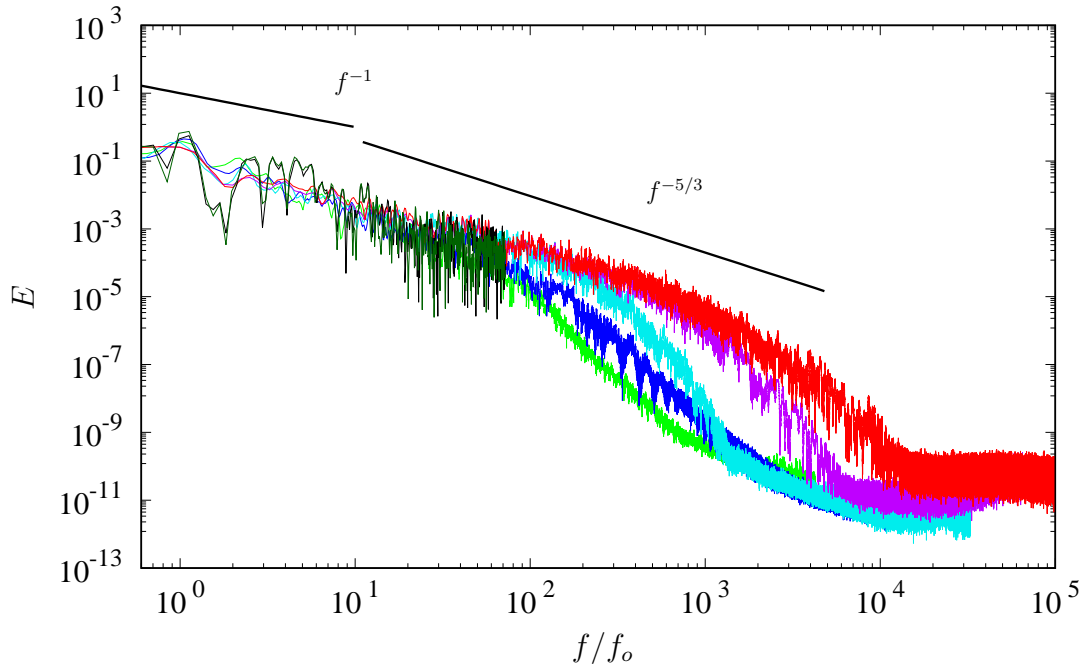


Figure 5.6. Spectra of the wind speed at 80 m high of domain; (---) $D1$, (---) $D2$, (.....) $D3$, (-.-.-) $D4$, (-.-.-) $D5$, (—) met-tower measurements and (—) SCADA from a turbine located in the southernmost row. The solid lines represent an energy decay with slope -1 and $-5/3$.

cycle. For mid-range frequency ($f > 10^{-1}$), the energy spectra decay with a slope of $-5/3$ as suggested by Kolmogorov [76]. As the resolution is progressively increased from parent to child grids, the small scales are better approximated. The domain $D1$ and $D2$ result over dissipative at intermediate scales. This behavior is corrected by the nested domains. This lends justification to the nesting, which allows a close approximation of the large scales and at the same time, with a reasonable computational cost, accurate small scales in the innermost domains. The energy spectra from the met-tower and SCADA measurements is also computed and included as reference. Small frequencies corresponding to large scale turbulence agree well with numerical results. However, at larger frequencies the SCADA and met-tower measurements are cut off because they are averaged over 10 minutes. Despite this drawback, the numerical results agree well to the measurements. A small under prediction in the energy content is observed from domain $D1$ and $D2$ with respect to the $D3 - D5$ and

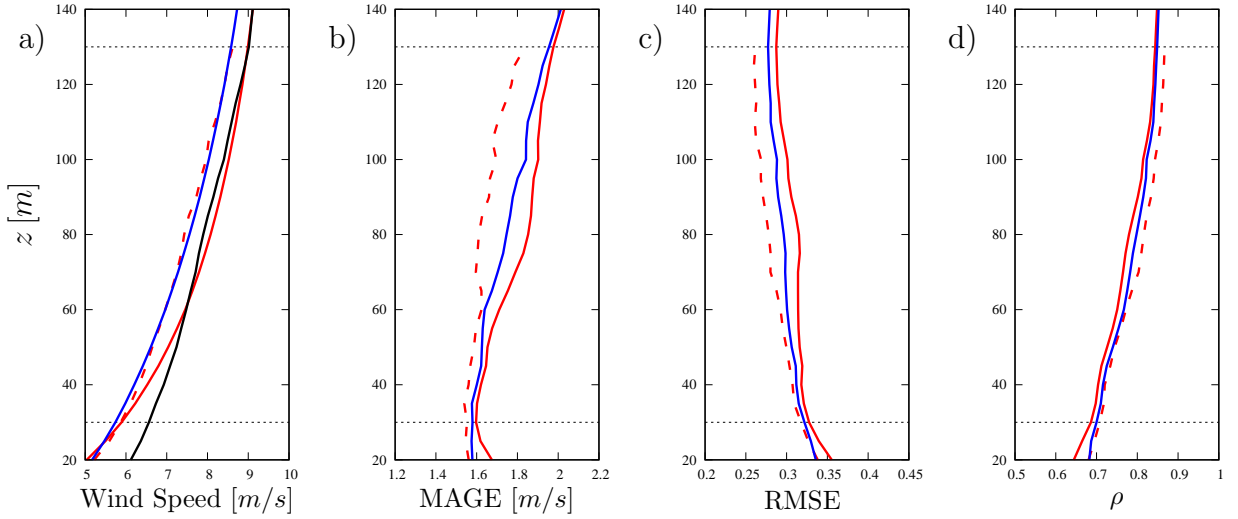


Figure 5.7. Numerical simulation velocity profile comparison against (—) LiDAR wind speed measurements; (a) mean wind speed profile, (b) mean absolute gross error, (c) root mean square error and (d) index of agreement of the (—) numerical results at $D2$, (—) numerical results at $D5$ and (---) numerical VAD at $D5$. Horizontal dashed lines (-----) delimits the turbines rotor area.

the measurements. This suggest that the PBL model scheme may be resolving part of the vertical mixing, causing an over dissipation.

5.4 Validation Against LiDAR

Although the hub velocity can be used to obtain a good estimate of the power production of the turbines, the velocity profile across the rotor can provide a better approximation of the thrust force. Therefore, the velocity in the lower region of the atmospheric boundary layer was compared against LiDAR measurements. Details of the measurement techniques (which is not part of this thesis) can be found in El-Asha et al. [62]. Three consecutive plan position indicator (PPI) scans at elevation of angles of 1° , 3° and 5° , at an angular velocity of $4^\circ s^{-1}$ were performed. The vertical profiles of the horizontal velocity and wind direction were obtained by applying the velocity-azimuth display (VAD) technique to each PPI scan. Numerical results are plotted in two different ways. One is the standard velocity profile

along the wall normal direction. The other is an attempt to mimic the LiDAR with the numerical results. To mimic the LiDAR measurements, the velocity field of the numerical results is decomposed into a radial velocity projected on a conical surface with a constant elevation angle and vertex at the LiDAR position as in the VAD technique. For brevity we will refer to this analysis as the “numerical VAD”. Due to the low resolution of domain $D2$ this computation was only performed for $D5$.

Comparison of the time averaged wind speed between the measurements and numerical simulations is shown in Figure 5.7a. Although, the numerical results on domain $D5$ slightly over estimate the shear in the lower rotor region, they agree well with the field measurements especially in the higher parts of the rotor. The numerical VAD and velocity profile on domain $D2$ slightly under predict the wind speed in comparison to the LiDAR measurements. In fact, both profiles collapse on top of each other, which suggests that the VAD technique produces an average over space obtaining similar velocity profile as those in $D2$.

To quantify the agreement between the numerical simulations and the measurements in time, the mean absolute gross error (MAGE) has been computed:

$$MAGE = \frac{1}{N} \sum_{i=1}^N |V_N - V_M|, \quad (5.9)$$

where V_N is the wind speed obtained from the numerical simulation and V_M is the LiDAR measured value. Figure 5.7b shows that the error across the rotor varies from 1.6 in the lower part of the rotor to 2 m s^{-1} in the top. Moreover, a deviation of around 30% is observed on the normalized root-mean-square error (RMSE) across the rotor region (Figure 5.7c). Although the mean velocity profile at domain $D5$ approximates better the average velocity profile, it does have a slightly larger RMSE and MAGE than the domain $D2$ and numerical VAD. This is due to the resolution of the experimental measurement, which is closer to the scales of $D2$ rather than to the dynamics solved in $D5$. However, the discrepancy in the error between the different measurements is considerably small.

The Willmott's index of agreement [77] is used to evaluate the relative co-variability of the numerical and experimental wind speed with respect to the mean of the experimental measurements. The index of agreement is given by

$$\rho = 1 - \frac{\sum (V_N - V_M)^2}{\sum [|V_N - \bar{V}_M| + |V_M - \bar{V}_M|]^2}, \quad (5.10)$$

where \bar{V}_M stands for the time averaged wind speed obtained from the LiDAR, V_N wind speed from the numerical simulation and V_M is the measured wind speed. The numerical results from domain *D2* and *D5*, and also the numerical VAD method shows a very similar agreement to the measurements in the rotor region. Because of the overestimated shear in the lower half of the rotor an agreement of 70% is obtained. The numerical simulation velocity profile accuracy increases up to 85% in the upper region of the rotor.

Figure 5.8 shows the absolute value of the radial velocity component aligned with the LiDAR beam for stable and unstable atmospheric conditions. Results are compared with those obtained with the MDTKE simulation; the radial velocity is reconstructed from the Cartesian components and projected into a conical surface with an elevation angle of 3° to mimic the LiDAR. When the wind direction is perpendicular to the line of sight, the measured radial velocity is shown as a zero radial velocity streak. During the convective atmospheric condition (Figure 5.8 a and b), this zero radial velocity region has a sigmoid shape due to the change in the wind direction with height, also known as the Ekman spiral. The wakes of the turbines located in the front row are convected toward northwest while those in the last row are directed northward. This difference in the wake direction is due to the difference in height of the radial velocity projection over the conical surface behind the wind turbines. Also, it is observed how the wake of the turbines of the first row impinges the turbines on the second row and those of the second row on the third, successively.

During unstable atmospheric conditions (Figure 5.8 c and d), the wind speed decreases and the variability in speed and direction increases. Contrary to the stable conditions, the am-

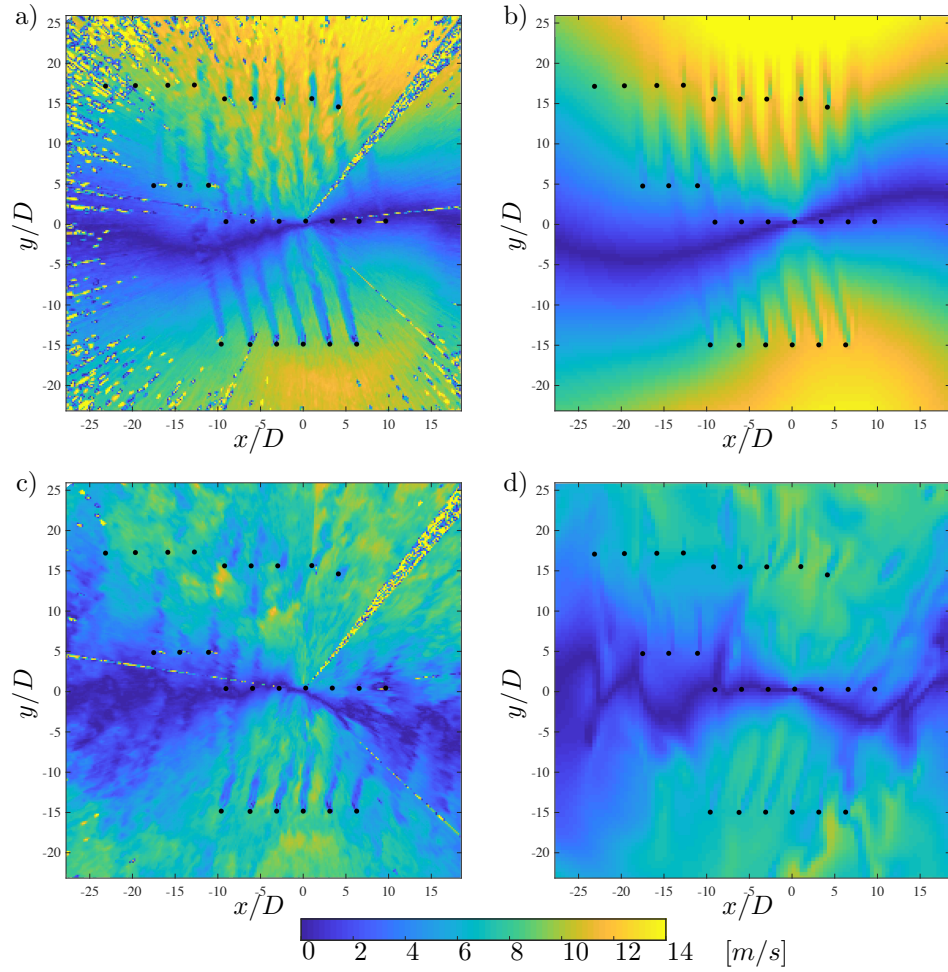


Figure 5.8. Color contours of the absolute value of the radial velocity field obtain from the LiDAR measurements (a, c) and virtual LiDAR from the MDTKE numerical simulations (b, d) during stable (a, b) and unstable (c, d) atmospheric boundary conditions at an elevation angle of 3° , synchronized in time. The turbine position are denoted by a solid circle (\bullet).

bient turbulent kinetic energy increases the energy entrainment and, therefore, the recovery of the wake of the wind turbines. It is evident that wake interaction is more significant during the stable atmospheric conditions as it was observed by El-Asha et al. [62]. The momentum deficit is slightly underestimated by the numerical simulations in comparison to the measurements, especially in the near wake region for both stable and unstable conditions.

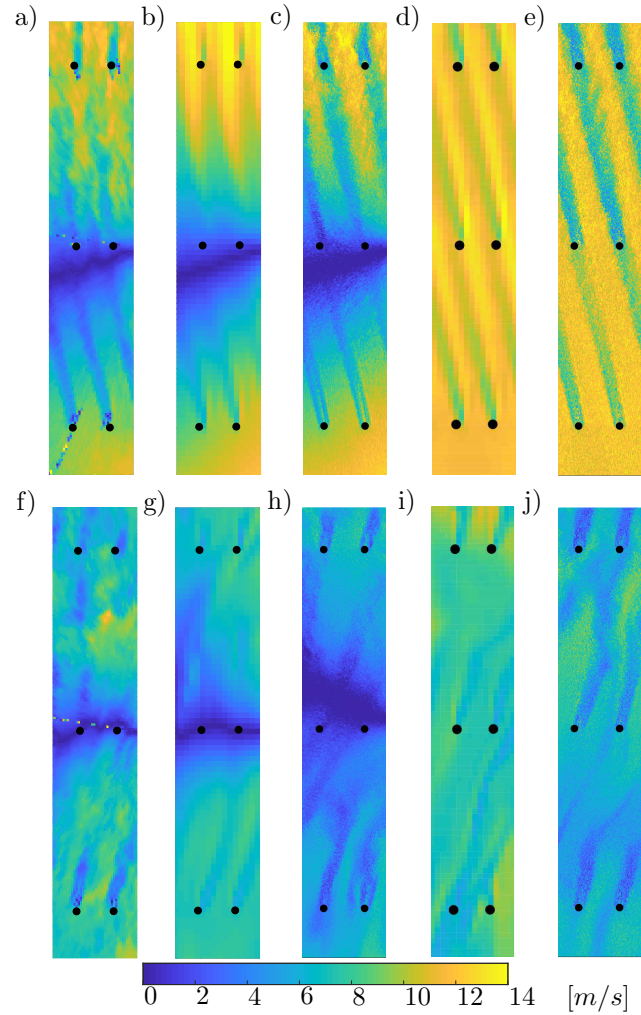


Figure 5.9. Color contours of the absolute value of the radial velocity field obtained from the LiDAR measurements (a,f), WRF (b,g) and UTD-WF LES (c,h) during stable (a-e) and unstable (f-j) atmospheric conditions at an elevation angle of 3° . The velocity magnitude obtained from WRF MDTKE (d,i) and UTD-WF (e,j) on a plane at hub-height is also shown as reference. The turbine positions are denoted by a black circle (\bullet).

Nevertheless, the direction of the wakes and interaction between the wind turbines is well captured by the numerical results.

A comparison between the LiDAR measurements, WRF and UTD-WF numerical results is shown in Figure 5.9. In addition to the radial velocity in figure 5.9 a,b,c, the wind field obtained with WRF and UTD-WF on a plane at hub-height is also shown for reference

(Figure 5.9 d-e,i-j). The wind speed is similar to the radial velocity counterpart, with the exception of the region where the velocity is perpendicular to the LiDAR line-of-sight. Wake interaction between the turbine is observed as the wake of the turbines on the first row impinges on the rotor of the turbine in the central row during stable atmospheric condition (Figure 5.9a-c). The periodic conditions on the lateral boundaries of the high fidelity LES approximate to a good degree the wake of the adjacent columns of turbines within the wind farm. The direction of the wake of WRF, UTD-WF and LiDAR agree well. The momentum deficit in the turbine wake obtained with the high fidelity LES is closer to the LiDAR measurements than that obtained with WRF domain $D5$ resolution. In fact, the wake obtained with WRF, during stable condition, expands more than the LiDAR measurements and the numerical results obtained with our in-house high resolution LES code.

Due to the mixing and entrainment of mean kinetic energy, during convective atmospheric conditions (Figure 5.9 f-h) the wake is shorter than during stable condition. Despite UTD-WF does not solve the heat flux, the velocity profile and fluctuations imposed at the inlet from the WRF solution of domain $D5$ allow a close representation of the flow with respect to LiDAR measurements.

5.5 Power Production

Figure 5.10 shows a polar histogram of the wind direction complemented with color histogram of the power production normalized with the nominal power (P_N) for each turbine within the wind farm for stable and unstable conditions for the MDTKE simulation. It is observed that for stable conditions during the six days, the wind direction is consistently from southeast. The first two rows of turbines produced between 95% and 100% of the nominal power more frequently for this direction. The power production above 95% of a turbine in the immediate wake of an upwind turbine (labeled as T14 for example) decreases due to the reduction of

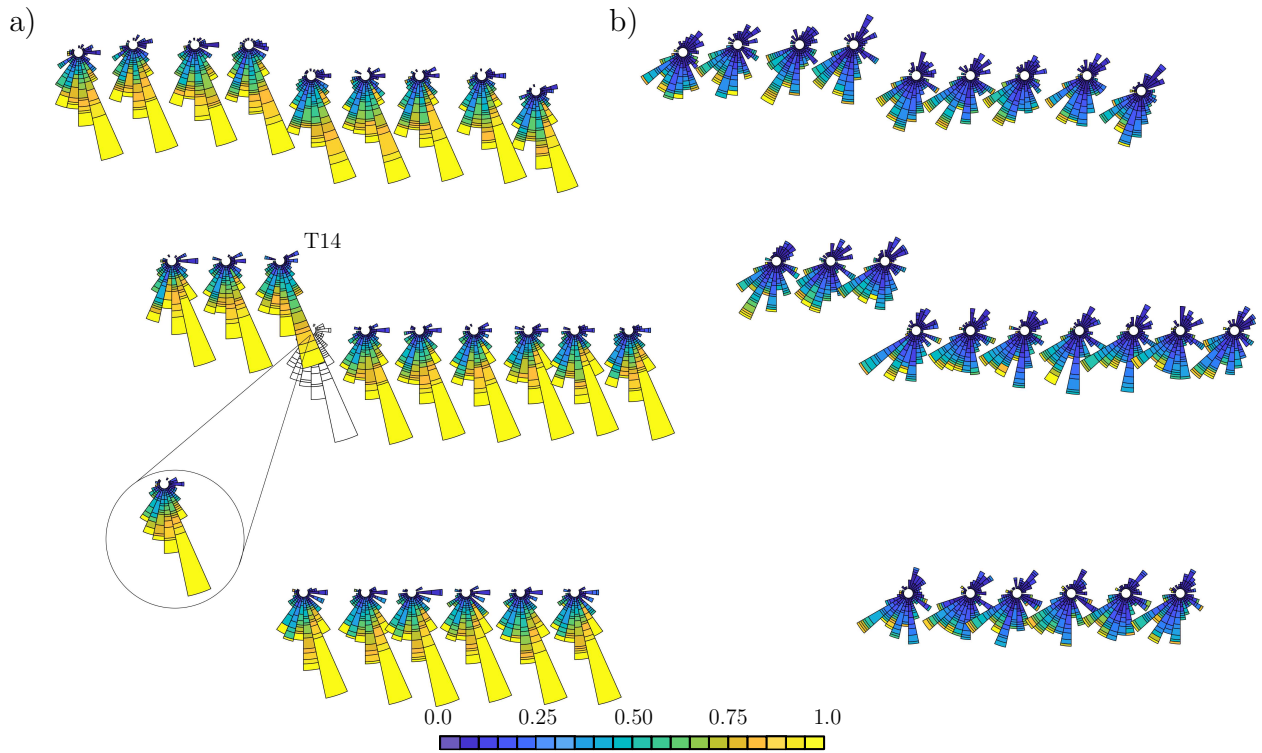


Figure 5.10. Polar and color histogram of the wind direction and power (P/P_T), respectively, during (a) stable and (b)unstable conditions. The colorbar correspond to the histogram bins with increments of 5% of the nominal power production.

energy in the wake. Similarly, the effect on the wake interaction is observed between the third row of turbines. Despite the reduction of power production due to wake interaction its evident that during stable atmospheric conditions, all the turbines are able to produce at least 95% of the turbine nominal power. This means that there are occasions during the stable convective period in which the wind directions is such that wake of the windward turbines is convected in the lateral gap between two turbines located downwind, not impinging into their rotor.

During unstable atmospheric conditions, the wind speed decreases and the wind flow variability in speed and direction increases significantly (Figure 5.4). Because the wind velocity during stable condition is above the manufacturer rated speed, all the turbines operate in region 3, reaching nominal power production during the night-time. As the wind velocity

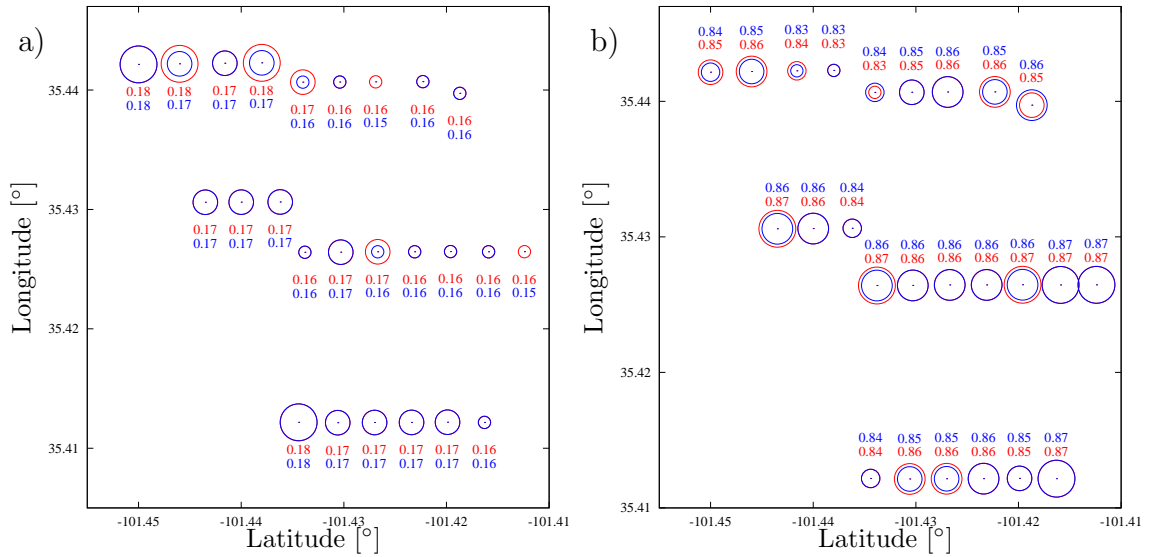


Figure 5.11. Mean absolute gross error (a) and index of agreement (b) of each turbine within the wind farm; (\circ) MDTKE turbines and (\circ) MO turbines. Size of each circle is relative to the value shown for each turbine.

decreases and the buoyancy generated turbulence dominates, the power production of the turbines decreases to about 50% and, consequently, the fluctuations of power production increase. This is further corroborated in the polar histogram (Figure 5.10b), where the wind direction probability is spread from the south to the southwest and from the north-east. Concurrently with the reduction in the wind speed and increase in variability the power production, histogram shows a larger probability producing between 40% and 60% of its nominal power. Despite the ambient turbulence due to the unstable atmospheric conditions increases the wake recovery, it also decreases the wind speed at hub height that is detrimental for the power production. Similar analysis performed on the MO turbines simulation, not shown here, does not produce an appreciable difference with respect to the MDTKE turbines.

To assess the performance of the wind farm simulations in WRF, the power production of each turbine was compared against the SCADA data of the corresponding turbine. Both turbine models, the MDTKE and MO, show a mean absolute gross error between 15% and

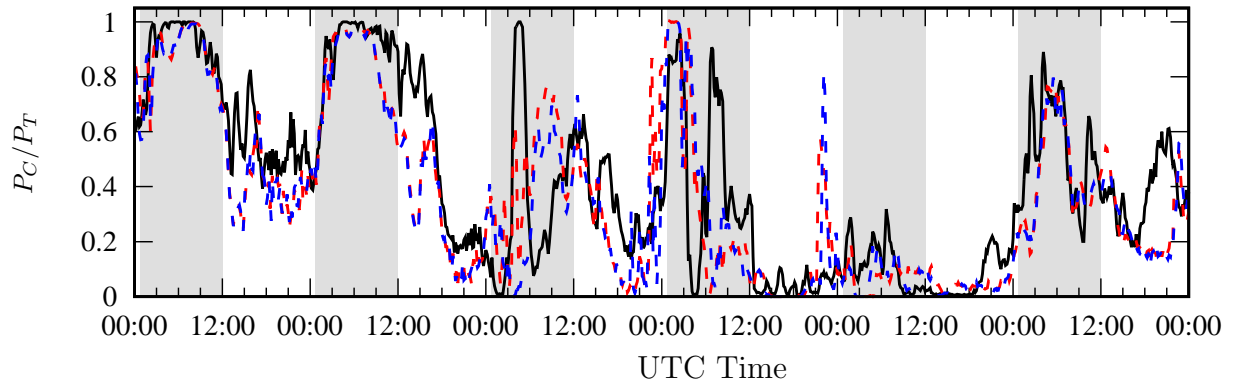


Figure 5.12. Wind farm normalized net power production for the 2015/09/05 through 2015/09/10; (—) SCADA data, (---) MDTKE turbines and (---) MO turbines. Shaded gray region delimits the nigh-time period.

18% of the power production (Figure 5.11a). The models do not show a significant difference in their performance. In fact, the performance of these models show to be independent of the turbine position or if the turbine is operating in the wake of a windward turbine.

The Willmott's index of agreement (see equation 5.10) was also computed for each individual turbine in order to analyze the co-variability of the numerical simulations with respect to the SCADA data (Figure 5.11b). An agreement between 83% and 88% is observed with respect to the SCADA data. The MDTKE turbine model presents only a marginal improvement, about 1%, with respect to the MO model. This suggests that the production of turbulence kinetic energy by the turbines does not have a significant impact on the power production of the turbines operating under waked conditions. In this wind farm, the distance between two rows of turbines is about $14D$, therefore, a minor change in the entrainment of mean kinetic energy may not be relevant.

The performance of the entire wind farm was assessed by summing the total power production (P_C) and normalizing it by the total power capacity (P_T) of the 25 wind turbines (Figure 5.12). The six days time series shows that most of the power production occurs during the nigh-time, which corresponds to the stable condition period. During the day-time the

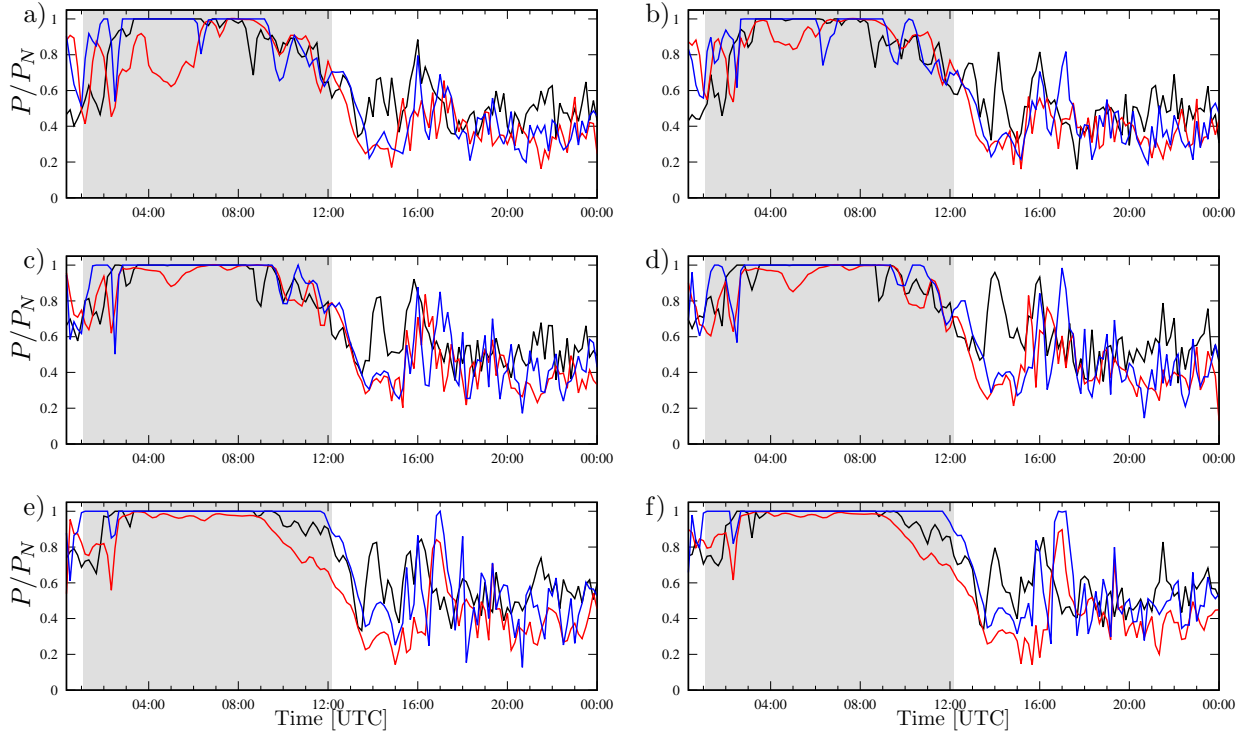


Figure 5.13. Power production of the northern-most row (a,b), middle row (c,d) and southern-most row (e,f); (—) SCADA measurements, (—) WRF simulation and (—) high-fidelity LES. The night-time is delimited by the shaded region.

power production decreases considerably and the variability increases. Both turbine models, MDTKE and MO, agree very well with the SCADA, especially during the stable condition periods. The largest difference between the numerical simulation and the SCADA is observed during the transition between stable to convective atmospheric regime. Since the transitions occurs during a relatively short period of time, the index of agreement is still encouraging, with 87.4% and 87.1% for the MDTKE and MO model, respectively. The small difference in the power production between the MDTKE and MO suggests that for this particular turbine separation, the added turbulent kinetic energy by the turbine may not contribute significantly to the wake recovery and, consequently, on the power production of the waked turbines.

The power production obtained with our in-house LES code is also compared against the SCADA system (Figure 5.13) and those obtained from the MDTKE simulation, for a single diurnal cycle. A noticeable difference is observed on turbines T1 and T2 in the southern-most row (see Figure 5.3), during the morning transition (Figure 5.13e,f). The velocity profiles upwind of turbine T1 obtained by UTD-WF and WRF are very similar as shown in Figure 5.14a. Small fluctuations in the velocity profile obtained with UTD-WF are due to the higher resolution of the computational grid that is capable of capturing fluctuations at a smaller scale than WRF. The momentum deficit at the location of the rotor is similar in WRF and UTD-WF (Figure 5.14b). Further downwind, $0.5D$ from the turbine rotor (Figure 5.14c), the ADM causes a larger momentum deficit than that of WRF. This difference in the momentum deficit could not be observed at the rotor because the force of the rotating actuator disk is spread over four grid points along the streamwise direction to avoid discontinuities in the discretization of the Navier-Stoke equation [29]. On the other hand, the turbine model implemented in WRF is designed for numerical grids with very low resolution. It computes the power production of each turbine using the manufacturer power curve and the velocity at hub height at the location of the turbine. Due to the induction zone and coarse grid resolution, the reference velocity used in the model may be slightly smaller than the upwind wind speed. As a consequence the power production estimated with the model and the momentum deficit are under-predicted. In addition, using only the velocity at hub-height may also under-estimate the power production especially if the velocity profile presents a high shear across the rotor of the turbine. This is not the case with the actuator disk model. For the rotating actuator disk, the power is computed from the integral of the aerodynamic forces in each blade section. Therefore, it accounts for the heterogeneity of wind speed (and the angle of attack) due to the higher shear.

Despite this difference in the computation of the power production, both the WRF simulation and the high fidelity LES have good agreement with the SCADA data. The power production

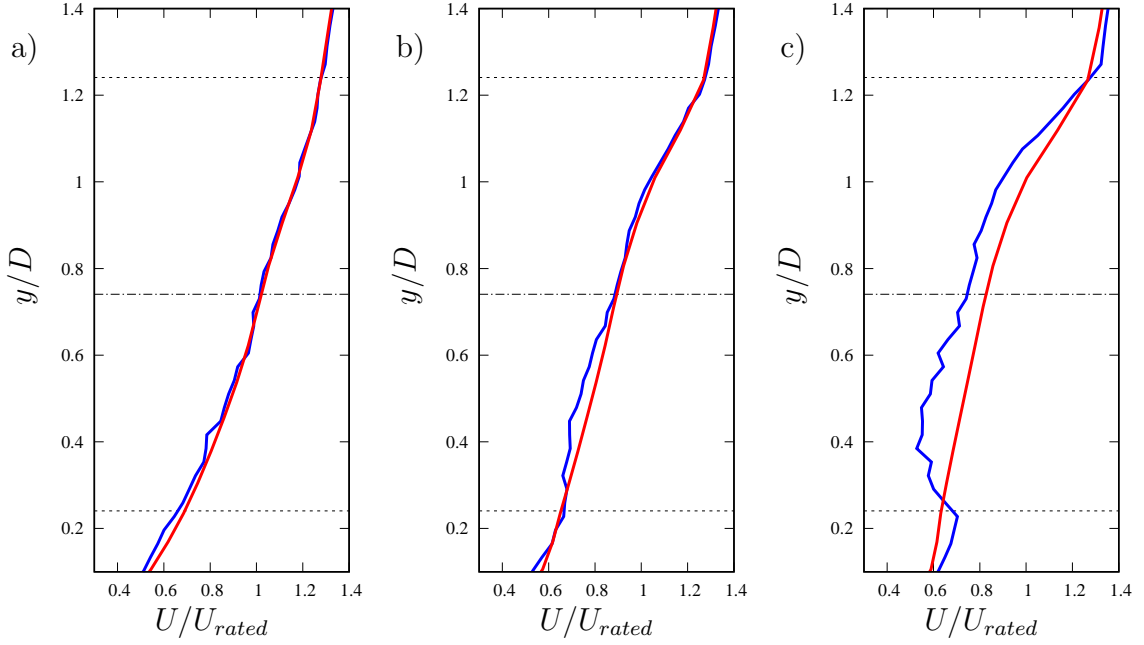


Figure 5.14. Velocity profile at 10:30 UTC averaged along $1D$ in the spanwise direction; a) $2D$ upwind, b) at the rotor and c) $0.5D$ downwind of turbine $T1$ of the WRF simulation (—) and high-fidelity LES (—) The rotor region is delimited by (·····) and the hub-height is indicated with (- - -).

Table 5.2. Turbine power production mean absolute gross error and index of agreement

Turbine	MAGE		ρ	
	WRF	UTD-WF	WRF	UTD-WF
T1	0.15	0.11	0.83	0.87
T2	0.13	0.11	0.85	0.88
T3	0.12	0.11	0.88	0.88
T4	0.13	0.13	0.84	0.84
T5	0.16	0.12	0.80	0.88
T6	0.13	0.12	0.88	0.90

of each turbine, computed by WRF and UTD-WF, presents a mean absolute gross error of about 14% and 12%, respectively (Table 5.2). Similarly, both models show a very good index of agreement with results from UTD-WF having a small improvement in the predicted power.

5.6 Conclusion

Numerical simulations of the flow in a wind farm in the north Texas region have been performed by combining 5 nested domains in WRF with our in-house LES code (UTD-WF). Turbines in WRF are modeled as a momentum deficit and a source of turbulent kinetic energy as in Fitch et al. [16, 18], while a Rotating Actuator Disk is used in UTD-WF. The wind speed and wind direction of the innermost WRF domain are used to provide time and space resolved boundary conditions to our in-house LES code. Wind speed, direction, power production, bulk Richardson number and the wind speed shear exponent obtained in the innermost domain of WRF (with 50 m resolution) agree well with met-tower, LiDAR and SCADA measurements.

Simulations performed with our in-house LES code improve slightly the results because of a finer grid (4×6 m resolution) and a more detailed turbine model, the RADM, which accounts for the variability of the wind speed in the rotor when the shear is high. The index of agreement obtained with WRF and UTD-WF is 85% and 88%, respectively.

Despite the simulation wall-clock time is around 3 and 6 times the numerical integration time, present results are promising. By increasing the number of processors and optimizing the parallelization, LES may be used in the near future as a valuable tool for the design and analysis of wind farms.

CHAPTER 6

FINAL REMARKS

The effect of the tower and nacelle on the flow past a wind turbine was studied using Large Eddy simulations. The geometrical configuration simulates the wind tunnel experiment performed at NTNU. The turbine was modeled using the Actuator Line Model for the rotor blades for two tip speed ratios, $\lambda = 3$ and 6, the former being an off-design condition. The Immersed Boundary Method was used to resolve the tower and nacelle. Numerical results of the wind turbine were compared against simulations of the wind turbine performed without the tower and nacelle. Time averaged velocity profiles along the vertical and horizontal direction showed that neglecting the tower and nacelle produces an unrealistic jet at the center of the rotor. However, modeling the tower and nacelle does not allow for the production of this jet having a better agreement with the experimental measurements. Although, it has no effect on the torque and power production of an isolated turbine, the turbulence induced by these components in combination with the swirl due to the rotor, causes a non-symmetrical flux of mean kinetic energy due to turbulence. Therefore, increasing the wake recovery on one side of the wake. This is important when the performance of an entire wind farm is considered. The asymmetry in the velocity and turbulent kinetic energy may induce fatigue loads on waked turbines that drastically differ from those which would be computed neglecting the presence of tower and nacelle. Considering the tower and nacelle improves significantly the numerical results, momentum deficit and turbulent kinetic energy, in the near and far wake having a better agreement with the experimental measurements.

The second main outcome of this dissertation was in clarifying the effect of topography on the flow past a wind turbine. Results show that the performance of the wind turbine is affected by the topography upwind. The coherent structures determined by the upwind topography modulate the variation of power production. The turbulence produced by the

upwind topography promotes the mean energy entrainment into the wake. Furthermore, the local topography downwind of the turbines has a negligible effect on the recovery of the wake. The average power production of the turbine is negatively affected by wavy wall because compared to a flat wall, the shear increases and the available energy at the turbine rotor is less. The turbine located on the flat terrain with inlet velocity taken from the wavy terrain precursor showed to have a similar power production and fluctuations to that located in the cavity of the ridges. The fluctuations in the power production showed to be related mostly to the amplitude of the ridges than to the location of the turbines.

In the final part of this dissertation we extended the work done on high resolution turbine modeling to a more practical case, where we reproduce a real wind farm. One-way nested mesoscale to microscale simulations of a wind farm were performed using the Weather Research and Forecasting model (WRF). Turbines in WRF were modeled as a momentum deficit and a source of turbulent kinetic energy as in Fitch et al. [16, 18]. To incorporate the turbines into very coarse large-eddy simulation, a modification to the implementation of the wind farm parameterization was proposed. The wind speed, direction, boundary layer profile and power production obtained from WRF agreed well with SCADA data and velocity profiles obtained with a scanning LiDAR.

To increase the resolution even further, our in-house LES code with a rotating actuator disk model was nested into the innermost domain of WRF. The wind speed and wind direction of WRF innermost domain were used to provide time and space resolved boundary conditions to our in-house LES code. Simulations performed with our in-house LES code improved slightly the results because of a finer grid and a more detailed turbine model, the RADM, which accounts for the variability of the wind speed in the rotor when the shear is high. However, both numerical codes provide a good approximation of the power production of the turbines.

REFERENCES

- [1] Wind vision: A new era for wind power in the united states. Technical report, United States Department of Energy, 2015.
- [2] 2015 wind technologies market report. Technical report, United States Department of Energy, 2016.
- [3] L A Martínez-Tossas, M J Churchfield, and S Leonardi. Large eddy simulations of the flow past wind turbines: actuator line and disk modeling. *Wind Energy*, 18(6):1047–1060, 2015.
- [4] P A Krogstad and P Eriksen. Blind test calculations of the performance and wake development for a model wind turbine. *Renewable Energy*, 50:325 – 333, 2013.
- [5] J Zalasiewicz, M Williams, W Steffen, and P Crutzen. The new world of the anthropocene. *Environmental science and technology*, 44:2228–2231, 2010.
- [6] S Mathew. *Wind Energy: Fundamentals, resource analysis and economics*. Springer-Verlag Berlin Heidelberg, 1 edition, 2006.
- [7] R Mikkelsen, J N Sørensen, S Øye, and N Troldborg. Analysis of power enhancement for a row of wind turbines using the actuator line technique. *Journal of Physics: Conference Series*, 75(1):012044, 2007.
- [8] J F Ainslie. Calculating the flowfield in the wake of wind turbines. *Journal of Wind Engineering and Industrial Aerodynamics*, 27(1):213 – 224, 1988.
- [9] N O Jensen. *A note on wind generator interaction*. 1983.
- [10] E Machefaux, GC Larsen, and JP Murcia-Leon. Engineering models for merging wakes in wind farm optimization applications. *Journal of Physics: Conference Series*, 625:012037, 2015.
- [11] GV Iungo, C Santoni-Ortiz, M Abkar, F Porté-Agel, MA Rotea, and S Leonardi. Data-driven reduced order model for prediction of wind turbine wakes. *Journal of Physics: Conference Series*, 625:012009, 2015.
- [12] M Debnath, C Santoni, S Leonardi, and GV Iungo. Towards reduced order modelling for predicting the dynamics of coherent vorticity structures within wind turbine wakes. *Philosophical Transactions of the Royal Society A: Mathematical, Physical and Engineering Sciences*, 375(2091):20160108, 2017.
- [13] V Santhanagopalan, MA Rotea, and GV Iungo. Performance optimization of a wind turbine column for different incoming wind turbulence. *Renewable Energy*, 2017.

- [14] J N Sørensen, W Z Shen, and X Munduate. Analysis of wake states by a full-field actuator disc model. *Wind Energy*, 1(2):73–88, 1998.
- [15] J N Sørensen and W Z Shen. Numerical Modeling of Wind Turbine Wakes. *Journal of Fluids Engineering*, 124:393–399, 2002.
- [16] A Fitch, J B Olson, J Lundquist, J Dudhia, A Gupta, J Michalakes, and I Barstad. Local and mesoscale impacts of wind farms as parameterized in a mesoscale NWP model. *Monthly Weather Review*, 140(9):3017–3038, 2012.
- [17] M Abkar and F Porté-Agel. A new wind-farm parameterization for large-scale atmospheric models. *Journal of Renewable and Sustainable Energy*, 7(1):013121, 2015.
- [18] A C Fitch, J K Lundquist, and Olson J B. Mesoscale influences of wind farms throughout a diurnal cycle. *Monthly Weather Review*, 141(7):2173–2198, 2013.
- [19] J C Y Lee and J K Lunquist. Observing and simulating wind-turbine wakes during the evening transition. *Boundary-Layer Meteorology*, 164(3):449–474, 2017.
- [20] C Santoni, U Ciri, M Rotea, and S Leonardi. Development of a high fidelity CFD code for wind farm control. In *2015 American Control Conference (ACC)*. IEEE, 2015.
- [21] A Wray. Minimal storage time-advancement scheme for spectral methods. Technical Report MS 202, NASA Ames Research Center, NASA Ames Research Center, California, 1990.
- [22] H Tennekes and J Lumley. *A first course in turbulence*. MIT Press, 1972.
- [23] P Orlandi and S Leonardi. DNS of turbulent channel flows with two- and three-dimensional roughness. *Journal of Turbulence*, 7:N73, 2006.
- [24] S Leonardi, P Orlandi, R J Smalley, L Djenidi, and R A Antonia. Direct numerical simulations of turbulent channel flow with transverse square bars on one wall. *Journal of Fluid Mechanics*, 491:229238, 2003.
- [25] P Burattini, S Leonardi, P Orlandi, and R A Antonia. Comparison between experiments and direct numerical simulations in a channel flow with roughness on one wall. *Journal of Fluid Mechanics*, 600:403426, 2008.
- [26] E A Fadlun, R Verzicco, P Orlandi, and J Mohd-Yusof. Combined immersed-boundary finite-difference methods for three-dimensional complex flow simulations. *J. Comput. Phys.*, 161(1):35–60, 2000.
- [27] J Sørensen and W Shen. *Computation of Wind Turbine Wakes using Combined Navier-Stokes/Actuator-line Methodology*, pages 156–159. 1999.

- [28] A Betz and L Prandtl. Schraubenpropeller mit geringstem energieverlust. mit einem zusatz von l. prandtl. *Nachrichten von der Gesellschaft der Wissenschaften zu Gttingen, Mathematisch-Physikalische Klasse*, 1919:193–217, 1919.
- [29] Umberto Ciri, Giovandomenico Petrolo, Maria Vittoria Salvetti, and Stefano Leonardi. Large-eddy simulations of two in-line turbines in a wind tunnel with different inflow conditions. *Energies*, 10(6), 2017.
- [30] C Santoni, K Carrasquillo, I Arenas-Navarro, and S Leonardi. Effect of tower and nacelle on the flow past a wind turbine. *Wind Energy*, 20(12):1927–1939, 2017.
- [31] C Santoni, K Carrasquillo, I Arenas-Navarro, and S Leonardi. Cover image. *Wind Energy*, 20(12):i–i, 2017.
- [32] P K Jha, M J Churchfield, P J Moriarty, and S Schmitz. Guidelines for Volume Force Distributions Within Actuator Line Modeling of Wind Turbines on Large-Eddy Simulation-Type Grids. *ASME Journal of Solar Energy Engineering*, 136:031003–031003–11, 2014.
- [33] L A Martínez-Tossas, M J Churchfield, and C Meneveau. Optimal smoothing length scale for actuator line models of wind turbine blades based on gaussian body force distribution. *Wind Energy*, 20(6):1083–1096, 2017.
- [34] Y Wu and F Porté-Agel. Large-eddy simulation of wind-turbine wakes: Evaluation of turbine parametrisations. *Boundary-Layer Meteorology*, 138(3):345–366, 2011.
- [35] H Sarlak, C Meneveau, and J N Sørensen. Role of subgrid-scale modeling in large eddy simulation of wind turbine wake interactions. *Renewable Energy*, 77:386 – 399, 2015.
- [36] F Pierella, P A Krogstad, and L Sætran. Blind test 2 calculations for two in-line model wind turbines where the downstream turbine operates at various rotational speeds. *Renewable Energy*, 70:62 – 77, 2014. Special issue on aerodynamics of offshore wind energy systems and wakes.
- [37] A Mittal, K Sreenivas, Taylor L K, L Hereth, and C B Hilbert. Blade-resolved simulations of a model wind turbine: effect of temporal convergence. *Wind Energy*, 19(10):1761–1783, 2016. WE-14-0228.R2.
- [38] S Kang, X Yang, and F Sotiropoulos. On the onset of wake meandering for an axial flow turbine in a turbulent open channel flow. *Journal of Fluid Mechanics*, 744:376403, 2014.
- [39] L P Chamorro, C Hill, S Morton, C Ellis, R E A Arndt, and F Sotiropoulos. On the interaction between a turbulent open channel flow and an axial-flow turbine. *Journal of Fluid Mechanics*, 716:658670, 2013.

- [40] P A Krogstad and J A Lund. An experimental and numerical study of the performance of a model turbine. *Wind Energy*, 15(3):443–457, 2012.
- [41] P A Krogstad and L Sæ tran. Invitation to the 2013 “blind test 3” workshop: Two in-line wind turbines with spanwise offset. Technical report, Norwegian University of Science and Technology, 2013.
- [42] N Troldborg. *Actuator line modeling of wind turbines wakes*. PhD thesis, Technical University of Denmark, 2008.
- [43] R B Cal, J Lebrón, L Castillo, H S Kang, and C Meneveau. Experimental study of the horizontally averaged flow structure in a model wind-turbine array boundary layer. *Journal of Renewable and Sustainable Energy*, 2(1):013106, 2010.
- [44] C VerHulst and C Meneveau. Large eddy simulation study of the kinetic energy entrainment by energetic turbulent flow structures in large wind farms. *Physics of Fluids*, 26(2):025113, 2014.
- [45] L Lignarolo, D Ragni, C Simão Ferreira, and van Bussel G. Experimental quantification of the entrainment of kinetic energy and production of turbulence in the wake of a wind turbine with particle image velocimetry. In *32nd ASME Wind Energy Symposium*. American Institute of Aeronautics and Astronautics, 2014.
- [46] J Jeong and F Hussain. On the identification of a vortex. *Journal of Fluid Mechanics*, 285:6994, 1995.
- [47] C Williamson. Vortex dynamics in the cylinder wake. *Annual Review of Fluid Mechanics*, 28(1):477–539, 1996.
- [48] J. C. Kaimal and J. J. Finnigan. *Atmospheric boundary layer flows: their structure and measurement*. Oxford University Press, 1994.
- [49] S Frandsen. On the wind speed reduction in the center of large clusters of wind turbines. *Journal of Wind Engineering and Industrial Aerodynamics*, 39(1-3):251–265, 1992.
- [50] M Calaf, C Meneveau, and J Meyers. Large eddy simulation study of fully developed wind-turbine array boundary layers. *Physics of Fluids*, 22(1):015110, 2010.
- [51] C Meneveau. The top-down model of wind farm boundary layers and its applications. *Journal of Turbulence*, 13:N7, 2012.
- [52] K B Howard, Chamorro L P Hu, J S, and M Guala. Characterizing the response of a wind turbine model under complex inflow conditions. *Wind Energy*, 18(4):729–743, 2014.

- [53] K B Howard, L B Chamorro, and M Guala. A comparative analysis on the response of a wind-turbine model to atmospheric and terrain effects. *Boundary-Layer Meteorology*, 158(2):229–255, 2015.
- [54] X Yang, K B Howard, M Guala, and F Sotiropoulos. Effects of a three-dimensional hill on the wake characteristics of a model wind turbine. *Physics of Fluids*, 27(2):025103, 2015.
- [55] E Politis, J Prospathopoulos, D Cabezón, K S Hansen, P K Chaviaropoulos, and R Barthelmie. Modeling wake effects in large wind farms in complex terrain: the problem, the methods and the issues. *Wind Energy*, 15(1):161–182, 2011.
- [56] W Tian, A Ozbay, W Yuan, P Sarkar, and H Hu. An experimental investigation on the performances of wind turbines sited over a hilly terrain. In *31st AIAA Applied Aerodynamics Conference*. American Institute of Aeronautics and Astronautics, 2013.
- [57] J Jonkman, S Butterfield, W Musia, and G Scott. Definition of a 5-MW reference wind turbine for offshore system development. Technical report, National Renewable Energy Laboratory, 2009.
- [58] J Meyers and C Meneveau. Flow visualization using momentum and energy transport tubes and applications to turbulent flow in wind farms. *Journal of Fluid Mechanics*, 715:335–358, 2013.
- [59] C Santoni, EJ García-Cartagena, U Ciri, GV Iungo, and S Leonardi. Coupling of mesoscale weather research and forecasting model to a high fidelity large eddy simulation. *Journal of Physics: Conference Series*, 1037(6):062010, 2018.
- [60] A Fitch. Notes on using the mesoscale wind farm parameterization of fitch et al.(2012) in WRF. *Wind Energy*, 19(9):1757–1758, 2015.
- [61] Giacomo Valerio Iungo and Fernando Port-Agel. Volumetric lidar scanning of wind turbine wakes under convective and neutral atmospheric stability regimes. *Journal of Atmospheric and Oceanic Technology*, 31(10):2035–2048, 2014.
- [62] S El-Asha, L Zhan, and G V Iungo. Quantification of power losses due to wind turbine wake interactions through SCADA, meteorological and wind LiDAR data. *Wind Energy*, 2017.
- [63] U Ciri, M Rotea, C Santoni, and S Leonardi. Large eddy simulation for an array of turbines with extremum seeking control. In *2016 American Control Conference (ACC)*. IEEE, 2016.
- [64] M Abkar, A Sharifi, and F Porté-Agel. Wake flow in a wind farm during a diurnal cycle. *Journal of Turbulence*, 17(4):420–441, 2016.

- [65] J D Mirocha, B Kosovic, M L Aitken, and J K Lundquist. Implementation of a generalized actuator disk wind turbine model into the weather research and forecasting model for large-eddy simulation applications. *Journal of Renewable and Sustainable Energy*, 6(1):013104, 2014.
- [66] J D Mirocha, D A Rajewski, N Marjanovic, J K Lundquist, B Kosović, C Draxl, and M J Churchfield. Investigating wind turbine impacts on near-wake flow using profiling lidar data and large-eddy simulations with an actuator disk model. *Journal of Renewable and Sustainable Energy*, 7(4):043143, 2015.
- [67] L Vollmer, J C-Y Lee, G Steinfeld, and J K Lundquist. A wind turbine wake in changing atmospheric conditions: Les and lidar measurements. *Journal of Physics: Conference Series*, 854(1):012050, 2017.
- [68] J. C. Y. Lee and J. K. Lundquist. Evaluation of the wind farm parameterization in the weather research and forecasting model (version 3.8.1) with meteorological and turbine power data. *Geoscientific Model Development*, 10(11):4229–4244, 2017.
- [69] M Nakanishi and H Niino. An improved mellor–yamada level-3 model: Its numerical stability and application to a regional prediction of advection fog. *Boundary-Layer Meteorology*, 119(2):397–407, 2006.
- [70] M Nakanishi and H Niino. Development of an improved turbulence closure model for the atmospheric boundary layer. *Journal of the Meteorological Society of Japan*, 87(5):895–912, 2009.
- [71] Jason H. Laks, Lucy Y. Pao, and Alan D. Wright. Control of Wind Turbines : Past , Present , and Future. *Proceedings of the American Control Conference*, pages 2096–2103, 2009.
- [72] W C Skamarock, J B Klemp, J Dudhia, D O Gill, D M Barker, M G Duda, X Y Huang, W Wang, and J G Powers. A description of the advance research wrf version 3. Technical report, National Center for Atmospheric Research, 2008.
- [73] Sonia Wharton and Julie K. Lundquist. Assessing atmospheric stability and its impacts on rotor-disk wind characteristics at an onshore windfarm. *Wind Energy*, 15(4):525–546, 2012.
- [74] A. E. Perry, K. L. Lim, and S. M. Henbest. An experimental study of the turbulence structure in smooth- and rough-wall boundary layers. *Journal of Fluid Mechanics*, 177:437466, 1987.
- [75] G. G. Katul, C. R. Chu, M. B. Parlange, J. D. Albertson, and T. A. Ortenburger. Lowwavenumber spectral characteristics of velocity and temperature in the atmospheric surface layer. *Journal of Geophysical Research: Atmospheres*, 100(D7):14243–14255, 1995.

- [76] A. N. Kolmogorov. The local structure of turbulence in incompressible viscous fluid for very large reynolds numbers. *Proceedings: Mathematical and Physical Sciences*, 434(1890):9–13, 1991.
- [77] C J Willmott. On the validation of models. *Physical Geography*, 2(2):184–194, 1981.

BIOGRAPHICAL SKETCH

Christian Santoni was born in Carolina, Puerto Rico. He completed his schoolwork in 2005 where he then attended the University of Puerto Rico at Mayagüez. There he obtained his Bachelor degree in Mechanical Engineering in 2010. Interested in science, he pursued graduate studies in numerical rheology and thermodynamics where he obtained a Master of Science in 2010 from that same university. Inspired by his coursework, professors and the challenge, he makes a minor detour in interest into fluid mechanics and turbulence.

In 2013, he started his PhD at the University of Texas at Dallas under the supervision of Dr. Stefano Leonardi. He performed research on turbine modeling, effect of surface roughness on the performance of turbines and the use of numerical weather prediction models to study the performance of turbines and wind farms under real conditions.

CURRICULUM VITAE

Christian SANTONI

Graduate Student HPCFD Research Group

Education

- 2013-Present Ph.D. in MECHANICAL ENGINEERING, **The University of Texas**, Dallas
Major: Mechanical Engineering
Dissertation: “Wind farm modeling: From the Meso-scale to the Micro-scale”
Advisor: Prof. Stefano LEONARDI
GPA: 3.6/4
- 2010-2013 M.Sc. in MECHANICAL ENGINEERING, **University of Puerto Rico**, Mayagüez
Thesis: “Brownian Dynamics Simulation of Colloidal Particles in a Gay-Berne Suspension”
Advisor: Gustavo GUTIERREZ
GPA: 3.90/4
- 2005-2010 B.S. in MECHANICAL ENGINEERING, **University of Puerto Rico**, Mayagüez
GPA: 3.88/4 *magna cum laude*

Research Experience

- 2013-Present* | HPCFD Research Group - The University of Texas at Dallas
Direct Numerical Simulation and Large Eddy simulation of bluff and streamlined bodies. Wind turbine modeling. Large Eddy simulations of wind turbines. Numerical weather prediction models for wind farm modeling.
- 2011-2013* | UCF Research Group - University of Puerto Rico at Mayagüez
Brownian and Stokesian dynamics simulation of spherical and non-spherical colloidal particles and rheology.
- 2010-2011* | Prof. Gustavo Gutierrez - University of Puerto Rico at Mayagüez
Modeling and Design of Inductance Accelerators. Finite volume simulation Maxwell’s Equation weakly coupled to Newton’s Law equations.
- 2009* | Prof. Silvina Cancelos - University of Puerto Rico at Mayagüez
Finite Difference simulation of pressure wave propagation along a cylindrical pipe for the detection of obstructions.

Teaching Experience

- 2010 | Thermodynamics II Application to the study of power and refrigeration cycles and combustion processes. Recitation and office hours; grading.
- 2010 | Momentum Transfer Introduction to mass, momentum and energy transport. Recitation and office hours; grading.

Computer Skills

Programming Skills: FORTRAN, C++, PYTHON, Matlab/Octave
Visualization Software: Paraview, Gnuplot, QMGA, POV-Ray
Parallel Computing: OpenMP, MPI and CUDA
Commercial Software: Comsol Multiphysics, FLUENT, StarCCM, SolidWorks
Word processors: MS Word, Open/Libre Office and L^AT_EX

Languages

SPANISH: Mothertongue
ENGLISH: Fluent

Refereed Journal Publications

Google Scholar Profile

- U Ciri, MV Salvetti, K Carrasquillo, C Santoni, GV Iungo, S Leonardi, “*Effects of the subgrid-scale modeling in the Large-Eddy simulations of wind turbines*”, Direct and Large-Eddy Simulation X. ERCOFTAC Series, 2018, vol 24.
- M Debnath, C Santoni, S Leonardi and GV Iungo, “*Development of a reduced order model for prediction of flow dynamics within wind turbine wakes*”, Phil. Trans. R. Soc. A, 2017, 375 20160108; DOI: 10.1098/rsta.2016.0108.
- U Ciri, M Rotea, C Santoni and S Leonardi, “*Large-Eddy simulations with extremum-seeking control for wind turbines array power optimization*”, Wind Energy, 2017, 20: 16171634. doi: 10.1002/we.2112
- C Santoni, K Carrasquillo, I Arenas-Navarro and S Leonardi, “*Effect of tower and nacelle over the flow past a wind turbine*”, Wind Energy, 2017, 20, 19271939. doi: 10.1002/we.2130
- U Ciri, M Rotea, C Santoni and S Leonardi, “*Large Eddy Simulation for an array of turbines with Extremum Seeking Control*”, 2016 American Control Conference (ACC), Boston, MA, 2016, pp. 531-536. doi: 10.1109/ACC.2016.7524968
- C Santoni, U Ciri, M Rotea and S Leonardi, “*Development of a high fidelity CFD code for wind farm control*”, American Control Conference (ACC), 2015, 1715-1720.

- GV Iungo, C Santoni-Ortiz, M Abkar, F Port-Agel, MA Rotea, S Leonardi, “*Data-driven Reduced Order Model for prediction of wind turbine wakes*”, Journal of Physics: Conference Series 625 (1), 2015, 012009
- C Santoni, EJ Garcia-Cartagena, U Ciri, GV Iungo and S Leonardi, “*Coupling of mesoscale Weather Research and Forecasting model to a high fidelity Large Eddy Simulation*”, Journal of Physics: Conference Series, (Submitted)

Conference Presentations

- C Santoni, EJ Garcia-Cartagena, L Zhan, GV Iungo and S Leonardi, “*Weather Research and Forecasting model simulation of an onshore wind farm: assessment against LiDAR and SCADA data*”, 70th Annual Meeting of the American Physics Society Division of Fluid Dynamics, Nov 19-21 (2017).
- C Santoni, U Ciri and S Leonardi, “*Performance of a wind turbine over a ridged terrain*”, 69th Annual Meeting of the American Physics Society Division of Fluid Dynamics, Nov 20-22 (2016).
- C Santoni, U Ciri and S Leonardi, “*Flow past a wind turbine over a wavy terrain*”, European Mechanics Society Colloquium 576 Wind Farms in Complex Terrains, 8-10 June (2016).
- U. Ciri, M.A. Rotea, C. Santoni, and S. Leonardi, “*Extremum-Seeking Control for Power Production Optimization*”, Windfarms 2016: International Colloquium on wind-power plants, May 23rd-25th. Dallas, TX, USA, (2016).
- C Santoni, U Ciri, A William and S Leonardi, “*Performance of a Wind Turbine on a Wavy Terrain*”, Windfarms 2016: International Colloquium on wind-power plants, May 23rd-25th. Dallas, TX, USA, (2016).
- C Santoni, U Ciri and S Leonardi, “*Effect of topography on wind turbine power and load fluctuations*”, 68th Annual Meeting of the American Physics Society Division of Fluid Dynamics, Nov 22-24 (2015).
- C Santoni, U Ciri and S Leonardi, “*Effect of topography on wind turbine power fluctuations and blade loads*”, WindFarms 2015: International colloquium on Large Wind-Power Plants: Interaction, Control and Integration, 8-10 July 2015, Leuven, Belgium.
- C Santoni and S Leonardi, “*Large Eddy Simulation of wind turbines using the actuator line model and immersed boundary method*”, 59th Annual Meeting of the American Physics Society Division of Fluid Dynamics, Nov 23-25 (2014).
- C Santoni, K Carrasquillo, M Rotea, Y Li and S Leonardi, “*Effect of the tip speed ratio in the power production of aligned wind turbines*”, 59th Annual Meeting of the American Physics Society Division of Fluid Dynamics, Nov 23-25 (2014).